Electroweak Interactions on the Deuteron

A Dissertation Presented for the

Doctor of Philosophy

Degree

The University of Tennessee, Knoxville

Jose Luis Bonilla

August 2024

To my beloved parents Norha Panesso and Jose Bonilla whose love, hard work, and perseverance will never be forgotten and to my wife Diana and my beautiful children Mira, Joshua, and Ariel whose love illuminated my life.

Acknowledgements

First, I want to thank my advisor, Dr. Lucas Platter, for the wonderful guidance and assistance he provided throughout my PhD journey. He was always available for any questions and concerns I had regarding research, and I would also like to immensely thank him for the opportunity he gave me to work with him since I was an undergraduate student.

I am grateful to Dr. Daniel Odell for the assistance and help he provided while I was trying to learn the world of quantum mechanics and its computational aspects. Additionally, I want to express my gratitude to Dr. Thomas Papenbrock for the wonderful lectures on Nuclear Physics and for being part of my committee.

I would like to thank Dr. Nadia Fomin, who was my undergraduate professor for the Modern Physics class, for serving as my committee member together with Dr. Lawrence Heilbronn. I want to express my appreciation to Dr. Bijaya Acharya, with whom I was fortunate to collaborate, for the help and guidance provided on computations done in my research.

I am truly grateful for the friendship, conversations, and time spent during my graduate studies with Dr. Samuel Emmons, Dr. Zichao Yang, Dr. Chinmay Mishra, Dr. Chenyi Gu, Dr. Evan Combes, Dr. Rudra Bista, and Shaun Vavra.

Finally, I would like to deeply thank my wife, Diana Aristizabal, for her love and endless support throughout all these years.

"Thou must be emptied of that wherewith thou art full, that thou mayest be filled with that whereof thou art empty."

— Saint Augustine

Abstract

This research explores the intricacies of Electroweak Interactions on the Deuteron, with a particular focus on muon capture and the hyperfine shift in atomic and muonic deuterium. These processes are phenomena of significant importance in nuclear physics. Understanding these interactions is crucial for illuminating fundamental aspects of nuclear structure and providing insight into the fundamental forces and interactions governing atomic and nuclear systems, as well as related processes such as proton-proton fusion or other astrophysical reactions, which are phenomena that cannot be easily reproduced in a laboratory and require a theoretical treatment to predict observables. Through this research, we systematically quantify the theoretical uncertainties associated with chiral effective field theory predictions of the muon-deuteron capture rate and the hyperfine energy shifts in atomic and muonic deuterium focusing on the relevant neutron-neutron (proton-neutron) partial wave channels in the final state, respectively. Our investigation encompasses the examination of several key factors, including the dependence on the cutoff employed to regularize the interactions, and the truncation of the chiral effective field theory expansion of the current operators employed in this research. By integrating these approaches, we present estimates that are comparable to existing data and previous theoretical predictions.

Table of Contents

Chapter 1

Introduction

In the realm of nuclear physics, the deuteron, an atomic nucleus composed of one proton and one neutron, stands as a fundamental laboratory for probing the intricate dynamics of strong and electroweak interactions. The study of electroweak processes on the deuteron provides a unique window into the underlying symmetries and forces governing the behavior of nucleons. This research allows us to understand the characteristics of electroweak interactions on the deuteron, employing theoretical frameworks rooted in Effective Field Theory (EFT) to explore the fundamental properties of nuclear processes.

The deuteron serves as an ideal system for investigating electroweak interactions due to its simple structure and well-defined properties. By subjecting the deuteron to probes, such as photons, neutrinos, electrons, and others, we gain valuable insights into the mechanisms underlying weak interactions and the structure of the nucleon-nucleon potential. Furthermore, the deuteron's role as a benchmark system allows for precise tests of theoretical models and predictions, offering a fertile ground for advancing our understanding of nuclear physics.

In our study, we first investigate the process of muon capture on a deuteron within the framework of chiral effective field theory. The study focuses on quantifying the theoretical uncertainties in the predicted muon-deuteron capture rates, emphasizing the contributions from neutron-neutron partial wave channels in the final state. By performing a detailed uncertainty analysis, this work aims to provide a robust theoretical foundation for the interpretation of forthcoming experimental data by the MuSun collaboration, thereby enhancing our understanding of fundamental nuclear interactions and the dynamics of muon capture processes.

Our second investigation focuses on the hyperfine shift in atomic and muonic deuterium. This study aims to provide a detailed analysis of the hyperfine splitting phenomena, which arises from the interaction between the magnetic moments of the deuteron and the electron or muon. By employing chiral effective field theory and utilizing chiral interactions, we seek to obtain accurate nuclear matrix elements that determine corresponding hyperfine energy shifts. This approach not only enhances our understanding of nucleon-nucleon interactions but also allows us to test and validate the theoretical predictions of chiral EFT in both atomic and muonic systems. Through this investigation, we aim to offer new insights into the fundamental forces shaping the behavior of these nuclear systems.

This document is organized as follows: In Chapter 2, we provide a comprehensive introduction to Effective Field Theory, emphasizing its importance in simplifying and systematically improving the description of physical systems across different scales. In this chapter, we outline key concepts, such as systematic expansion and power counting, and explain the process of constructing an EFT by focusing on the relevant degrees of freedom and symmetries within a specified energy range. Additionally to this, we talk about the foundations of chiral effective field theory, emphasizing its role in low-energy nuclear physics calculations. Moreover, we mention how chiral EFT allows for the construction of current operators by exploiting the symmetries and the spontaneous breaking of chiral symmetry in quantum chromodynamics. Within this framework, we explain how electroweak currents provide a systematic way to describe interactions between nucleons and leptons and how we use them to analyze electroweak processes studied in this project.

In Chapter 3, we focus on the muon capture process on the deuteron, highlighting the use of chiral effective field theory to derive and calculate the capture rate. we detail the reaction mechanism, kinematics, and theoretical calculations involved in estimating the rate. We emphasize on quantifying the uncertainties associated with theoretical predictions, ensuring the reliability and accuracy of the results.

In Chapter 4, we study the hyperfine shift in both atomic and muonic deuterium, emphasizing the use of chiral interactions and electroweak current operators. We provide details on the dynamics of these processes, the kinematics, and the theoretical prescriptions involved in predicting the hyperfine energy shifts.

Finally, in the Appendices, we provide detailed derivations for the intermediate steps in the calculation of the muon capture rate on the deuteron and the hyperfine shift in atomic and muonic deuterium. These derivations involve the calculation of the deuteron wave functions, the solution of the Lippmann-Schwinger equation (t-matrix), the inclusion of final state interactions in nuclear matrix elements, and other calculations involved throughout this research.

Chapter 2

Effective Field Theory

2.1 Introduction

In the realm of theoretical physics, the pursuit of understanding the fundamental building blocks of the universe and its deep complexity has led to the developing of powerful frameworks that allow the description of physical phenomena across a wide range of scales. These scales may be quantified in units such as time, distance, or energy. To illustrate this, we can imagine a piece of cord hanging from a tree branch. From a distance, this cord may be seen as a massless line with length L and maybe positioned in an angle θ relative to the tree branch. Now if we were from the size of an ant and be standing on the cord, then our perspective of reality would be totally different. We could think of the cord as a cylindrical massive object with a volume V described by its radius R and length L. As we go further in smaller scales, we can notice that the cord is made of fibers and if we go further down then we would be able to notice that this fibers are actually made of atoms connected by electromagnetic forces. At each of these different scales, there is a different set of physics that would allows to understand and describe the very same object.

At this point, one can argue that to do physics on a specific system comprehensively, it is advantageous to isolate a subset of phenomena from the rest. This enables us to describe the system without the need for a complete understanding of every aspect. Typically, this can be achieved by partitioning the parameter space of the system into various regions, each of which requires a distinct description of the relevant physics. This framework is known as Effective Theory. The main concept is that certain parameters are either significantly smaller or larger in magnitude compared to the physical quantities of interest. By setting the small parameters to zero and the large parameters to infinity, we can obtain a considerably simplified approximation of the physics. The finite effects of parameter sizes are then considered as minor perturbations around this initial approximation. If the separation of scales fall within the hierarchy of energy scales, then we think of Effective Field Theory or EFT. This is the cornerstone in the fields of nuclear, particle, and atomic physics which is a conceptual and mathematical framework that has proven to be invaluable in unraveling the complexities of diverse physical systems in the realm of quantum mechanics.

An Effective Field Theory is regarded as the low-energy limit of a specific fundamental theory, allowing for the calculation of low-energy characteristics of physical systems with a finite margin of error. This is achieved by incorporating the relevant degrees of freedom and taking advantage of a separation of scales within the system [14]. As a consequence, any EFT requires a renormalization and regularization scheme which ensures that a set of physical observables remain finite and well-defined. Formally speaking, an EFT has a small expansion parameter $\beta = q_{low}/q_{high}$ known as the power-counting parameter, where $q_{low} \ll q_{high}$. Calculations describing a particular system can be expanded to some order n in β, from which we can obtain an error of order $\epsilon = \beta^{n+1}$. This systematic expansion has a well defined procedure to calculate higher order corrections in β, allowing us to make our theoretical error as small as we need by choosing a sufficient large n.

An excellent illustration that highlights the separation of scales and power counting is the widely recognized Fermi theory of beta decay. Take, for instance, neutron beta decay, depicted by the process $n \to p + e^- + \bar{\nu}_e$ and mediated by the W boson. At energy transfers much lower than the W boson mass of 80 GeV, the W boson propagator is defined by

$$\frac{1}{q^2 - M_W^2} \ , \tag{2.1}$$

where q represents a low-energy transfer and M_W stands for the mass of the W boson. By selecting $q_{low} = q$ and $q_{high} = M_W$, we can formulate a small expansion parameter, $\beta = q/M_W$, and subsequently expand the propagator in terms of β. This leads to the propagator taking the form:

$$-\frac{1}{M_W^2}\left[\frac{1}{1-\beta^2}\right] \longrightarrow -\frac{1}{M_W^2}\left[1+\beta^2+\beta^4+\mathcal{O}\big(\beta^6\big)\right] \tag{2.2}$$

From this resulting expansion, the leading-order (LO) term is $-1/M_W^2$, which corresponds to a contact interaction explained in Fermi's beta decay theory. The large mass of the W boson contained in the propagator makes the interaction short-ranged. With this simple example, our objective is to understand the construction and simplification of an Effective Field Theory by choosing appropriate degrees of freedom within a specified energy range and identifying potential symmetries within the system under study. This allows us to construct a general Lagrangian that can be expressed in terms of an expansion parameter, facilitating the development of a power-counting scheme. This approach helps us identify the essential leading-order contributions in the expansion in terms of the expansion parameter, such as β, thereby minimizing errors in our calculations. Subsequently, we will provide a brief discussion on the fundamentals of χEFT. We will explore how incorporating the pion mass as a fundamental parameter of the theory enables the establishment of a power counting system. This counting system is crucial in the development of current operators utilized in the calculation of electroweak processes outlined in this document. At this point, we can provide a general procedure for constructing an effective field theory.

EFT General Formulation Steps:

1. *Identify relevant degrees of freedom and energy scales:*

   Begin by identifying the key components and degrees of freedom in a system. These could be particles, fields, or other objects that play a crucial role in the dynamics of the system. Then, understand the energy scale of interest in the system. Effective Field Theories are designed to be effective at certain energy scales, and choosing the appropriate scale is crucial for the accuracy and efficiency of the theory. For this, identify q_{low} and q_{high} scales; these q-scales can be either momenta or energies associated to the limits in which the system is contained.

2. *Identify and Incorporate Symmetries:*

   Identify global and local symmetries of underlying theory and how they are broken. Utilize symmetries inherent in the system to simplify the EFT. Symmetry considerations can lead to powerful constraints on the form of the Lagrangian and guide the choice of terms.

3. *Construct the Lagrangian:*

   Formulate the Lagrangian that describes the system. This involves writing down the kinetic and potential terms that govern the dynamics of the identified degrees of freedom. Include interaction terms that capture the relevant physics at the specified energy scale.

4. *Power counting:*

   Employ power counting to organize terms in the Lagrangian based on their relevance at different energy scales. This helps prioritize terms and determine which ones are more important for a given level of precision. For this, we identify a power counting scheme which is related to a small expansion parameter such as β.

5. *Regularization and renormalization:*

   Address issues related to divergences and renormalization. Renormalize the theory to absorb infinities into redefined parameters, ensuring that physical observables remain finite and well-defined. Declaration of a regularization and renormalization scheme. We must introduce a regulator to ensure the theory behaves appropriately at high energies or momenta in our loop integrals, which involve summations over intermediate states.

6. *Match to Full Theory:*

   Ensure that the EFT reproduces the relevant physics of the full theory at the chosen energy scale. This involves matching observables and coefficients to those derived from the complete, more fundamental description or experimental data.

7. *Validation and Predictions:*

   Validate the EFT by comparing its predictions to experimental or observational data. Refine the theory as needed based on the level of agreement and use it to make predictions for new phenomena or unexplored regimes within the chosen energy scale.

In the next section, we will discuss χEFT and its foundations, and how the exploitation of symmetries in a nuclear system is used to derive nuclear forces and current operators from chiral Lagrangians.

2.2 χEFT Foundations

In the pursuit of understanding the strong force that binds quarks and gluons within atomic nuclei, Chiral Effective Field Theory (χEFT) emerges as a powerful and elegant framework. Rooted in the principles of chiral symmetry, a fundamental symmetry of the strong force governing the behavior of massless quarks, χEFT provides a systematic and model-independent approach to describe the interactions of nucleons and pions, the building blocks of atomic nuclei.

χEFT represents a bridge between the fundamental principles of Quantum Chromodynamics (QCD), the theory of the strong force, and the effective descriptions necessary for practical calculations in low-energy nuclear physics. By acknowledging the spontaneous breaking of chiral symmetry in QCD, χEFT introduces an organized expansion in terms of small parameters, allowing us to navigate the complexities of nuclear interactions with precision and predictive power.

The development of χEFT was motivated by the necessity to understand nuclear interactions without looking into the complexity of QCD. The challenge with the QCD approach is that it cannot be used directly in deriving nuclear forces. QCD itself is a relativistic, non-perturbative quantum field theory. This complexity arises from the behavior of quarks and gluons, the colored particles in QCD, whose interactions are weak at short distances (high energies), behaving almost like free particles when they are close together. This phenomenon is known as asymptotic freedom. Conversely, at long distances (low energies), the interactions of colored objects are strong, leading to the confinement of quarks into colorless objects known as hadrons. However, there are other approches such as Lattice Quantum Chromodynamics (LQCD) that attempts to describe the theory of the strong force by discretizing space-time into a finite lattice. This enables the numerical study of QCD in the non-perturbative regime. This approach allows for the calculation of hadronic properties and interactions. Unfortunately, LQCD calculations are computationally intensive, requiring significant resources and sophisticated algorithms often relying on Monte Carlo methods.

To overcome the difficulties associated with the non-perturbative nature of QCD at low energies, χEFT provides a systematic framework that leverages the symmetries of QCD, particularly chiral symmetry, to describe nuclear forces using only nucleonic and pionic degrees of freedom. Chiral symmetry is an approximate symmetry of QCD that becomes exact in the limit of massless up and down quarks. By treating pions (the lightest mesons) as the Goldstone bosons associated with the spontaneous breaking of chiral symmetry, χEFT allows for the construction of an effective theory that captures the essential physics of low-energy nuclear interactions.

In χEFT, the interactions are organized in a systematic expansion in terms of a small parameter, typically the ratio of the pion mass to the chiral symmetry breaking scale. This expansion, known as the chiral expansion, provides a hierarchy of terms that can be calculated to a desired level of accuracy. The leading-order terms capture the most significant contributions, while higher-order terms provide corrections that can be systematically included to improve precision.

One of the key advantages of χEFT is that it provides a clear and systematic way to quantify theoretical uncertainties. By truncating the chiral expansion at a certain order, one can estimate the uncertainty associated with the neglected higher-order terms. This feature is particularly important for making reliable predictions and for comparing theoretical results with experimental data.

χEFT has been successfully applied to a wide range of nuclear phenomena, from the properties of individual nucleons to the interactions between multiple nucleons and the structure of light nuclei. It has also been extended to include electroweak interactions, enabling the study of processes such as those examined in this document: muon capture and the hyperfine shift in atomic and muonic deuterium. Overall, χEFT provides a powerful and versatile tool for exploring the rich and complex world of nuclear physics while remaining grounded in the fundamental principles of QCD.

2.2.1 Nuclear Forces in χEFT

By following the general formulation steps of EFT from the previous section, one can provide a simplified overview of the development of nuclear forces in χEFT.

First, it is necessary to identify a separation of energy scales. This is done by identifying the relevant degrees of freedom in our framework, which are pions and nucleons. Therefore, our low-energy scale is the pion mass, $q_{\text{low}} = m_\pi$, and our high-energy scale, q_{high}, is set to the chiral symmetry breaking scale $\Lambda_\chi \approx 700$ GeV, which is of the order of the ρ meson mass.

The next step is to construct the relevant Lagrangian that describes our system. In χEFT, interactions between Goldstone bosons must vanish in the chiral limit, meaning that $m_\pi \to 0$ and at zero momentum transfer. Therefore, the low-energy expansion of the effective Lagrangian is expressed in powers of pion masses and derivatives, and in powers of the small expansion parameter $\beta = \{m_\pi, q\}/\Lambda_\chi$. The effective Lagrangian can formally be written and expressed as a perturbation series in symbolic and general form as follows:

$$\mathcal{L}_{eff} = \mathcal{L}_\pi^2 + \mathcal{L}_\pi^4 + \mathcal{L}_{\pi N}^1 + \mathcal{L}_{\pi N}^2 + \mathcal{L}_{\pi N}^3 + \mathcal{L}_{NN}^0 + \mathcal{L}_{\pi NN}^1 + \dots \, . \tag{2.3}$$

The superscripts refer to the number of derivatives and/or insertions of the pion mass. The effective Lagrangian $\mathcal{L}_{\text{eff}}$ is described by the pionic $\mathcal{L}_\pi$ and pion-nucleon Lagrangians $\mathcal{L}_{\pi N}$, which contain information about the low-energy constants. The relevant terms are shown in [4]. Terms for $\mathcal{L}^0_{NN}$ and $\mathcal{L}^1_{\pi NN}$ are listed in [14]. By employing the canonical formalism, the corresponding pion-nucleon Hamiltonian is derived from Eq.(2.3), which governs the pion-nucleon dynamics in the presence of external fields. In general, this Hamiltonian depends on external axial-vector, vector, scalar, and pseudoscalar sources, which are space- and time-dependent. The flavor structure and transformation properties with respect to chiral rotations are beyond the scope of this research.

In the modern framework of χEFT, the frequently used methods to derive nuclear forces are based on unitary transformation and the S-matrix. In the former scheme, the potential is derived by applying an appropriately chosen unitary transformation to the pion-nucleon Hamiltonian that describes the system, which allows the elimination of the coupling between the nucleonic Fock space states and those containing pions. In the second approach, the nuclear potential is defined by matching the amplitude to the iterated Lippmann-Schwinger equation. Both methods lead to energy-independent interactions, which is a feature that enables applications to systems with three or more nucleons [14]. In this work, the electroweak currents used were derived in [25] using the method of unitary transformations (MUT). This choice provides the freedom to alter and define current operators and nuclear forces through the selected MUT, essentially by adjusting the basis in the Fock space. This is because, unlike the S-matrix, current operators and nuclear forces are not direct observables.

Moreover, the ambiguity in the unitary transformation, which is related to the freedom in choosing the basis in Fock space, can be simplified by requiring renormalizability within the framework of the nuclear Hamiltonian and current operators. Specifically, systematically applying this freedom is essential to guarantee the cancellation of ultraviolet divergences in the corresponding counterterms in the effective Lagrangian and the loop contributions to the one-pion exchange electromagnetic current operator, leading to finite matrix element contributions of the currents.

As explained in [25], the nuclear potential and the currents are obtained from the effective Lagrangian describing the interactions between pions and nucleons in the presence of external sources.

In the following subsection, there will be a brief explanation of how the electroweak currents are classified and used as building blocks to study the muon capture and the hyperfine shift in atomic and muonic deuterium processes.

2.2.2 Electroweak currents

Interactions of nuclear systems with external probes such as photons, electrons, neutrinos, and others, are characterized by current operators. In the presence of these sources, these operators enables the transition from one state to another within a system of particles in χEFT. These current operators are consistently derived order by order in a power counting or Q-counting scheme with the effective Hamiltonian of the system.

These current operators contain 1-body, 2-body, and N-body contributions, which are categorized based on the number of nucleons participating directly in the interaction with a particular external probe. They can be ordered by using the number of nucleons they couple to ,

$$J^\mu = \sum_{i=1}^{N} j^\mu_{(i)} + \sum_{i<j}^{N} j^\mu_{(i,j)} + \ldots \, . \tag{2.4}$$

Here $j^\mu_{(i)}$ and $j^\mu_{(i,j)}$ describe the 1-body and 2-body current operators respectively. This current operator is expressed as the sum of vector V^μ and axial A^μ currents and they serve as the foundational components of the nuclear electroweak current. Now the operator J^μ is defined as

$$J^\mu = A^\mu_{1B} + V^\mu_{1B} + A^\mu_{2B} + V^\mu_{2B} \ , \tag{2.5}$$

where the subscripts in the axial and vector currents refer to 1-body ($1B$) and 2-body ($2B$) contributions, respectively. It is worth noting that from the conserved vector current hypothesis, the vector component is linked to the electromagnetic currents through isospin rotations. Relations for these current operators have been previously derived in Refs. [33, 32, 31, 42]. In this study, we employ operators obtained through the method of unitary transformations as derived by Krebs *et al.* [25] and Kölling *et al.* [24].

In EFT, we assign orders in Q-counting to describe the order of the axial and vector current operators contributions. In our framework, the expansion parameter Q is given by $\max(m_\pi; q)/\Lambda_b$, where m_π and q are the mass of the pion and a particular low momentum scale, and Λ_b is related to the breakdown scale of the theory. The Q-counting that describes the ordering of the chiral electroweak currents used in our study is displayed in Tbl. 2.1. These current operators contain a range of non-zero contributions at leading order (LO), next-to-leading order (NLO), and next-to-next-to-leading order (NNLO). Additionally, the Q-counting incorporates terms labeled with $1/m$ which are relevant relativistic corrections.

In this section, we provide the precise form of the current operators used in this work. Many of this terms have unitary-phase dependence which are given by the standard choice in [25].

To have a better insight, We can split the total electroweak contribution into axial A^μ and vector V^μ currents. The first contribution to electroweak current arises at order Q^{-3}. This comprises a static time-like 1-body vector operator Eq.(2.6) and a space-like 1-body axial operator Eq.(2.7). The latter includes the sum of the conventional Gamow-Teller operator along with a pion-pole contribution incorporated within the pseudoscalar form factor of this term. This is effectively illustrated by the diagram depicted in Fig. 2.1(a). The time-like component of the 1-body vector current follows the conventional expression

$$V^0_{1B} = G_E(t)\ \tau_{-,1}\ +\ (1 \to 2)\ , \tag{2.6}$$

where $(1 \to 2)$ refers to the exchange of index value of the ith nucleon on which we are operating on. The vector components of the 1-body axial current are

$$\mathbf{A}_{1B} = \left[-G_A(-\mathbf{q}^2)\boldsymbol{\sigma}_1 + \frac{G_P(-\mathbf{q}^2)}{4m^2}\boldsymbol{q}(\boldsymbol{q}\cdot\boldsymbol{\sigma}_1)\right]\tau_{-,1}\ +\ (1 \to 2)\ , \tag{2.7}$$

where $m = 938.9$ MeV, $\boldsymbol{q} = \boldsymbol{p}'_i - \boldsymbol{p}_i$.

At the Q^{-1} order, we encounter the leading-order time-like 1-body relativistic correction $(1/m)$ and a time-like 1-body axial operator Eq. (2.8), which arises from the time evolution of unitary transformations. The time-like component of the 1-body axial current operator includes contributions from both the axial form factor G_A and the pseudoscalar form factor G_P,

$$A^0_{1B} = \left[-\frac{G_A(-\mathbf{q}^2)}{m} \boldsymbol{q}_1 \cdot \boldsymbol{\sigma}_1 + \frac{G_P(-\mathbf{q}^2)}{4m^2} q_0 \boldsymbol{q} \cdot \boldsymbol{\sigma}_1 \right] \tau_{-,1} \; + \; (1 \to 2) \; , \tag{2.8}$$

where $q_0 = (\boldsymbol{p}_i'^2 - \boldsymbol{p}_i^2)/2m$, and $\boldsymbol{q}_i = (\boldsymbol{p}_i' + \boldsymbol{p}_i)/2$. These operators are described by the diagrams from Fig.(2.1b) and Fig.(2.1c) respectively. Additionally, there is a space-like vector operator contribution, as described in Eq. (2.9), incorporating the spin-magnetization term and the convection current. The space-like components of the 1-body vector current operator has conventional contributions from the magnetic and electric couplings represented by the magnetic and electric form factors G_M and G_E, respectively.

$$\mathbf{V}_{1B} = \left[\frac{G_E(t)}{m} \boldsymbol{q}_1 - i \frac{G_M(t)}{2m} \big(\boldsymbol{q} \times \boldsymbol{\sigma}_1 \big) \right] \tau_{-,1} \; + \; (1 \to 2) \; , \tag{2.9}$$

where we defined $t = q_0^2 - \mathbf{q}^2 = m_\mu(m_\mu - 2E_\nu)$ as the four-momentum transfer, with $\mathbf{q} = E_\nu \, \hat{z}$ as the three-momentum transfer.

For the 2-body axial current operators, the chiral expansion starts at order Q^{-1}. The dominant contributions generate 2-body axial operators which are shown in the first line of Fig.(2.2), but only diagrams (d) and (e) give non-banishing contribution to the time-like 2-body axial operator Eq.(2.10) due to the choice of unitary phases which are dictated by the matching and the renormalizability to the nuclear force. These diagrams are dependent on the lowest-order unitary transformation. This operator takes the form

$$A^0_{2B:1\pi} = -i \frac{g_A}{4F_\pi^2} \frac{\boldsymbol{k}_1 \cdot \boldsymbol{\sigma}_1}{k_1^2 + m_\pi^2} [\boldsymbol{\tau}_1 \times \boldsymbol{\tau}_2]_- \; + \; (1 \leftrightarrow 2) \; . \tag{2.10}$$

At order Q^0, one encounters the contribution to the 2-body vector-like axial operator that are generated by diagrams (f)-(i) from Fig.(2.2). We have two terms, a two-nucleon contact term Eq.(2.11) and a 1-pion exchange current Eq.(2.12), in which both are pion-pole dependents containing low energy constants (LECs) which are related to the 3-body force. These are represented by c_i and c_D that originated from $\mathcal{L}^2_{\pi N}$ and $\mathcal{L}^1_{\pi NN}$, respectively. The

2-body vector-like axial current operators are described as

$$\mathbf{A}_{2B:cont} = -\frac{c_D}{2F_\pi^2\Lambda_\chi}\left[\boldsymbol{\sigma}_1 - \frac{\boldsymbol{q}(\boldsymbol{\sigma}_1\cdot\boldsymbol{q})}{q^2+{m_\pi}^2}\right]\tau_{-,1} \;+\; (1\leftrightarrow 2)\ , \tag{2.11}$$

where $m_\pi = 138.039$ MeV is the pion mass, $\Lambda_\chi = 700$ MeV is the chiral symmetry breaking scale, and $F_\pi = 92.4$ MeV [8] is the pion decay constant, and

$$\begin{aligned}\mathbf{A}_{2B:1\pi} = \frac{g_A}{2F_\pi^2}\frac{\boldsymbol{\sigma}_1\cdot\boldsymbol{k}_1}{k_1^2+m_\pi^2}\Bigg\{\tau_{-,1}\left[-8c_1 m_\pi^2\frac{\boldsymbol{q}}{q^2+m_\pi^2}+4c_3\left(\boldsymbol{k}_1-\frac{\boldsymbol{q}\,\boldsymbol{q}\cdot\boldsymbol{k}_1}{q^2+m_\pi^2}\right)\right] \\ + c_4[\boldsymbol{\tau}_1\times\boldsymbol{\tau}_2]_-\left(\boldsymbol{k}_1\times\boldsymbol{\sigma}_2-\frac{\boldsymbol{q}\,\boldsymbol{q}\cdot\boldsymbol{k}_1\times\boldsymbol{\sigma}_2}{q^2+m_\pi^2}\right)-\frac{\kappa_v}{4m}[\boldsymbol{\tau}_1\times\boldsymbol{\tau}_2]_-\boldsymbol{q}\times\boldsymbol{\sigma}_2\Bigg\} \;+\; (1\leftrightarrow 2)\ ,\end{aligned} \tag{2.12}$$

where $\boldsymbol{k}_i = \boldsymbol{p}_i' - \boldsymbol{p}_i$, and $q = |\boldsymbol{q}|$ is the magnitude of the three momentum transfer. The constant κ_v is the well known isovector anomalous magnetic moment of the nucleon.

Finally, the last current operator used in our work is the 2-body vector piece Eq.(2.13) which includes the one-pion exchange current operator at leading order Q^{-1} shown in Fig.(2.3). This current operator is proportional to the ratio of the physical LECs g_a/F_π, where $g_A = 1.2754(0.0013)$ [46].

$$\mathbf{V}_{2B:1\pi} = i\frac{g_A^2}{4F_\pi^2}\frac{\boldsymbol{\sigma}_2\cdot\boldsymbol{k}_2}{k_2^2+{m_\pi}^2}\left[\boldsymbol{k}_1\frac{\boldsymbol{\sigma}_1\cdot\boldsymbol{k}_1}{k_1^2+{m_\pi}^2}-\boldsymbol{\sigma}_1\right][\boldsymbol{\tau}_1\times\boldsymbol{\tau}_2]_- \;+\; (1\leftrightarrow 2)\ . \tag{2.13}$$

The axial form factor within the 1-body axial current operators is defined following the parameterization outlined in Ref. [25],

$$G_A(-\mathbf{q}^2) = g_A\left(1-\frac{\langle r_A^2\rangle}{6}\mathbf{q}^2\right)\ , \tag{2.14}$$

where the squared axial radius $\langle r_A^2\rangle$ is reported as 0.46(16) fm^2. The pseudoscalar form factor is written as

$$G_P(-\mathbf{q}^2) = \frac{4m^2}{\mathbf{q}^2+m_\pi^2}g_A\ , \tag{2.15}$$

where it is worth noting that we observed no difference between employing this parameterization and using the form utilized in Ref. [28], which substitutes the factor of g_A with the axial form factor.

For the case of the 1-body vector current operators, we utilize the isovector combination of the magnetic (electric) neutron and proton form factors G_M^n and G_M^p (G_E^n and G_E^p) [40], respectively,

$$G_E = G_E^p - G_E^n \quad \text{and} \quad G_M = G_M^p - G_M^n \ . \tag{2.16}$$

The individual neutron and proton form factors can be written as

$$G_E^p(t) = G_D(t) \quad \text{and} \quad G_E^n(t) = \mu_n \frac{t}{4m^2} \frac{G_D(t)}{1 - t/m^2} \ , \tag{2.17}$$

$$G_M^p(t) = \mu_p G_D(t) \quad \text{and} \quad G_M^n(t) = \mu_n G_D(t) \ . \tag{2.18}$$

where $\mu_p = 2.793$ and $\mu_n = -1.913$ are the magnetic moments of the proton and neutron respectively and are expressed in nuclear magnetons. These form factors are parametrized by the dipole factor denoted as G_D which is defined as

$$G_D(t) = \frac{1}{(1 - t/\Lambda_V^2)^2} \ , \tag{2.19}$$

where $\Lambda_V = 0.833$ GeV. In the following section, there will be a complete discussion and description of the construction of the nuclear matrix elements, which use the electroweak current operators described above. These nuclear matrix elements are the building blocks for the calculation of the processes studied in this document.

Table 2.1: Ordering of chiral electroweak currents, as outlined in Refs. [24, 25]. Current operators labeled with a subscript *static* correspond to contributions where the external current directly interacts with the nucleon. Subscripts $1/m$ indicate relativistic corrections, while subscripts 1π denote contributions incorporating a pion loop.

J^μ	Q^{-3} (LO)	Q^{-1} (NLO)	Q^0 (NNLO)
A^0	-	$A^0_{1B:UT} + A^0_{1B:1/m} + A^0_{2B:1\pi}$	-
A^i	$A^i_{1B:static}$	-	$A^i_{2B:1\pi} + A^i_{2B:cont}$
V^0	$V^0_{1B:static}$	-	-
V^i	-	$V^i_{1B:static} + V^i_{1B:1/m} + V^i_{2B:1\pi}$	-

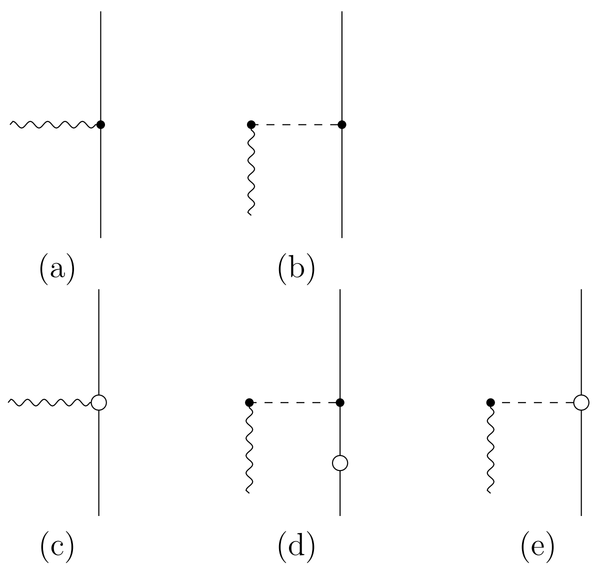

Figure 2.1: Lowest contribution diagrams for the axial 1-body current operators. Diagram (a) refers to $\mathbf{A}_{1B:static}$ at Q^{-3} order, (b) refers to $A^0_{1B:UT}$ at Q^{-1} order. Figures (c), (d), and (e) are $1/m$ relativistic corrections. Diagram (c) contributes to $A^0_{1B:1/m}$ at Q^{-1} order.

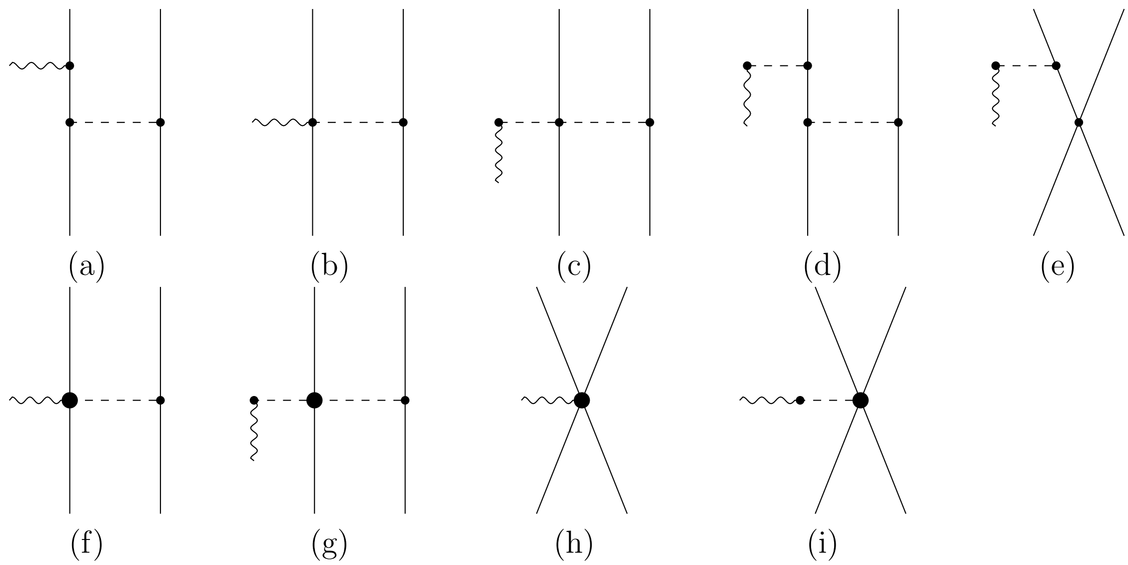

Figure 2.2: Lowest contribution diagrams for axial 2-body current operators. Figures (a) through (e) are the lowest order contributions for the time-like current $A^0_{2B:1\pi}$ at Q^{-1} order. Diagrams (f) through (i) correspond to $\mathbf{A}_{2B:cont}$ and $\mathbf{A}_{2B:1\pi}$ at Q^0 order.

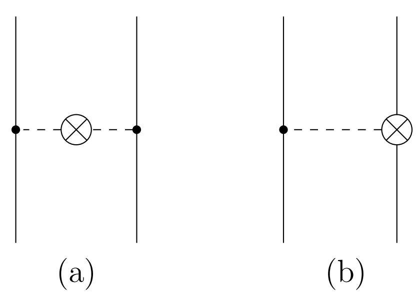

Figure 2.3: Lowest order diagrams for the pion exchange 2-body vector current $\mathbf{V}_{2B:1\pi}$ at Q^{-1} order.

2.3 Nuclear Matrix Elements

In quantum mechanics, the nuclear matrix element describes a system that undergoes a transition from an initial state to a final state due to the presence of external sources. For example, this system can represent a bound state of two nucleons, such as the deuteron nucleus, that gets excited into a scattering state by the absorption of a muon particle or the interaction with any external source that carries enough momentum or energy.

This matrix element is constructed from the current operator $\hat{J}^\mu$, which represents the external source, and wave functions that describe the nuclear system as shown in the expression below,

$$\langle \psi_f P_f m_f | \, \hat{J}^\mu \, | \psi_i P_i m_i \rangle \ , \tag{2.20}$$

where $|\psi_i P_i m_i\rangle$ and $|\psi_f P_f m_f\rangle$ can be either bound or scattering states.

In this work, the muon-deuteron capture (μd-capture) and the hyperfine shift (HPS) in atomic and muonic deuterium processes are composed of currents that contain electroweak contributions from axial plus vector ($A^\mu + V^\mu$) and vector only (V^μ) current operators, respectively.

For either of the two processes examined in this document, the nuclear matrix element can be expressed as $\langle \Psi_s(\boldsymbol{p}) s_1 s_2 | \hat{J}^\mu | \psi_d M_d \rangle$, where the initial state $|\psi_d M_d\rangle$ represents the bound state of the deuteron with wave function ψ_d and total angular momentum projection M_d, and the outgoing state $|\Psi_s(\boldsymbol{p}) s_1 s_2\rangle$ represents a nucleon-nucleon scattering state with wave function Ψ_s and spin projections s_1 and s_2. Now, we represent the deuteron initial state by projecting it to have a spin-1 state, $|1, M_{S_d}\rangle$, and an isospin-zero state, $|0,0\rangle$, and employing a complete set of momentum states. This state is then defined as

$$|\psi_d, M_d\rangle = \sum_{l_d=0,2} \int dp p^2 \, |p(l_d 1); 1, M_d\rangle \otimes |0,0\rangle \, \psi_{l_d}(p) \ , \tag{2.21}$$

and we represent the scattering state with relative momentum $\mathbf{p}$ by employing the identity

$$\langle \Psi_s(\mathbf{p}) s_1 s_2 | = \langle T, M_T | \otimes \langle \mathbf{p} s_1 s_2 | \left[\hat{1} + \hat{t}(E_{nn}) \hat{G}_0(E_{nn}) \right] \ , \tag{2.22}$$

where $\hat{t}$ represents the solution of the Lippmann-Schwinger equation, and G_0 denotes the free two-nucleon Green's function, both evaluated at the energy $E_{nn} = \frac{p^2}{m}$ corresponding to the scattering of two nucleons. The $\langle T, M_T|$ state denotes the isospin state of the two outgoing nucleons.

By using the defined bound and scattering states above, we can construct our nuclear matrix element:

$$\begin{aligned}\langle \Psi_s(\boldsymbol{p}) s_1 s_2 | \hat{J}^\mu | \psi_d M_d \rangle = \langle T, M_T | \otimes \langle \mathbf{p} s_1 s_2 | \hat{J}^\mu | \psi_d, M_d \rangle \\ + \langle T, M_T | \otimes \langle \mathbf{p} s_1 s_2 | \hat{t}(E_{nn}) \hat{G}_0(E_{nn}) \hat{J}^\mu | \psi_d, M_d \rangle \ . \end{aligned} \tag{2.23}$$

The overall nuclear matrix element can be partially wave projected and be re-written as:

$$\begin{aligned}\langle \Psi_s(\boldsymbol{p}) s_1 s_2 | \hat{J}^\mu | \psi_d M_d \rangle = \sum_{\alpha, M_J, m_l, s_z} Y_l^{*m_l}(\hat{p}) \ C^{J,M_J}_{l,m_l;s,s_z} C^{s,s_z}_{\frac{1}{2},s_1;\frac{1}{2},s_2} \Big[\langle p\alpha M_J; T, M_T | \hat{J}^\mu | \psi_d, M_d \rangle \\ + \langle p\alpha M_J; T, M_T | \hat{t}(E_{nn}) \hat{G}_0(E_{nn}) \hat{J}^\mu | \psi_d, M_d \rangle \Big] \ , \end{aligned} \tag{2.24}$$

where $\alpha = \{J, l, s\}$ is the representation of the channel at which the partial-wave state is projected. This state in a general sense can be defined as,

$$|p(ls); J, M_J; T, M_T\rangle = |p(ls)\rangle \otimes |J, M_J\rangle \otimes |T, M_T\rangle \ , \tag{2.25}$$

where p is the magnitude of the outgoing relative momentum of both nucleon, l and s are the orbital angular momentum and spin quantum numbers, and J and M_J are the total angular momentum and total spin projection quantum numbers of the system. The object inside the brackets of Eq. (2.24) can be re-expressed and expanded further:

$$
\begin{aligned}
\langle p\alpha M_J; T, M_T | \left[\hat{1} + \hat{t}(E_{nn})\hat{G}_0(E_{nn})\right] \hat{J}^\mu | \psi_d, M_d\rangle &= \langle p\alpha M_J; T, M_T | \hat{J}^\mu | \psi_d, M_d\rangle \\
+ \sum_{\alpha', M_J', T', M_T'} \int_0^\infty dp' p'^2 \, &\langle p\alpha M_J; T, M_T | \hat{t}(E_{nn})\hat{G}_0(E_{nn}) | p'\alpha' M_J'; T', M_T'\rangle \\
&\times \langle p'\alpha' M_J'; T', M_T' | \hat{J}^\mu | \psi_d, M_d\rangle \ . \qquad (2.26)
\end{aligned}
$$

The equation obtained above is the nuclear plane-wave matrix element, which contains two important expressions. The first term on the right-hand side of the equation is a free nuclear plane-wave matrix element projected onto a plane wave in momentum space as the final state. The second term is a momentum space loop integral decomposed into the contributions of the scattering amplitude or t-matrix and the free plane-wave matrix element. Both expressions involve the contribution of the free nuclear plane-wave matrix element, which, in this formulation, serves as the building blocks of the electroweak processes studied in this document.

At this point, we can generate a general formula to calculate the nuclear matrix elements using both the 1-body and 2-body current operators. Before we proceed with the derivations of the generalized formula for the nuclear matrix elements involving the 1-body and 2-body current operators, we must first define a prescription for the momentum that relates both nucleons in the studied system.

2.3.1 Particle Momentum Definition

In our framework, a momentum space treatment is done to calculate the nuclear matrix element. The current operators are projected into incoming and outgoing momentum of both particles,

$$\langle \boldsymbol{p}_1' | \, \hat{J}^\mu_{1B} \, | \boldsymbol{p}_1 \rangle = \delta^3(\boldsymbol{p}_1' - \boldsymbol{p}_1 - \boldsymbol{q}) J^\mu_{1B}(\boldsymbol{q}) \ , \qquad (2.27)$$

$$\langle \boldsymbol{p}_1' \boldsymbol{p}_2' | \, \hat{J}^\mu_{2B} \, | \boldsymbol{p}_1 \boldsymbol{p}_2 \rangle = \frac{1}{(2\pi)^3} \delta^3(\boldsymbol{p}_1' + \boldsymbol{p}_2' - \boldsymbol{p}_1 - \boldsymbol{p}_2 - \boldsymbol{q}) J^\mu_{2B}(\boldsymbol{q}) \ , \qquad (2.28)$$

whee we use the same normalization prescription as in [25]. The delta function in each current operator ensures momentum conservation, in other words, it is the sum of incoming momenta, and they are factored out from the connected contributions of the scattering amplitude. One advantage of working in momentum space is that observables calculated using this matrix elements are easily obtained without a multipole decomposition.

We define $\boldsymbol{P}_d$, $\boldsymbol{P}_s$ as the center-of-mass momentum of the deuteron and two-nucleon scattering states, respectively. The momenta $\boldsymbol{p}_1$ and $\boldsymbol{p}_2$ are the momenta for particle one and two, and $\boldsymbol{p}$ and $\boldsymbol{p}'$ as the relative incoming and outgoing relative momenta respectively. If particle 1 and 2 interact with an external source such as a neutrino or a photon, then the momentum that describes this external source is the 3-vector momentum transfer $\boldsymbol{q}$.

For the center-of-mass momentum of the deuteron that relates particle 1 and 2 we have

$$\boldsymbol{P}_d = \boldsymbol{p}_1 + \boldsymbol{p}_2 \ , \tag{2.29}$$

and by momentum conservation the center-of-mass momentum of the scattering state is

$$\boldsymbol{P}_s = \boldsymbol{p}'_1 + \boldsymbol{p}'_2 = \boldsymbol{p}_1 + \boldsymbol{p}_2 + \boldsymbol{q} = \boldsymbol{P}_d + \boldsymbol{q} \ . \tag{2.30}$$

By introducing the Jacobi momentum prescription, we can re-write the momentum $\boldsymbol{p}_1$ ($\boldsymbol{p}'_1$) and $\boldsymbol{p}_2$ ($\boldsymbol{p}'_2$) of both nucleon in terms of the relative momentum $\boldsymbol{p}$ ($\boldsymbol{p}'$). For the incoming momentum we have

$$\boldsymbol{p} = \frac{1}{2}(\boldsymbol{p}_1 - \boldsymbol{p}_2) \tag{2.31}$$

$$\begin{aligned} \boldsymbol{p}_1 &= \frac{\boldsymbol{P}_d}{2} + \boldsymbol{p} \ , \\ \boldsymbol{p}_2 &= \frac{\boldsymbol{P}_d}{2} - \boldsymbol{p} \ . \end{aligned} \tag{2.32}$$

Now if the center-of-mass of the deuteron is taken to be at rest then $\boldsymbol{P}_d = 0$ then

$$
\begin{aligned}
\boldsymbol{p}_1 &= \boldsymbol{p} \ , \\
\boldsymbol{p}_2 &= -\boldsymbol{p} \ ,
\end{aligned}
\tag{2.33}
$$

and for the outgoing momentum we write

$$
\begin{aligned}
\boldsymbol{p}'_1 &= \frac{\boldsymbol{P}_s}{2} + \boldsymbol{p}' = \frac{\boldsymbol{q}}{2} + \boldsymbol{p}' \ , \\
\boldsymbol{p}'_2 &= \frac{\boldsymbol{P}_s}{2} - \boldsymbol{p}' = \frac{\boldsymbol{q}}{2} - \boldsymbol{p}',
\end{aligned}
\tag{2.34}
$$

At this stage, by using the above expressions, Eq.(2.27) and Eq.(2.28) can be re-written in terms of the incoming and outgoing relative momentum of both nucleons. For the 1-body current operator we get

$$
\langle \boldsymbol{p}' | \hat{J}^{\mu}_{1B}(1) | \boldsymbol{p} \rangle = J^{\mu}_{1B}(1)(\boldsymbol{p}', \boldsymbol{p}) \delta^3(\boldsymbol{p}' - \boldsymbol{p} - \boldsymbol{q}/2) \ , \tag{2.35}
$$

$$
\langle \boldsymbol{p}' | \hat{J}^{\mu}_{1B}(2) | \boldsymbol{p} \rangle = J^{\mu}_{1B}(2)(\boldsymbol{p}', \boldsymbol{p}) \delta^3(\boldsymbol{p}' - \boldsymbol{p} + \boldsymbol{q}/2) \ , \tag{2.36}
$$

and for the 2-body current operator we have

$$
\langle \boldsymbol{p}' \boldsymbol{P}_s | \hat{J}^{\mu}_{2B}(i,j) | \boldsymbol{p} \boldsymbol{P}_d \rangle = J^{\mu}_{2B}(i,j)(\boldsymbol{p}', \boldsymbol{p}) \delta^3(\boldsymbol{P}_s - \boldsymbol{P}_d - \boldsymbol{q}) \ , \tag{2.37}
$$

and dropping the delta function we obtain

$$
\langle \boldsymbol{p}' | \hat{J}^{\mu}_{2B}(i,j) | \boldsymbol{p} \rangle = J^{\mu}_{2B}(i,j)(\boldsymbol{p}', \boldsymbol{p}) \ , \tag{2.38}
$$

where the functional expressions $J^{\mu}_{1B}(i)(\boldsymbol{p}', \boldsymbol{p})$, and $J^{\mu}_{2B}(i,j)(\boldsymbol{p}', \boldsymbol{p})$ are defined in Eq.(2.5) containing axial and vector contributions.

2.3.2 Plane Wave Calculation for 1-body Current Operator

In the calculation of the nuclear matrix element, one can decompose the system into the contributions of partially wave projected matrix elements, as shown in Eq. (2.26) allowing us to generate a general formulation of these reduced expressions. We start by neglecting final state interactions. Using the J^{μ}_{1B} current, we proceed to derive nuclear matrix elements in momentum space as follows:

$$\langle nn| \hat{J}^{\mu}_{1B}(1) |\psi_d, M_d\rangle = \langle p'(ls); J, M_J; T, M_T| \hat{J}^{\mu}_{1B}(1) |\psi_d, M_d\rangle \ , \tag{2.39}$$

where p is the magnitude of the relative momentum between particules with momenta p_1 and p_2, and it is expressed as, $\boldsymbol{p} = \frac{1}{2}(\boldsymbol{p}_1 - \boldsymbol{p}_2)$, and inserting a complete set of momentum states we have

$$\begin{aligned}\langle nn| \hat{J}^{\mu}_{1B}(1) |\psi_d, M_d\rangle &= \\ &\langle T, M_T| \otimes \langle S, M_S| \otimes \int d\hat{\boldsymbol{p}}' \sum_{m_l} C^{J,M_J}_{l,m_l;S,M_J-m_l} Y^{*m_l}_{l}(\hat{\boldsymbol{p}}') \langle \boldsymbol{p}'| \hat{J}^{\mu}_{1B}(1) |\psi_d, M_d\rangle\end{aligned} \tag{2.40}$$

Now solving for the right most piece of Eq. (2.40), by using Eq. (2.21) and inserting a complete set of momentum states, we get:

$$\begin{aligned}\langle \boldsymbol{p}'| \hat{J}^{\mu}_{1B}(1) |\psi_d, M_d\rangle = \int d^3\boldsymbol{p} \sum_{l_d=0,2} \sum_{m_{l_d}} C^{1,M}_{l_d,m_{l_d};1,M-m_{l_d}} Y^{m_{l_d}}_{l_d}(\hat{\boldsymbol{p}}) \\ \times \langle \boldsymbol{p}'| \hat{J}^{\mu}_{1B}(1) |\boldsymbol{p}\rangle \otimes |1, M_{S_d}\rangle \otimes |0,0\rangle\, \psi_{l_d}(p)\end{aligned} \tag{2.41}$$

Finally, putting everything together and solving the delta functions found in the current operators we obtain a generalized formula for the nuclear matrix element using the 1-body current operator

$$
\begin{aligned}
\langle nn|\, \hat{J}^{\mu}_{1B}(1)\, |\psi_d, M_d\rangle = &\int d\hat{\boldsymbol{p}}' \sum_{m_l} C^{J,M_J}_{l,m_l;S,M_J-m_l} Y^{*m_l}_{l}(\hat{\boldsymbol{p}}') \\
&\times \sum_{l_d=0,2} \sum_{m_{l_d}} C^{1,M}_{l_d,m_{l_d};1,M-m_{l_d}} Y^{m_{l_d}}_{l_d}(\widehat{\boldsymbol{p}' - \boldsymbol{q}}/2)\psi_{l_d}(|\boldsymbol{p}' - \boldsymbol{q}/2|) \\
&\times \langle T, M_T| \otimes \langle S, M_J - m_l| \otimes \langle \boldsymbol{p}'|\, \hat{J}^{\mu}_{1B}(1)\, |\boldsymbol{p}' - \boldsymbol{q}/2\rangle \otimes |1, M - m_{l_d}\rangle \otimes |0, 0\rangle \quad (2.42)
\end{aligned}
$$

The results obtained in this research were calculated using nuclear matrix elements evaluated at the different required outgoing momenta in the scattering states and the 3-vector momentum transfer $\boldsymbol{q}$. In the following sections, we will discuss the calculation of uncertainty estimates for muon capture on the deuteron and the hyperfine shift in atomic and muonic deuterium. We will also detail how we implemented the previously derived nuclear matrix element to explain these processes and the relationships necessary to calculate relevant observables.

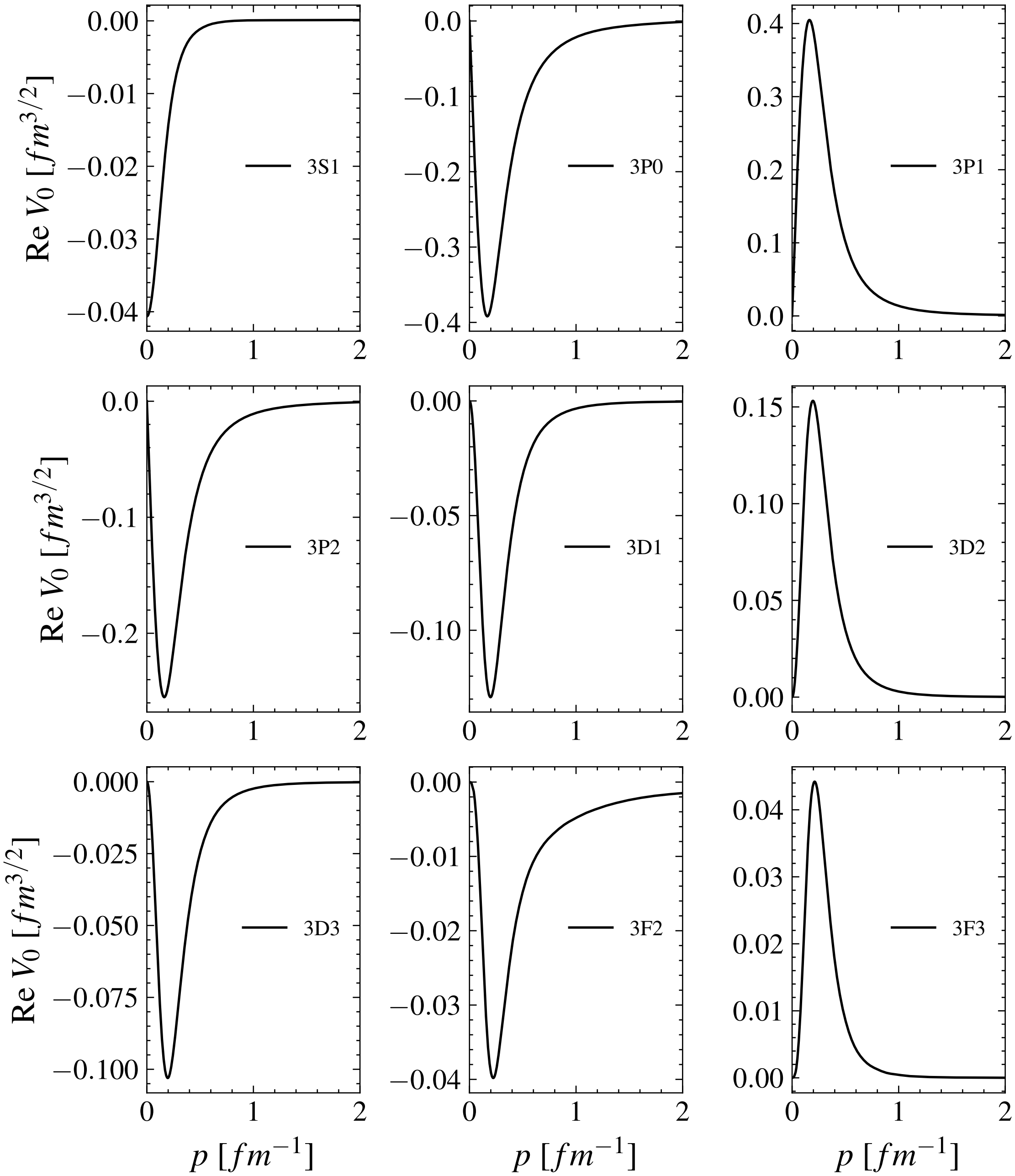

Figure 2.4: Results for matrix elements (Real part) using the time-like 1-body vector current operator Eq. (A.51) with no final state interactions for different partial wave channels up to $L = 3$. Matrix elements were evaluated for $q = 50$ MeV and q-angular values of $\theta_q = 0.5$ and $\phi_q = 0.5$.

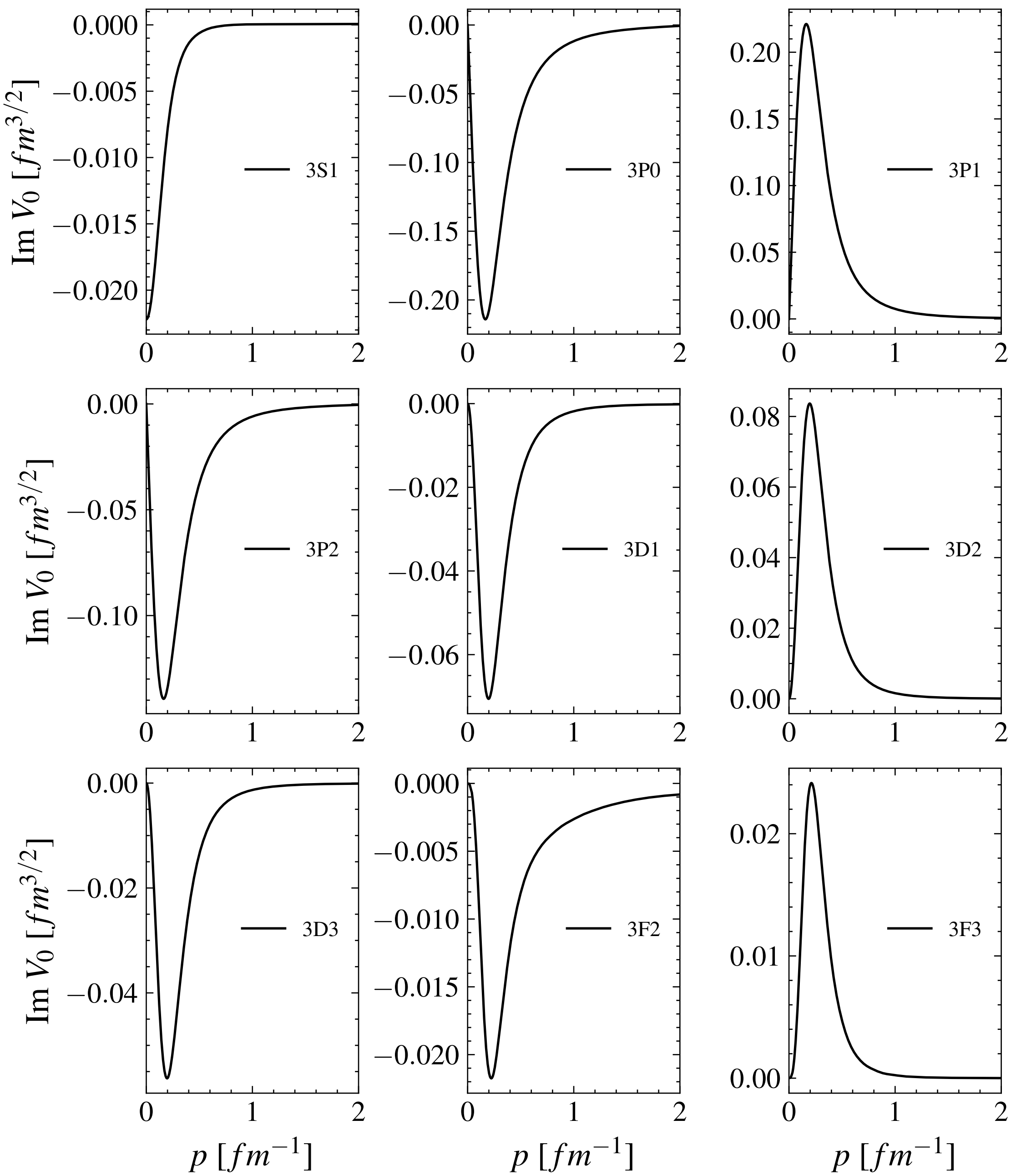

Figure 2.5: Results for matrix elements (Imaginary part) using the time-like 1-body vector current operator Eq. (A.51) with no final state interactions for different partial wave channels up to $L = 3$. Matrix elements were evaluated for $q = 50$ MeV and q-angular values of $\theta_q = 0.5$ and $\phi_q = 0.5$.

Chapter 3

Uncertainty Estimates for Muon Capture on the Deuteron

3.1 Introduction

Muon capture on the deuteron is an important process in nuclear physics, providing valuable insights into the interactions and dynamics of fundamental particles within atomic nuclei. In this process, a negatively charged muon (μ^-) is captured by a deuteron ^{2}H (d), leading to the formation of a muonic deuterium bound state. Upon capture, the muon-deuteron system splits into two neutrons (n) and a neutrino (ν_μ). This is a reaction governed by the weak interaction. This is shown in Eq.(3.1)

$$\mu^- + d \to \nu_\mu + n + n \ . \tag{3.1}$$

The capture rate of muons on deuterons is a critical parameter for understanding the weak force and the behavior of nucleons under its influence. This rate is influenced by various factors, including the interactions mediated by electroweak currents, the energy states of the muon-deuteron system, and the dynamics of the resulting nuclear products. By studying the capture rate, we can gain deeper insights into the properties of the weak interaction and the structure of the deuteron.

In this study, we aim to explore the theoretical framework that describes the capture process using the framework of χEFT, highlighting the role of electroweak currents in facilitating the reaction and the mechanisms by which the muon-deuteron system splits into two neutrons and a neutrino.

Our main goal is to determine uncertainty estimates by analyzing capture rate results using several chiral interactions with chiral electroweak currents truncated at NNLO. By systematically varying the chiral interactions and incorporating different truncations of the electroweak currents, we aim to quantify the theoretical uncertainties and provide a robust assessment of the capture rates. This comprehensive approach will enhance our understanding of the underlying physics and improve the predictive power of χEFT in describing muon capture on the deuteron. By conducting a thorough uncertainty analysis, this work aims to establish a solid theoretical basis for interpreting forthcoming experimental data from the MuSun collaboration. Additionally, we will compare our theoretical predictions with existing theoretical and experimental data on the μd-capture rate, helping to validate and refine our theoretical models. Results of this work were published in [6].

3.2 Muon Capture Process and Kinematics

The μd-capture process can be described by the contribution of 1- and 2-body processes as shown by the two diagrams in Fig.(3.1). In the 1-body diagram on the left side, only one nucleon takes part in the reaction by being attached to the lepton line that describes the neutrino production. In the 2-body process, the second diagram on the right side, both nucleons take part in the interaction with the lepton. The 1- and 2-body mechanisms are shown in the form of the filled circle. These mechanisms are determined by the 1- and 2-body currents that operate between initial and final states that are described, in our case, by the deuteron bound state and the neutron-neutron scattering state, as seen in Fig.(3.2).

Now, we can examine the kinematics of the μd-capture process by omitting the mass of the resulting neutrino and neglecting the small binding energy of the muon atom. Considering momentum and energy conservation, we can express Eq.(3.1) as follows:

$$m_\mu + m_d = E_\nu + \sqrt{m_n^2 + \boldsymbol{p}_1^2} + \sqrt{m_n^2 + \boldsymbol{p}_2^2} \ , \tag{3.2}$$

$$\boldsymbol{p}_1 + \boldsymbol{p}_2 + \boldsymbol{p}_\nu = 0 \ , \tag{3.3}$$

where m_n, m_d, and m_μ are the corresponding masses of the neutron, deuteron, and muon respectively. E_ν is the neutrino energy, and $\boldsymbol{p}_\nu$, $\boldsymbol{p}_1$, and $\boldsymbol{p}_2$ are the momenta of the produced neutrino, and the outgoing momentum of nucleons 1 and 2 (both neutrons) respectively . In this work, the kinematics of μd-capture process are treated non-relativistically. Subsequently, the equation for energy conservation is simplified by expanding the square root terms on the right-hand side of Eq.(3.2) and retaining the first two terms of the expansion. This results in

$$m_\mu + m_d = E_\nu + 2m_n + \frac{\boldsymbol{p}_1^2}{2m_n} + \frac{\boldsymbol{p}_2^2}{2m_n} \ . \tag{3.4}$$

By introducing the relative Jacobi momentum, $\boldsymbol{p} = \frac{1}{2}(\boldsymbol{p}_1 - \boldsymbol{p}_2)$, and reformulating non-relativistic energy conservation to establish a connection between the momenta of both nucleons during the calculation of the nuclear matrix element, then Eq.(3.4) can be expressed and re-arranged to give

$$\frac{\boldsymbol{p}^2}{m_n} = m_\mu + m_d - E_\nu - 2m_n - \frac{E_\nu^2}{4m_n} \ , \tag{3.5}$$

where $\boldsymbol{p}^2/m_n$ is the relative energy E_{nn} in the two-neutron system. This energy is used as input to the Lippman-Schwinger equation for our final neutron-neutron state. In the following section, we will discuss the capture rate derivation and its calculation using the previously derived general prescription for the nuclear matrix element.

Figure 3.1: Muon capture process representation with 1-body currents (left figure) and 2-body currents (right figure)

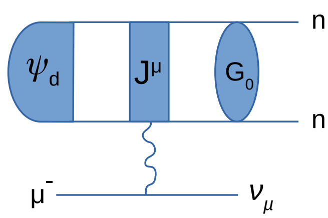

Figure 3.2: Muon capture process

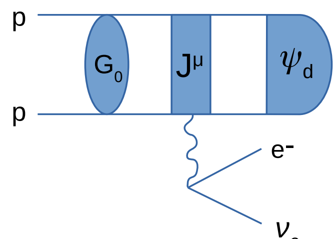

Figure 3.3: p-p fusion process

3.3 Capture Rate Calculation

To establish the foundational components required for computing the capture rate, we initially create the momentum-space matrix elements of the current operators, as discussed in the preceding section. These elements are essential for evaluating the corresponding transition amplitude, which is defined as

$$T_{fi} = \frac{G_V}{\sqrt{2}} \psi_{\mu d}(0) \sum_{s_\mu, M_d} C^{f,f_z}_{1/2,s_\mu;1M_d} \; l^{\sigma -} \left\langle \Psi_s(\boldsymbol{p}) s_1 s_2 | \hat{J}_\sigma | \psi_d M_d \right\rangle \;, \tag{3.6}$$

where G_V= 1.14939×10^{-5} GeV^{-2} is the Fermi coupling constant obtained from Ref.[28]. Here, $\psi_{\mu d}(0) = [\alpha_{\rm em} m_\mu m_d/(m_\mu + m_d)]^{3/2}/\pi^{1/2}$ represents the ground state wavefunction of the muonic-deuterium atom at the origin, and $\alpha_{\rm em}$ is the fine-structure constant. The leptonic tensor in Eq. (3.6) is expressed as

$$l^\sigma = \bar{u}(k', h)\gamma^\sigma(1 - \gamma_5)u(k, s_\mu) \;, \tag{3.7}$$

with lepton spinors $u(k, h)$. Moreover, we incorporate the angular momentum coupling between the muon and deuteron spin by including a Clebsch-Gordan coefficient $C^{f,f_z}_{1/2,s_\mu;1M_d}$ in Eq. (3.6), enabling the calculation of capture rates for the two hyperfine states $f = 1/2$ and $f = 3/2$.

To determine the capture rate, we must integrate over the solid angle of $\boldsymbol{p}$. To establish a connection between the capture rate and the matrix elements involving partial-wave projected final states, we represent the transition amplitude of Eq. (3.6) in terms of spherical harmonics.

$$\begin{aligned} T_{fi} = \frac{G}{\sqrt{2}} \psi_{\mu d}(0) \sum_{s_\mu, M_d} C^{f,f_z}_{1/2,s_\mu;1,M_d} l^\sigma \\ \times \sum_{\alpha, m_l, s_z} Y_l^{*m_l}(\hat{p}) C^{J,M_J}_{l,m_l;s,s_z} C^{s,s_z}_{1/2,s_1;1/2,s_2} \langle p\alpha| \, (\hat{1} + \hat{t}G_0) \hat{J}_\sigma \, |\psi_d M_d\rangle \;. \end{aligned} \tag{3.8}$$

In this context, α denotes the channel defined by the quantum numbers $\alpha \equiv \{(ls); JM_J\}$. Our analysis covers rates up to $J \leq 2$, incorporating channels ${}^1S_0$, ${}^3P_0$, ${}^3P_1$, ${}^3P_2$, ${}^1D_2$, and ${}^3F_2$, all of which make significant contributions to the overall muon capture rate. To calculate the unpolarized rate, we sum over s_1 and s_2, which represent the spin projections of the outgoing nucleons. Additionally, we integrate over the solid angle of $\boldsymbol{p}$, providing angle-averaged squared matrix elements that can be directly associated with the total capture rate

$$\Gamma^f_{\mu d} \propto \overline{|T_{fi}|^2} = \int d\hat{p} \frac{1}{2f+1} \sum_{f_z} \sum_{s_1,s_2} |T_{fi}|^2 \ . \tag{3.9}$$

The resulting expression for the angle-averaged squared matrix element, including the nuclear matrix element, is given by

$$\overline{|T_{fi}|^2} = \frac{G_V^2}{2} |\psi_{\mu d}(0)|^2 \frac{1}{2f+1} \sum_{f_z} \sum_{\alpha} \left| \sum_{s_\mu, M_d} C^{f,f_z}_{1/2,s_\mu;1,M_d} \ l^\sigma \left\langle p\alpha \right| (\hat{1} + \hat{t}G_0) \hat{J}_\sigma \left| \psi_d M_d \right\rangle \right|^2 \ . \tag{3.10}$$

Ultimately, the momentum distribution of the capture rate can be computed by performing the phase space integral over the momentum of the outgoing neutrino, resulting in

$$\frac{d\Gamma^f_{\mu d}}{dp} = \frac{2}{\pi} E_\nu^2 p^2 \frac{m_n}{E_\nu + 2m_n} \overline{|T_{fi}|^2} \ . \tag{3.11}$$

The neutrino's energy in Eq. (3.11) is determined by the expression: $E_\nu = \frac{1}{2(m_\mu + m_d)} \left[(m_\mu + m_d)^2 - 4(m_n^2 + p^2) \right]$. Integrating Eq. (3.11) over the relative momentum p from 0 to $p_{\max} = \left[\frac{(m_\mu + m_d)^2}{4} - m_n^2 \right]^{1/2}$ allows us to compute the total capture rate $\Gamma^f_{\mu d}$ at a particular hyperfine state f. For our capture rate calculations, We employ 120 points for p to ensure convergence in our results.

3.4 Results for the Muon Capture Rate

To compute the μd-capture rate, we initially utilize a set of 42 interactions truncated at NNLO. These interactions incorporate NN and NNN LECs that were fitted in Ref. [8] across seven distinct values of the regulator cutoff Λ. The range spans from 450 to 600 MeV in 25 MeV increments. The fitting process is simultaneous to data on pion-nucleon interactions, energies, and charge radii of ^{2,3}H and ^{3}He, the 1-body quadrupole moment of ^{2}H, the relative β-decay half-life of ^{3}H, and six different datasets of NN scattering with various truncations in the NN scattering energy, $T_{\rm lab}$. These interactions, referred to as NNLOsim, underwent a re-fit to address an equation error concerning the relationship between c_D and the axial two-body contact current. Subsequently, they were utilized to compute muon capture into the ^{1}S$_0$ nn-channel [1].

In this context, we have computed the muon capture rate for five additional partial wave channels, which contribute significantly to the overall rate and are therefore essential for comparison with experimental data. While the NNLOsim interactions encompass uncertainties stemming from cutoff variation, sensitivity to input datasets, and fitting errors that consider correlations among the LECs, it is also valuable to constrain the pion-nucleon LECs to precise values determined in Refs. [21, 41] through Roy-Steiner analysis. To accomplish this, we utilize the LO, NLO, and NNLO interactions outlined in Ref. [44], referred to as LO$_{\rm RS450}$, NLO$_{\rm RS450}$, and NNLO$_{\rm RS450}$. These interactions were fitted against the Granada database [34, 35, 36], along with the nn effective range parameters [26], where the pion-nucleon constants are fixed at the central values of the NLO pion-nucleon coupling constants of Ref. [41]. The different orders of the RS450 interactions provide a means to compare the truncation error in the potential to the uncertainties in NNLOsim, which serves as a crucial self-consistency check for χEFT [13].

The results for the capture rates, including those from the doublet and quartet channels and other channels truncated at various total nuclear angular momenta $J_{\rm max}$, obtained using differently regulated NNLOsim and 1-body currents only, are presented in Tbl. 3.1. Each entry represents the average over the set of NNLOsim interactions with different $T_{\rm lab}$ truncations at a specific regulator Λ. The last row displays the corresponding results reported in Ref. [11], which were obtained using wave functions from χEFT potentials and standard 1-body operators. Tbl. 3.2 presents the results for the doublet capture rate, obtained using NNLOsim potentials alongside 1- and 2-body currents. Additionally, the table includes the corresponding results obtained with the RS450 interactions at LO, NLO, and NNLO, as well as experimental data from Refs. [43, 5, 29, 7], and theoretical findings from Refs. [2, 28, 11]. The various columns now detail the contribution from each individual channel, with the final column providing the total capture rate.

To illustrate the influence of incorporating final state interactions, we present in Figs. 3.4 and 3.5 the differential capture rate. The top figures depict the scenario without final state interactions, while the bottom figures include these interactions. These rates are plotted against the magnitude of the relative momentum p between the outgoing neutrons for the doublet and quartet hyperfine-state channels, respectively. Each solid line of varying color represents the contribution from individual partial wave channels of the nn state. The dashed line represents the total differential capture rate. The widths of these lines are determined by calculating the partial differential capture rate with the 42 different NNLOsim interactions. It is evident that for both the doublet and quartet rates, capture into the ${}^1S_0$ channel dominates, yet several other channels also make significant contributions. The overall differential capture rates for the doublet and quartet channels qualitatively align with the findings in Ref. [11], which utilized chiral wave functions and phenomenological two-body currents.

In Fig. 3.6, the top (bottom) figure displays the complete rate $\Gamma^{1/2}_{\mu d}$ for capture originating from the doublet (quartet) channel, computed across the 42 distinct chiral interactions. To derive our central rates, we average the outcomes from all 42 interactions within each channel. The range between the smallest and largest rates, in conjunction with the respective central value, provides an estimation of the rate and its associated uncertainty. This is indicated as the primary error in Eq. (3.12) below. Additionally, we incorporate the new value of the uncertainty in the axial radius, $r_A^2 = 0.46 \pm 0.16$ fm^2 [20], by computing the rates at both the upper and lower bounds of this uncertainty range. This contributes to the second (symmetric) error in Eq. (3.12) below. Consequently, for the rates pertaining to the doublet and quartet channels, we obtained the following

$$\begin{aligned}
\left[\Gamma_{\mu d}^{1/2}\right]_{\text{sim}} &= (396.33^{+0.94}_{-1.85} \pm 4.4)\text{s}^{-1} \ , \\
\left[\Gamma_{\mu d}^{3/2}\right]_{\text{sim}} &= (12.38^{+0.34}_{-0.25} \pm 0.04)\text{s}^{-1} \ .
\end{aligned} \tag{3.12}$$

A more robust approach to obtain the uncertainty of an EFT calculation involves examining the convergence pattern of an observable order by order. Here, we will adopt the approach outlined in Ref. [15] by expressing the capture rate for either the doublet or quartet channel as

$$\Gamma_{\mu d} = \Gamma_{\mu d}^{\text{LO}} \sum_{n=0}^{3} c_n \left(\frac{p}{\Lambda_b}\right)^n \ , \tag{3.13}$$

Here, $\Gamma_{\mu d}^{\text{LO}}$ represents the leading order result for the muon capture rate, either in the doublet or quartet hyperfine state, while p signifies the intrinsic momentum scale of the issue at hand, and Λ_b stands for the breakdown scale. An approximation of the truncation is then derived by computing $(p/\Lambda_b)^4 \max(|c_0|, |c_2|, |c_3|)$. By utilizing the RS450 results from Tbl. 3.2 and Tbl. 3.3 to acquire the c_i coefficients, assuming the pion mass for the momentum scale p, and setting $\Lambda_b = 500$ MeV, we obtain an uncertainty of 7.6 s^{-1} for the overall doublet channel capture rate and 0.47 s^{-1} for the total quartet capture rate.

Taking these findings as they are, the μd-capture result from this methodology yields

$$\begin{aligned}
\left[\Gamma_{\mu d}^{1/2}\right]_{\text{RS450}} &= (401.90 \pm 7.6 \pm 4.4)\ \text{s}^{-1} \ , \\
\left[\Gamma_{\mu d}^{3/2}\right]_{\text{RS450}} &= (12.24 \pm 0.47 \pm 0.04)\ \text{s}^{-1} \ ,
\end{aligned} \tag{3.14}$$

where the initial uncertainty mentioned represents the EFT truncation error, while the second one arises from the axial radius uncertainty. The uncertainty for the doublet estimate aligns well with the uncertainty determined using a similar approach for capture into the $^1\text{S}_0$ channel in Ref. [1], as well as with the variation in the final outcomes between NNLOsim and $\text{NNLO}_{\text{RS450}}$ interactions. To obtain a conclusive suggestion for the μd-capture rates in both the doublet and quartet hyperfine states, we compute the average of the values provided in

Eqs. (3.12) and (3.14), incorporating the uncertainties outlined in Eq. (3.14)

$$\Gamma_{\mu d}^{1/2} = (399.1 \pm 7.6 \pm 4.4)\ \mathrm{s}^{-1}\ , \tag{3.15}$$

$$\Gamma_{\mu d}^{3/2} = (12.31 \pm 0.47 \pm 0.04)\ \mathrm{s}^{-1}\ . \tag{3.16}$$

Our findings, encompassing the quoted truncation error, align with prior theoretical investigations as reported in Refs. [11, 27], though they display a slight disparity with the findings presented in Ref. [2]. Additionally, our results for capture into the doublet ${}^1S_0$ channel alone demonstrate close agreement with a recent computation outlined in Ref. [9]. Furthermore, our assessment of doublet capture resonates favorably with experimental observations [43, 5, 29, 7], although the substantial uncertainties in these observations hinder conclusive remarks regarding the efficacy of the utilized currents.

3.5 Conclusion

In this study, we have computed the overall μd-capture rates from both the doublet ($f = 1/2$) and quartet ($f = 3/2$) hyperfine-state channels, utilizing χEFT interactions at order NNLO along with consistent NNLO currents. After combining results from various interactions, we obtain capture rates of $\Gamma_{\mu d}^{1/2} = 399.1 \pm 7.6 \pm 4.4\ \mathrm{s}^{-1}$ for the doublet channel, and $\Gamma_{\mu d}^{3/2} = 12.31 \pm 0.47 \pm 0.04\ \mathrm{s}^{-1}$ for quartet channel. The initial uncertainty stems from the convergence pattern in Eq.(3.13) of the total capture rates, while the second error reflects the axial radius uncertainty. The recent substantial axial radius uncertainty [20] poses a significant challenge, making it difficult to establish a dependable connection between experimental measurements and the nuclear Hamiltonian. Nevertheless, the considerable capture rate uncertainty in the doublet channel due to inherent errors in χEFT underscores the potential for experimental results to offer crucial insights into the nuclear Hamiltonian.

The findings regarding both the differential and total capture rates align well with existing theoretical forecasts [2, 27, 11, 28], with only a minor deviation observed in the ${}^1D_2$ doublet capture rate as reported in [27]. As far as we're aware, this study marks the inaugural application of EFT in computing the quartet capture rate.

This and preceding studies underscore the significance of muon capture calculations on light nuclei as a tool for probing the nuclear Hamiltonian. Its dynamics are influenced by intricate interplays among current matrix elements and rely heavily on precise characterizations of nuclear bound and scattering properties. A comprehensive initiative aimed at mitigating experimental uncertainties, coupled with capture rate computations across various processes, holds promise for constraining additional short-range counterterms evident in the vector and axial currents at order Q [24, 25]. Moreover, a comprehensive analysis of radiative corrections, such as the Wγ box contribution, appears both desirable and feasible. This would be particularly valuable in assessing the significance of contributions that extend beyond one-nucleon radiative corrections and their sensitivity to nuclear structure effects [17]. As a final statement, it is worth mentioning that this work has been cited by Gnech *et al*. in which a Bayesian analysis of muon capture on deuteron in χEFT for the doublet rate was calculated [16]. Their results are consistent with the analysis done in our study.

Table 3.1: Displayed are the muon capture rates for the doublet ($f = 1/2$) and quartet ($f = 3/2$) channels, computed using NNLOsim interactions [8] and NNLO 1-body currents exclusively. Columns represent rates with channel inclusions up to $J = 0$, $J = 1$, or $J = 2$. Each row corresponds to results obtained with different momentum cutoffs Λ, averaged across six NNLOsim interactions with varied $T^{\text{lab}}_{\text{max}}$ truncations at the specified cutoff. The final row offers results from Ref. [11] for comparison.

$g_A = 1.2754$	Capture Rate 1B $\Gamma^{f}_{\mu d}(s^{-1})$					
	$f = 1/2$			$f = 3/2$		
NNLOsim	$^1S_0$	$J \leq 1$	$J \leq 2$	$^1S_0$	$J \leq 1$	$J \leq 2$
$\Lambda = 450$ MeV	248.73	305.97	386.27	6.64	7.66	11.23
$\Lambda = 475$ MeV	248.14	305.95	386.25	6.62	7.66	11.26
$\Lambda = 500$ MeV	247.61	305.80	386.12	6.61	7.66	11.29
$\Lambda = 525$ MeV	247.14	305.57	385.90	6.60	7.66	11.31
$\Lambda = 550$ MeV	246.73	305.34	385.68	6.59	7.65	11.32
$\Lambda = 575$ MeV	246.37	305.10	385.47	6.58	7.65	11.33
$\Lambda = 600$ MeV	246.07	304.90	385.28	6.57	7.64	11.33
A. Elmeshneb [11]	240.5	303.3	383.4	6.38	7.73	11.31

Table 3.2: Displayed are the results for $\Gamma_{\mu d}^{1/2}(s^{-1})$ in the doublet hyperfine state, presented in units of s^{-1}. The labels NNLOsim and $\mathrm{NNLO_{RS}}$ indicate the order Q^3 nn interactions utilized to compute deuteron and nn wave functions, respectively. The various columns denote results corresponding to the inclusion of different partial wave channels.

Capture Rate for Doublet State 1B+2B $\Gamma_{\mu d}^{1/2}(s^{-1})$							
NNLOsim	$^1S_0$	$^3P_0$	$^3P_1$	$^3P_2$	$^1D_2$	$^3F_2$	Total
$\Lambda = 450$ MeV	255.04	15.27	45.55	71.88	7.75	0.97	396.46
$\Lambda = 500$ MeV	254.44	16.02	45.72	71.93	7.75	0.98	396.84
$\Lambda = 550$ MeV	253.48	16.32	45.84	72.00	7.75	0.98	396.37
$\Lambda = 600$ MeV	252.09	16.47	45.89	72.06	7.76	0.98	395.25
$\mathrm{NNLO_{RS450}}$ ($\Lambda = 450$ MeV)	$^1S_0$	$^3P_0$	$^3P_1$	$^3P_2$	$^1D_2$	$^3F_2$	Total
LO	189.36	13.60	30.23	58.98	5.88	0.70	298.75
NLO	250.92	19.28	47.08	72.05	7.91	1.00	398.24
NNLO	254.39	19.23	47.07	72.31	7.89	1.01	401.90
Theoretical Results:							
S. Ando *et al.* [2]	386±4						
L.E. Marcucci *et al.* [27]	399±3						
A. Elmeshneb [11]	401						
A. Gnech [16]	395±10						
Experimental Results:							
I.-T. Wang *et al.* [43]	365±96						
A. Bertin *et al.* [5]	445±60						
M. Martino [29]	470±29						
M. Cargnelli *et al.* [7]	409±40						

Table 3.3: The table presents results for $\Gamma_{\mu d}^{3/2}(s^{-1})$ in the quartet hyperfine state ($f = 3/2$). Results in this table used the approach of partial wave decomposition and are listed for each respective partial wave up to $J \leq 2$. The labels NNLOsim and $\mathrm{NNLO_{RS}}$ signify the order Q^3 nn interaction employed in computing the deuteron and nn wave functions, respectively.

Capture Rate for Quartet State 1B+2B $\Gamma_{\mu d}^{3/2}(s^{-1})$							
NNLOsim	$^1S_0$	$^3P_0$	$^3P_1$	$^3P_2$	$^1D_2$	$^3F_2$	Total
$\Lambda = 450$ MeV	6.72	0.54	0.50	1.53	2.58	0.34	12.21
$\Lambda = 500$ MeV	6.71	0.57	0.51	1.54	2.68	0.34	12.35
$\Lambda = 550$ MeV	6.69	0.58	0.51	1.56	2.75	0.35	12.44
$\Lambda = 600$ MeV	6.68	0.59	0.51	1.56	2.79	0.35	12.48
$\mathrm{NNLO_{RS450}}$ ($\Lambda = 450$ MeV)	$^1S_0$	$^3P_0$	$^3P_1$	$^3P_2$	$^1D_2$	$^3F_2$	Total
LO	2.77	0.40	0.21	0.64	1.29	0.13	5.44
NLO	6.63	0.75	0.52	1.48	1.84	0.33	11.55
NNLO	6.72	0.75	0.51	1.53	2.39	0.34	12.24
Theoretical Results:							
A. Elmeshneb [11]	12.7						
A. Gnech [16]	13.3–13.8						

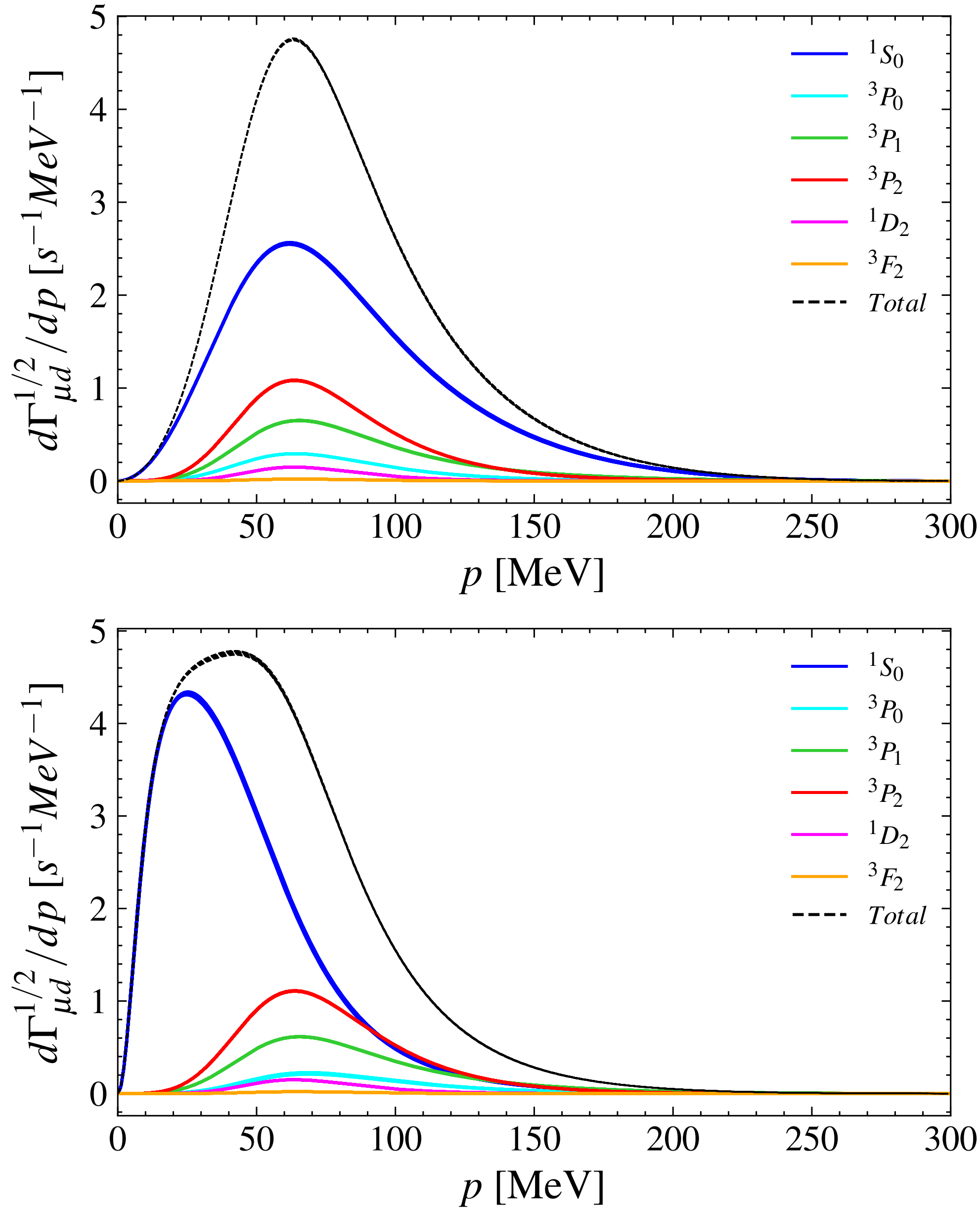

Figure 3.4: Top figure: Results for $d\Gamma^{1/2}_{\mu d}/dp$ for the doublet hyperfine state, computed in the absence of final state interactions. Bottom figure: Results for $d\Gamma^{1/2}_{\mu d}/dp$ for the doublet hyperfine state, factoring in final state interactions. The solid lines represent outcomes for various nn-partial-wave channels, while the dashed lines depict the total differential capture rate.

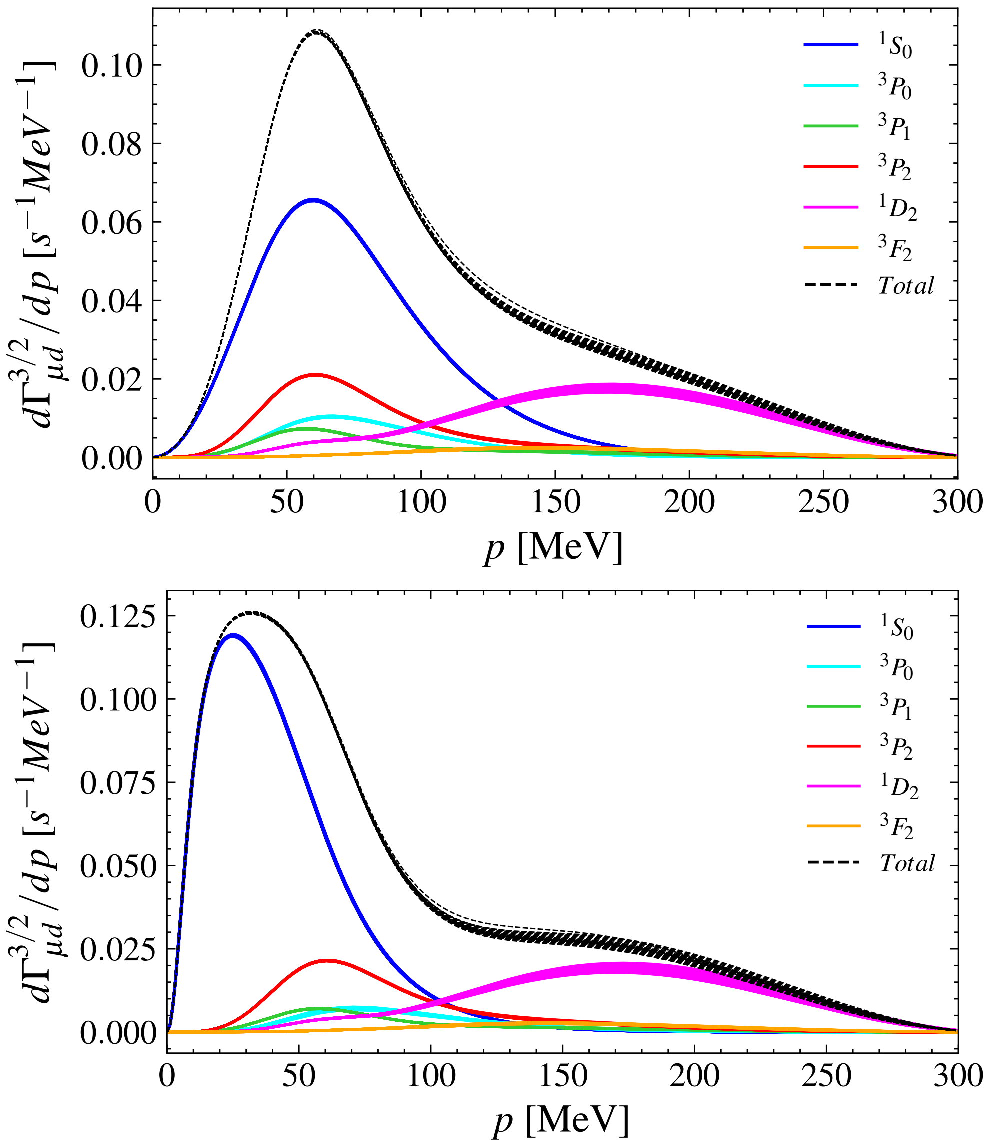

Figure 3.5: Top figure: Results for $d\Gamma_{\mu d}^{3/2}/dp$ for the quartet hyperfine state, computed in the absence of final state interactions. Bottom figure: Results for $d\Gamma_{\mu d}^{3/2}/dp$ for the quartet hyperfine state, factoring in final state interactions. The solid lines represent outcomes for various nn-partial-wave channels, while the dashed lines depict the total differential capture rate.

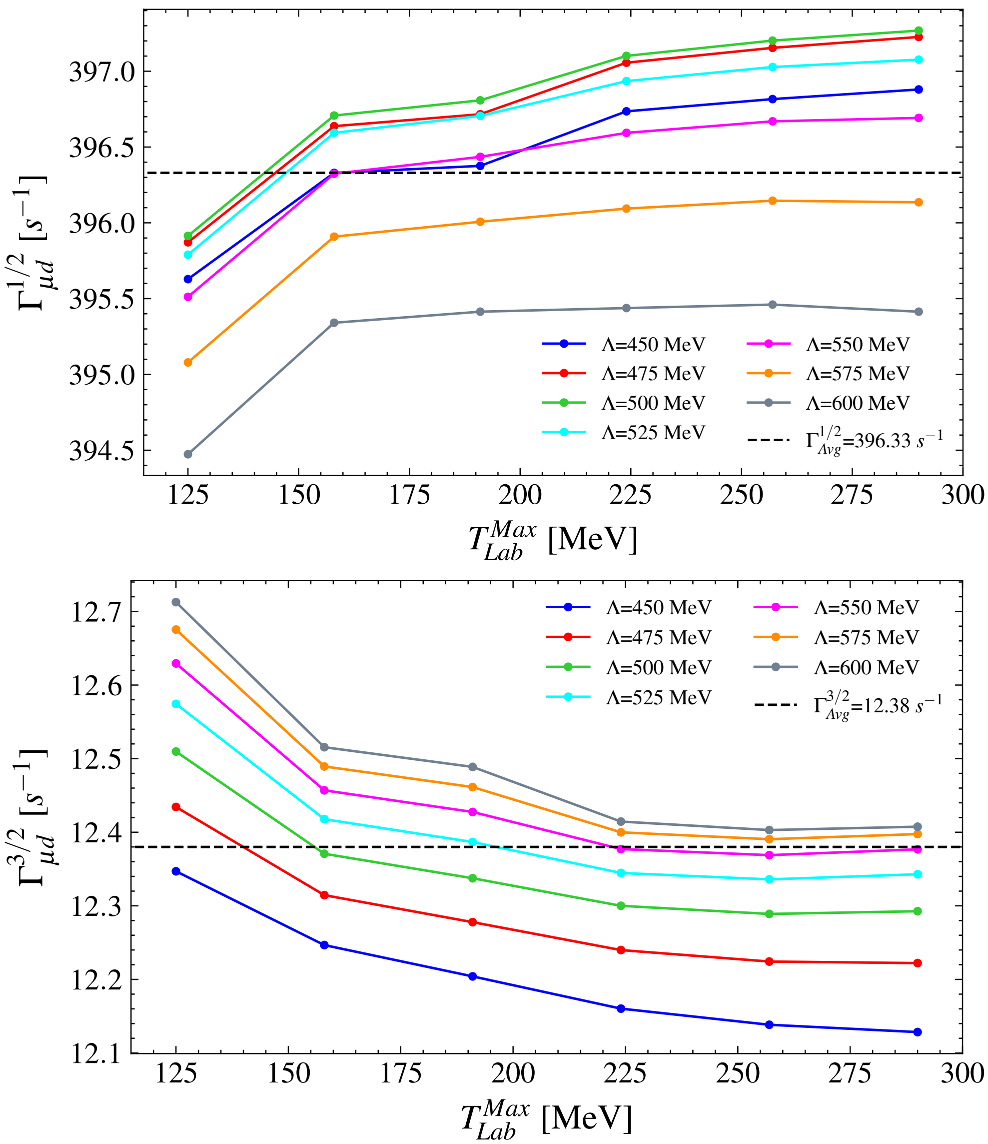

Figure 3.6: Top figure: Results for $\Gamma^{1/2}_{\mu d}$ pertaining to the doublet hyperfine state. Bottom figure: Results for $\Gamma^{3/2}_{\mu d}$ pertaining to the quartet hyperfine state. The results encompass contributions from the nn-channels up to total angular momentum $J \leq 2$. Each data point corresponds to the outcome derived at each of the 42 NNLOsim interactions at order Q^3, sourced from Ref. [8]. Connecting lines link results with identical cutoffs to aid visualization.

Chapter 4

The hyperfine shift in atomic and muonic deuterium

4.1 Introduction

The hyperfine structure in atomic and muonic deuterium is an important topic in nuclear and particle physics, providing deep insights into the fundamental interactions between particles within an atomic nucleus. Hyperfine splitting, which results from the interaction between the magnetic moments of the nucleus and a lepton in the atom, reveals intricate details about the forces at play at very small scales. In particular, the study of hyperfine shifts in both atomic and muonic deuterium provides a unique and precise probe into the nature of nucleon-nucleon interactions, enabling us to explore the effective forces that govern nuclear structure and test the predictions of χEFT in a high-precision regime against measurements obtained using high precision laser spectroscopy on light [19, 45, 39, 18] and muonic atoms [3, 38, 10] and theoretical predictions obtained using pionless EFT [23] and Quantum Electrodynamics (QED) [45, 22].

In this study, we employ χEFT by using chiral interactions and electroweak current operators truncated at NLO to model and derive the necessary nuclear matrix elements for calculating the hyperfine energy shifts in both atomic and muonic deuterium systems.

We will discuss the derivation of these matrix elements, highlighting the role of electroweak currents and their interactions with the nucleons. Our goal is to determine the hyperfine energy shifts with high accuracy, thereby contributing to the broader understanding of nuclear interactions and the validation of χEFT as a robust framework for nuclear physics. Through this research, we aim to offer new insights into the fundamental forces that shape the behavior of atomic ^2H $(e^- + d)$ and muonic μ^2H $(\mu^- + d)$ systems, advancing both theoretical and experimental frontiers in the field.

4.2 Hyperfine splitting Process

Hyperfine splitting, or hyperfine energy shifts, refers to the splitting of atomic energy levels due to the magnetic interaction between the magnetic dipole moments of the nucleus, in this case the deuteron, and the electron or muon particle. This interaction causes the energy levels of the atom to split into closely spaced sub-levels, resulting in observable energy shifts.

In atomic deuterium, the deuteron has a magnetic moment arising from the spins of its constituent nucleons. The electron, orbiting at a relatively large distance from the nucleus, also has a magnetic moment. The hyperfine interaction between these magnetic moments causes a small splitting of the atomic energy levels. This splitting is relatively weak because the electron is far from the nucleus, resulting in a weaker magnetic interaction [37].

In muonic deuterium, the electron is replaced by a muon, which is about 200 times heavier than the electron. This increased mass means the muon orbits much closer to the nucleus compared to the electron in atomic deuterium. As a result, the magnetic dipole-dipole interaction between the muon and the deuteron is much stronger, leading to more significant hyperfine energy shifts. The closer proximity of the muon to the nucleus enhances the magnetic interaction, resulting in larger and more easily observable energy splittings [30].

This magnetic dipole-dipole interaction depends on the relative orientation of the spins of the deuteron and the interacting particle. The interaction energy depends on the alignment of these spins, leading to different energy states for different spin alignments. The energy levels of the atomic or muonic atom split into multiple sub-levels due to this interaction.

The degree of splitting is influenced by the strength of the magnetic interaction, which is stronger for the muon in muonic deuterium than for the electron in atomic deuterium.

In QED, the magnetic moments interact through the exchange of virtual photons. Hyperfine splitting or hyperfine energy shifts in atomic and muonic deuterium are actually constrained by the effects of nuclear structure. This is due to the mechanism known as 2-photon exchange (TPE) process [23]. Here in this study, we focus our calculations on inelastic TPE or in other words nuclear polarizability which happens due to nuclear virtual excitations.

Using χEFT interactions and vector current operators truncated at NLO, we aim to evaluate the TPE contributions in ^2H and μ^2H. In the next sections, we discuss about the two-photon exchange process and its kinematics that will lead to the calculation of the energy shifts of both study cases.

4.2.1 Two-Photon Exchange Theory

Derivations for the two-photon exchange theory have been previously obtained in [23]. It is essential to review these derivations to gain insight into the two-photon exchange mechanism.

The hyperfine splitting of a $ns_{1/2}$ state is actually dominated by contact interactions that occur between the nuclear spin denoted as $\mathbf{I}$ and the lepton spin $\boldsymbol{\sigma}_l/2$. This contact interaction can be defined as:

$$H_I = \frac{2\pi\alpha g_m}{3m_l m}\phi_n^2(0)\boldsymbol{\sigma}^{(l)} \cdot \mathbf{I} \ , \tag{4.1}$$

where m_l and m are the masses of the lepton and the nucleon respectively, g_m is the nuclear magnetic g-factor, α is fine structure constant. The expression defined as $\phi_n^2(0) = (Z\alpha m_R)^3/(n^3\pi)$ is the squared of the wave function at origen of the atomic $ns_{1/2}$ state with a reduced mass m_R between the lepton and the nucleus. The contribution of this contact interaction can be obtained by taking its expectation value

$$E_F = \langle (ns_{1/2}, N_0, I)F, M_F| \, H_I \, |(ns_{1/2}, N_0, I)F, M_F\rangle \ , \tag{4.2}$$

where E_F is known as the Fermi-contact hyperfine energy, F and M_F are the total angular momentum and its z-projection of the atomic hyperfine structure state respectively, and $|N_0 I\rangle$ is the nuclear ground state with spin I.

Now, the TPE is driven by the exchange of two virtual photons between the lepton and the nucleus. The operator that describes this process is given by

$$H_{2\gamma} = i(4\pi\alpha)^2\phi_n^2(0)\int \frac{d^4q}{(2\pi)^4}\frac{\eta_{\mu\nu}(q)T^{\mu\nu}(q,-q)}{(q^2+i\epsilon)^2(q^2-2m_l q_0+i\epsilon)} \ , \tag{4.3}$$

where T and η are the nuclear and lepton tensors. Only the contribution from the lepton tensor, which contain spin dependency, contributes to the hyperfine splitting. From this dependency, we can construct the TPE polarizability operators that are defined as:

$$H_{pol}^{(0)} = \frac{i\alpha^2\phi_n^2(0)}{2\pi m_l^2}\int d\omega \int \frac{d^3q}{\boldsymbol{q}^4} h^{(0)}(\omega,|\boldsymbol{q}|)\boldsymbol{\sigma}^{(l)}\cdot\{\boldsymbol{q}\times\mathbf{V}(-\boldsymbol{q}),V_0(\boldsymbol{q})\}\delta(\omega-\omega_N) \ , \tag{4.4}$$

$$H_{pol}^{(1)} = \frac{i\alpha^2\phi_n^2(0)}{2\pi m_l^2}\int d\omega \int \frac{d^3q}{\boldsymbol{q}^2} h^{(1)}(\omega,|\boldsymbol{q}|)\boldsymbol{\sigma}^{(l)}\cdot\{\mathbf{V}(-\boldsymbol{q})\times\mathbf{V}(\boldsymbol{q})\}\delta(\omega-\omega_N) \ , \tag{4.5}$$

where V_0 is the time-like vector current operator, $\mathbf{V}=\mathbf{V_c}+\mathbf{V_m}$ is the vector-like vector operator containing the already mentioned convection and magnetic vector current contributions. These vector current operators correspond to Eq. (2.6) and Eq. (2.9). The variable ω_N is the excitation energy of the nuclear state, and the kernels $h^{(0,1)}$ are defined as

$$h^{(0)}(\omega,q) = \left(2+\frac{\omega}{E_q}\right)\left[\frac{E_q^2+m_l^2+E_q\omega}{(E_q+\omega)^2-m_l^2}\right] - \frac{2q+\omega}{q+\omega} \ , \tag{4.6}$$

$$h^{(1)}(\omega,q) = \frac{1}{E_q}\left[\frac{E_q^2+m_l^2+Eq\omega}{(E_q+\omega)^2-m_l^2}\right] - \frac{1}{q+\omega} \ , \tag{4.7}$$

with

$$E_q = \sqrt{q^2+m_l^2} \ . \tag{4.8}$$

Eq. (4.4) is the transition matrix that contains the time-like current operator at order LO and the vector-like vector operator at NLO in anticommutation. In Eq. (4.5), we encounter the vector-vector-like current operators both at NLO and in commutation.

The two-photon exchange polarizability corrections to the atomic hyperfine structure is evaluated by obtaining the expectation value of $H_{pol}^{(0,1)}$ on the atomic hyperfine state $|(ns_{1/2}, N_0, I)F, M_F\rangle$ and express this quantity in ratios of E_F.

$$E_{pol}^{(0,1)} = \langle (ns_{1/2}, N_0, I)F, M_F|\, H_{pol}^{(0,1)}\, |(ns_{1/2}, N_0, I)F, M_F\rangle \ . \tag{4.9}$$

$$E_{pol}^{(0,1)} = \delta_{pol}^{(0,1)}\ E_F \tag{4.10}$$

where:

$$\delta_{pol}^{(0)} = \frac{6\alpha m}{\pi m_l g_m I}\int_{\omega_{th}}^{\infty} d\omega \int_0^{\infty} dq\ h^{(0)}(\omega, q) S^{(0)}(\omega, q)\ , \tag{4.11}$$

$$\delta_{pol}^{(1)} = -\frac{6\alpha m}{\pi m_l g_m I}\int_{\omega_{th}}^{\infty} d\omega \int_0^{\infty} dq\ h^{(1)}(\omega, q) S^{(1)}(\omega, q)\ , \tag{4.12}$$

and where $S^{(0,1)}(\omega, q)$ are respond functions and are defined as:

$$S^{(0)}(\omega, q) = \int \frac{d\hat{q}}{4\pi}\frac{1}{q^2} Im\big(\langle N_0; I, I|\, V_0(-\boldsymbol{q})\big[\boldsymbol{q}\times \boldsymbol{V}_m(\boldsymbol{q})\big]_3\, |N_0; I, I\rangle\, \big)\delta\bigg(\omega - B_d - \frac{\boldsymbol{q}^2}{4m} - \frac{\boldsymbol{p}^2}{m}\bigg)\ , \tag{4.13}$$

$$S^{(1)}(\omega, q) = \int \frac{d\hat{q}}{4\pi}\epsilon^{3jk} Im\big(\langle N_0; I, I|\, \boldsymbol{V}_{c,j}(-\boldsymbol{q})\boldsymbol{V}_{m,k}(\boldsymbol{q})\, |N_0; I, I\rangle\, \big)\delta\bigg(\omega - B_d - \frac{\boldsymbol{q}^2}{4m} - \frac{\boldsymbol{p}^2}{m}\bigg)\ , \tag{4.14}$$

The addition from contributions $E_{pol}^{(0)}$ and $E_{pol}^{(1)}$, Eq. (4.9), provides the total two-photon exchange polarizability contribution as shown in the expression below

$$E_{pol} = E_{pol}^{(0)} + E_{pol}^{(1)}\ . \tag{4.15}$$

4.2.2 TPE Kinematics

As in the μd-capture case, we picture a deuteron nucleus interacting with an incoming photon. Upon contact, this interaction excites both the neutron and proton particles, which are then expelled with specific energies from their initial reference point. This interaction can be described by the following expression:

$$d + \gamma \to p + n \ , \tag{4.16}$$

where d is the deuteron nucleus, γ is the incoming photon, and p and n are the proton and neutron particles respectively. Now by conservation of energy, we can write our process as

$$E_d + E_\gamma = \sqrt{m_n^2 + \boldsymbol{p}_1^2} + \sqrt{m_p^2 + \boldsymbol{p}_2^2} \ . \tag{4.17}$$

If we take the deuteron system at rest then its momentum $\boldsymbol{p}_d = 0$, and expanding the terms inside the square root and taking only the leading orders then the energy conservation equation becomes

$$m_n + m_p - B_d + E_\gamma = m_n + \frac{\boldsymbol{p}_1^2}{2m_n} + m_p + \frac{\boldsymbol{p}_2^2}{2m_p} \ , \tag{4.18}$$

$$-B_d + E_\gamma = \frac{\boldsymbol{p}_1^2}{2m_n} + \frac{\boldsymbol{p}_2^2}{2m_p} \ . \tag{4.19}$$

Now the momentum conservation equation is defined as

$$\boldsymbol{p}_\gamma = \boldsymbol{p}_1 + \boldsymbol{p}_2 \ , \tag{4.20}$$

where $\boldsymbol{p}_\gamma$ is the incoming momentum of the photon and $\boldsymbol{p}_1$ and $\boldsymbol{p}_2$ are the momenta of the neutron and proton particles respectively. If we introduce the relative Jacobi momentum $\boldsymbol{p} = \frac{1}{2}(\boldsymbol{p}_1 - \boldsymbol{p}_2)$, then we can re-write the momentum of the proton and neutron as follows:

$$\boldsymbol{p}_1 = \frac{\boldsymbol{p}_\gamma}{2} + \boldsymbol{p} \ , \tag{4.21}$$

$$\boldsymbol{p}_2 = \frac{\boldsymbol{p}_\gamma}{2} - \boldsymbol{p} \ . \tag{4.22}$$

Now inserting Eq.(4.21) and Eq.(4.22) into Eq.(4.19), the energy equation becomes

$$-B_d + E_\gamma = \frac{\boldsymbol{p}_\gamma^2}{8m_n} + \frac{\boldsymbol{p}^2}{2m_n} + \frac{\boldsymbol{p}_\gamma^2}{8m_p} + \frac{\boldsymbol{p}^2}{2m_p} \ . \tag{4.23}$$

If we define $\mu = \frac{m_n m_p}{m_n + m_p}$, which is the reduced mass between the mass of the proton and neutron, then the above equation is written as

$$-B_d + E_\gamma = \frac{\boldsymbol{p}_\gamma^2}{8\mu} + \frac{\boldsymbol{p}^2}{2\mu} \ . \tag{4.24}$$

By approximating the mass of the neutron and proton by m, which is the nucleon mass $m_p \approx m_n \approx m$, then the reduced mass becomes $\mu = m/2$, and if we define $E_\gamma \to \omega$ as the excitation energy of the deuteron and $\boldsymbol{p}_\gamma \to \boldsymbol{q}$ as the 3-momentum transfer of the incoming photon, then we obtain

$$-B_d + \omega = \frac{\boldsymbol{q}^2}{4m} + \frac{\boldsymbol{p}^2}{m} \ . \tag{4.25}$$

At this point, we can use Eq. (4.25) to defined the 2-nucleon scattering relative momenta $p = |\boldsymbol{p}|$ as follows

$$p = \sqrt{m(\omega - B_d) - q^2/4} \tag{4.26}$$

From the above definition, we can extract the minimum excitation energy of the deuteron in the inelastic TPE process, which is given by $\omega_{th} = B_d + q^2/4m$. This result is used as the minimum limit in the excitation energy integral encountered in Eq. (4.11) and Eq. (4.12).

4.3 Two-Photon Exchange Calculation

To obtain the foundational components required for computing the two-photon exchange process, we need to obtain the momentum-space matrix elements of the electromagnetic current operators. This is done similarly as we did for the muon capture process case. These elements are essential for evaluating the response functions Eq. (4.13) and Eq. (4.14), which are proportional to the 2-photon exchange polarizability contribution.

The electromagnetic vector current operators in the response functions $S^{(0,1)}$ are projected onto an initial and final state defined by the deuteron bound state. This state can be re-defined as $|N_0; I, I\rangle \to |\psi_d, M_d\rangle$, where $I = J_d = 1$ is the total nuclear spin of the deuteron, and its z-component projection is taken to be at its maximum value $M_d = 1$.

From here, we take $S^{(0,1)}$ and insert a complete set of intermediate states in the continuum which can be defined as

$$\sum_{s1,s2}\sum_{T,M_T}\int d^3\boldsymbol{p}\,|\Psi_s(\mathbf{p})s_1s_2\rangle\,\langle\Psi_s(\mathbf{p})s_1s_2| \;\;, \tag{4.27}$$

where the state $|\Psi_s(\mathbf{p})s_1s_2\rangle$ is defined as in Eq. (2.22). The response functions are re-written as follows:

$$S^{(0)}(\omega,q) = \sum_{s_1,s_2}\sum_{T,M_T}\int\frac{d\hat{q}}{4\pi}\frac{1}{q^2}\int d^3\boldsymbol{p}\;Im\big(\,\langle\psi_d,1|\,V_0(-\boldsymbol{q})\,|\Psi_s(\mathbf{p})s_1s_2\rangle$$
$$\langle\Psi_s(\mathbf{p})s_1s_2|\,\big[\boldsymbol{q}\times\boldsymbol{V}_m(\boldsymbol{q})\big]_3\,|\psi_d,1\rangle\,\big)\,\delta\!\left(\omega - B_d - \frac{\boldsymbol{q}^2}{4m} - \frac{\boldsymbol{p}^2}{m}\right)\;, \tag{4.28}$$

$$S^{(1)}(\omega,q) = \sum_{s_1,s_2}\sum_{T,M_T}\int\frac{d\hat{q}}{4\pi}\epsilon^{3jk}\int d^3\boldsymbol{p}\;Im\big(\,\langle\psi_d,1|\,\boldsymbol{V}_{c,j}(-\boldsymbol{q})\,|\Psi_s(\mathbf{p})s_1s_2\rangle$$
$$\langle\Psi_s(\mathbf{p})s_1s_2|\,\boldsymbol{V}_{m,k}(\boldsymbol{q})\,|\psi_d,1\rangle\,\big)\,\delta\!\left(\omega - B_d - \frac{\boldsymbol{q}^2}{4m} - \frac{\boldsymbol{p}^2}{m}\right)\;, \tag{4.29}$$

where the matrix operator with negative momentum, $\langle\psi_d, M_d|\,V^\mu(-\boldsymbol{q})\,|\Psi_s(\mathbf{p})s_1s_2\rangle$, indicates the de-excitation or transition of a nuclear intermediate state to the bound state of the deuteron. This state is equivalent to the complex conjugate of the matrix element in the inverse process $\langle\Psi_s(\mathbf{p})s_1s_2|\,V^\mu(\boldsymbol{q})\,|\psi_d, M_d\rangle$. These matrix elements are derived in A.[—].

At this point, we have the building blocks to obtain a final expression for the response functions $S^{(0,1)}(\omega,q)$. By looking $\delta^{(0,1)}_{TPE}$, it is more convenient to integrate over ω, this means we have to work out the delta function in the response functions $S^{(0,1)}$ and then integrate over the momenta p, for this we do:

$$\Delta E = \frac{\boldsymbol{q}^2}{4m} + \frac{\boldsymbol{p}^2}{m} + B_d - \omega \tag{4.30}$$

Now using the identity

$$\delta(g(x)) = \frac{\delta(x - x_0)}{\left|\frac{dg(x)}{dx}\right|_{x=x_0}} \tag{4.31}$$

we can work the delta functions in Eq.(4.28) and (4.29) as follows

$$\delta(\Delta E) = \frac{\delta(p - p_0)}{\left|\frac{d(\Delta E)}{dp}\right|_{p=p_0}} \tag{4.32}$$

$$\delta(\Delta E) = \frac{m}{2p_0}\delta(p - p_0) \tag{4.33}$$

where p_0 can be obtained by setting $\Delta E = 0$ and solve for p, then we get

$$p_0 = \sqrt{m(\omega - B_d) - q^2/4}\ , \tag{4.34}$$

which is the same expression as in Eq. (4.26). Now using the above delta function over p, and using Eq.(4.28), we get

$$S^{(0)}(\omega, q) = \frac{mp_0}{8\pi q^2} \sum_{s_1,s_2} \sum_{T,M_T} \int d\hat{q} \int d\hat{p}\ Im\Big(\langle \psi_d, 1 | \, V_0(-\boldsymbol{q}) \, | \Psi_s(\boldsymbol{p}_0) s_1 s_2 \rangle$$
$$\times \langle \Psi_s(\boldsymbol{p}_0) s_1 s_2 | \left[\boldsymbol{q} \times \boldsymbol{V}_m(\boldsymbol{q}) \right]_3 | \psi_d, 1 \rangle \Big)\ . \tag{4.35}$$

Now if we partial wave decompose the intermediate state as in (2.24), sum over spins s_1 and s_2, and integrate over the solid angle of $\boldsymbol{p}$, then the response function $S^{(0)}$ becomes

$$S^{(0)}(\omega, q) = \frac{mp_0}{8\pi q^2} \sum_{T,M_T} \sum_{\alpha,M_J} \int d\hat{q}\ Im\Big(\langle p_0 \alpha | \, (\hat{1} + \hat{t}G_0) V_0(\boldsymbol{q}) \, | \psi_d, 1 \rangle^*$$
$$\times \langle p_0 \alpha | \, (\hat{1} + \hat{t}G_0) \big[\boldsymbol{q} \times \boldsymbol{V}_m(\boldsymbol{q}) \big]_3(\boldsymbol{q}) \, | \psi_d, 1 \rangle \Big)\ . \tag{4.36}$$

Similarly, we get for Eq.(4.29)

$$S^{(1)}(\omega,q) = \frac{mp_0}{8\pi}\sum_{T,M_T}\sum_{\alpha,M_J}\int d\hat{q}\;\epsilon^{3jk} Im\Big(\langle p_0\alpha|\,(\hat{1}+\hat{t}G_0)\boldsymbol{V}_{c,j}\,|\psi_d,1\rangle^* \times \langle p_0\alpha|\,(\hat{1}+\hat{t}G_0)\boldsymbol{V}_{m,k}\,|\psi_d,1\rangle\Big)\ . \quad (4.37)$$

The summation that runs through the indices j and k, which represent indices of the Cartesian coordinate system, can be handled as follows

$$\epsilon^{3jk}A_jB_k = A_1B_2 - A_2B_1 = A_xB_y - A_yB_x\ . \quad (4.38)$$

Now changing the Cartesian coordinate system to spherical coordinate system, we do the following

$$C_x = \frac{1}{\sqrt{2}}(C_{-1} - C_{+1})\ ,$$
$$C_y = \frac{i}{\sqrt{2}}(C_{-1} + C_{+1})\ ,$$
$$C_z = C_0\ .$$

By using the above change of basis system, we obtain for A and B:

$$A_xB_y - A_yB_x = i(A_{-1}B_{+1} - A_{+1}B_{-1})\ .$$

From the above, we can define $S^{(1)}(\omega,q)$ as

$$S^{(1)}(\omega,q) = \frac{mp_0}{8\pi}\sum_{T,M_T}\sum_{\alpha,M_J}\int d\hat{q}\; Im\Big[i\Big(\langle p_0\alpha|\,(\hat{1}+\hat{t}G_0)\boldsymbol{V}_{c,-1}\,|\psi_d,1\rangle^*\langle p_0\alpha|\,(\hat{1}+\hat{t}G_0)\boldsymbol{V}_{m,+1}\,|\psi_d,1\rangle - \langle p_0\alpha|\,(\hat{1}+\hat{t}G_0)\boldsymbol{V}_{c,+1}\,|\psi_d,1\rangle^*\langle p_0\alpha|\,(\hat{1}+\hat{t}G_0)\boldsymbol{V}_{m,-1}\,|\psi_d,1\rangle\Big)\Big]\ . \quad (4.39)$$

In the following section, we will provide analysis and results for the two-photon exchange polarizability contributions.

4.4 Results for TPE

For the calculation of the hyperfine energy shifts, we use the Idaho interaction of Ref. [12] truncated at NNNLO. We denote this interaction as NNNLO_{Idaho}. Relevant matrix elements were calculated using only the one-body vector current operator, as derived in Ref. [25].

We show the results for polarizability contributions to TPE for atomic ^2H and muonic-deuterium μ^2H systems from the $1S$ and $2S$ states at the different partial wave contributions up to $L \leq 3$. These results are obtained with the NNNLO_{Idaho} and 1-body vector current operators only in Tbl. 4.1. Here, we calculate the theoretical values of $E^{(0)}_{pol}$, $E^{(1)}_{pol}$, and their sum E_{pol}. The different columns give the contribution for each individual channel included in the calculation with the last one giving the total polarizability contribution to TPE.

Similar to the μd-capture process, we demonstrate the impact of the inclusion of the individual partial-wave contributions by calculating the response functions $S^{(0,1)}(\omega, q)$ as a function of the excitation energy ω of the deuteron at different fixed momentum q values: 5, 50, and 100 MeV in Fig. 4.1 and Fig. 4.2. Additionally, to illustrate the influence of incorporating final state interactions, we calculated these response functions $S^{(0,1)}(\omega, q)$ without final state interactions (left column figures) and with final state interactions (right column figures) in Fig. 4.1 and Fig. 4.2 respectively. The different colored solid lines denote the cumulative contributions from the different partial waves included in this calculation. Each line gives the result for the response function with channels included up to a nuclear orbital angular momentum $L = 0$ (S), 1 (P), 2 (D), and 3 (F). It is evident the sensitivity of $S^{(0,1)}(\omega, q)$ functions at the different q values and different partial waves. For the response function $S^{(0)}(\omega, q)$ computed without final-state interactions, the S-wave dominates at lower q values, while the P-waves start to dominate in contribution strength at higher q values. For results of $S^{(0)}(\omega, q)$ with final state interaction, we can appreciate that the P-wave gives the largest contribution while others are only a minimal but sizable contribution of the overall response function calculation. For the response function $S^{(1)}(\omega, q)$ computed without and with final state interaction the P-wave always dominates at any q value while other partial waves remain minimal contributions of the overall response functions calculation.

A summary to the total polarizability contribution to TPE for $E_{pol}^{(0,1)}$ and their sum E_{pol} obtained using the NNNLO$_{Idaho}$ interaction and 1-body vector current operators is shown in Tbl. 4.2. Here, we show results for atomic ^2H (columns 2 and 3) and muonic-deuterium μ^2H (columns 4 and 5) for both $1S$ and $2S$ states. The last rows show the theoretical results obtained in Ref. [23]. The total polarizability contribution to TPE E_{pol} for atomic and muonic-deuterium from the $1S$ and $2S$ states are in qualitative agreement with the results shown in Ref. [23] that were obtained using a pionless EFT framework.

4.5 Conclusion

In this study, we have calculated hyperfine energy shifts by determining the total polarizability contribution to the two-photon exchange (TPE) from the $1S$ and $2S$ states for atomic and muonic deuterium systems. We employed chiral EFT NNNLO$_{Idaho}$ interaction with vector current operators truncated at NLO. Using the NNNLO$_{Idaho}$ interaction, we found the total polarizability for the atomic system to be $E_{pol}(1S) = 125.90$ kHz and $E_{pol}(2S) = 15.74$ kHz, while for the muonic deuterium system, we obtained $E_{pol}(1S) = 3.34$ meV and $E_{pol}(2S) = 0.42$ meV.

In comparison with the results obtained in Ref. [23], the polarizability contributions $E_{pol}(1S)$ and $E_{pol}(2S)$ for muonic deuterium μ^2H show percentage differences of 16.8%, while the polarizability contribution$E_{pol}(1S)$ for atomic deuterium differs by 14.7%.

Our results for the response functions $S^{(0,1)}(\omega, q)$ for both studied cases are in qualitative agreement with the results shown in [23]. Even though, the average percentage difference from the results obtained for the polarizability corrections was about 16%, this study demonstrates the effectiveness of χEFT frameworks in producing high-precision theoretical predictions for hyperfine splitting observables. Moreover, it highlights the deuteron as a valuable system for investigating hyperfine shifts in both atomic and muonic deuterium, providing a robust platform for future studies in this area.

Table 4.1: The table presents results for polarizability contributions to TPE for atomic ^2H and muonic-deuterium μ^2H in $1S$ and $2S$ states. Results in the table used the approach of partial wave decomposition and are listed for each respective partial wave up to $L \leq 3$. The labels $E_{pol}^{(0,1)}$ and E_{pol} represent computations done using Eq. (4.10) and Eq. (4.15) respectively.

Hyperfine Energy Shift for Atomic (^2H) $E_{pol}^{(0,1)}$(kHz)											
State: 1S	$^3S_1$	$^3P_0$	$^3P_1$	$^3P_2$	$^3D_1$	$^3D_2$	$^3D_3$	$^3F_2$	$^3F_3$	$^3F_4$	Total
$E_{pol}^{(0)}$	3.7098	9.6680	29.4973	70.9334	2.3426	1.1185	2.9234	3.4970	3.0066	6.8028	133.4993
$E_{pol}^{(1)}$	-0.1428	-0.8164	-1.9651	-3.2366	-0.1805	-0.0452	-0.1688	-0.3000	-0.2298	-0.5136	-7.5990
E_{pol}	3.5670	8.8516	27.5322	67.6968	2.1621	1.0732	2.7545	3.1970	2.7768	6.2891	125.9004
State: 2S	$^3S_1$	$^3P_0$	$^3P_1$	$^3P_2$	$^3D_1$	$^3D_2$	$^3D_3$	$^3F_2$	$^3F_3$	$^3F_4$	Total
$E_{pol}^{(0)}$	0.4637	1.2085	3.6872	8.8667	0.2928	0.1398	0.3654	0.4371	0.3758	0.8503	16.6874
$E_{pol}^{(1)}$	-0.0179	-0.1021	-0.2456	-0.4046	-0.0226	-0.0057	-0.0211	-0.0375	-0.0287	-0.0642	-0.9499
E_{pol}	0.4459	1.1064	3.4415	8.4621	0.2703	0.1342	0.3443	0.3996	0.3471	0.7861	15.7375
Hyperfine Energy Shift for Muonic-Deuterium (μ^2H) $E_{pol}^{(0,1)}$(meV)											
State: 1S	$^3S_1$	$^3P_0$	$^3P_1$	$^3P_2$	$^3D_1$	$^3D_2$	$^3D_3$	$^3F_2$	$^3F_3$	$^3F_4$	Total
$E_{pol}^{(0)}$	0.1099	0.2300	0.7484	1.8077	0.0643	0.0343	0.0866	0.1095	0.0916	0.2067	3.4890
$E_{pol}^{(1)}$	-0.0042	-0.0110	-0.0325	-0.0568	-0.0042	-0.0018	-0.0047	-0.0095	-0.0069	-0.0152	-0.1466
E_{pol}	0.1057	0.2190	0.7160	1.7509	0.0601	0.0325	0.0819	0.1001	0.0847	0.1915	3.3424
State: 2S	$^3S_1$	$^3P_0$	$^3P_1$	$^3P_2$	$^3D_1$	$^3D_2$	$^3D_3$	$^3F_2$	$^3F_3$	$^3F_4$	Total
$E_{pol}^{(0)}$	0.0137	0.0287	0.0936	0.2260	0.0080	0.0043	0.0108	0.0137	0.0115	0.0258	0.4361
$E_{pol}^{(1)}$	-0.0005	-0.0014	-0.0041	-0.0071	-0.0005	-0.0002	-0.0006	-0.0012	-0.0009	-0.0019	-0.0183
E_{pol}	0.0132	0.0274	0.0895	0.2189	0.0075	0.0041	0.0102	0.0125	0.0106	0.0239	0.4178

Table 4.2: Summary results for polarizability contributions to TPE using 1-body vector current operators. Values for ^2H are given in kHz, and values for μ^2H are given in meV. Results were calculated up to a partial wave of $L = 3$. Polarizability contributions $E_{pol}^{0,1}$ with subscript $Idaho$ are calculated using $NNNLO_{Idaho}$ interaction.

Hyperfine Energy Shift E_{pol}				
	$^2H(1S)$	$^2H(2S)$	$\mu^2H(1S)$	$\mu^2H(2S)$
$E_{pol,Idaho}^{(0)}$	133.4993	16.6874	3.4890	0.4361
$E_{pol,Idaho}^{(1)}$	-7.5990	-0.9499	-0.1466	-0.0183
$E_{pol,Idaho}$	125.9004	15.7375	3.3424	0.4178
Theoretical: Chen Ji *et al.* [23]	109.8(3.8)	-	2.86(10)	0.358(13)

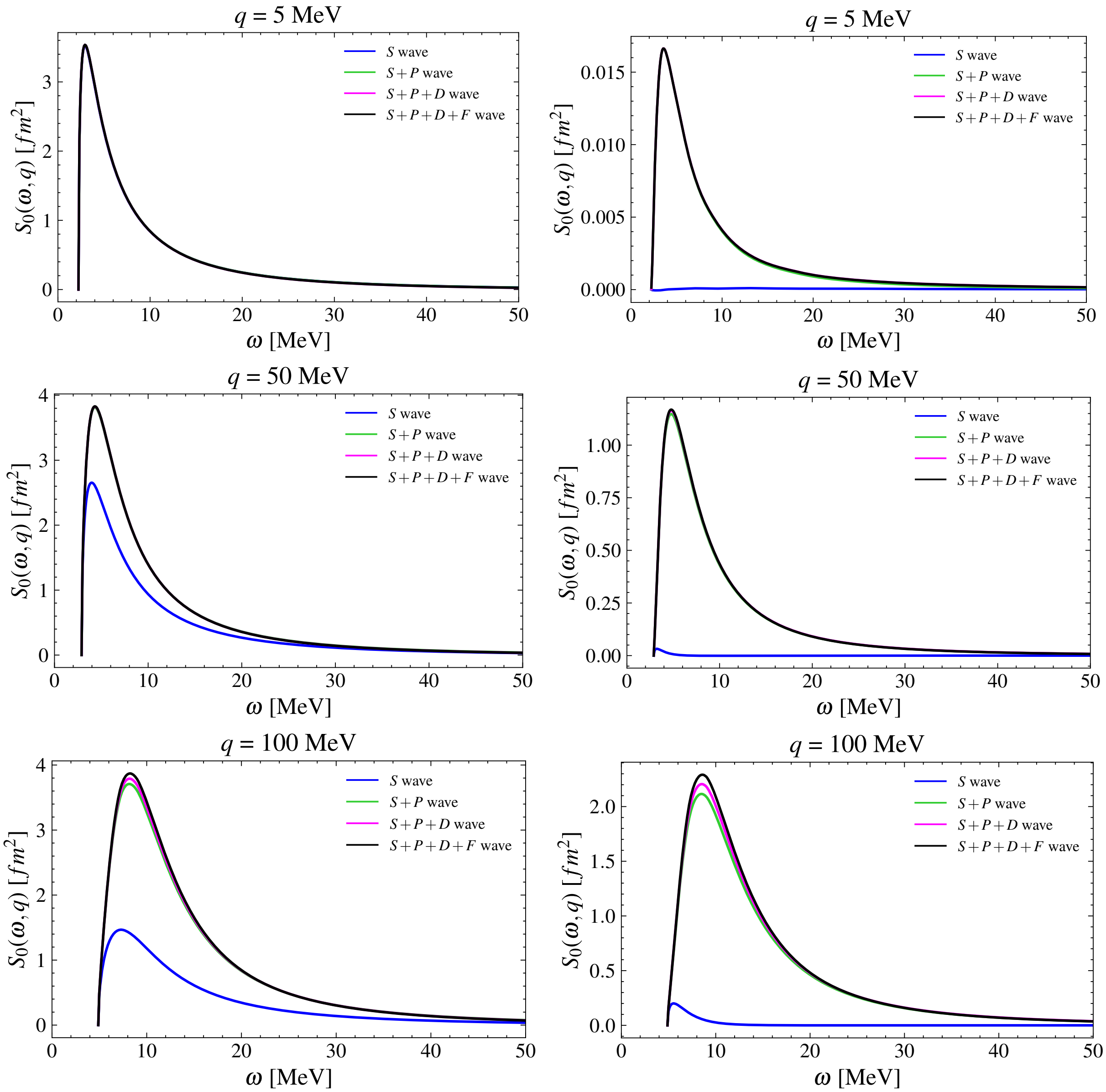

Figure 4.1: Results for the $S^{(0)}(\omega, q)$ response function computed in the absence of final state interactions (left column figures) and with final state interactions (right column figures). These results were evaluated at three fixed momentum q plotted as a function of ω and obtained using Idaho interaction with 1-body vector current operators only and point-like form factors. Line colors represent response function contributions with channel inclusions up to $L = 3$.

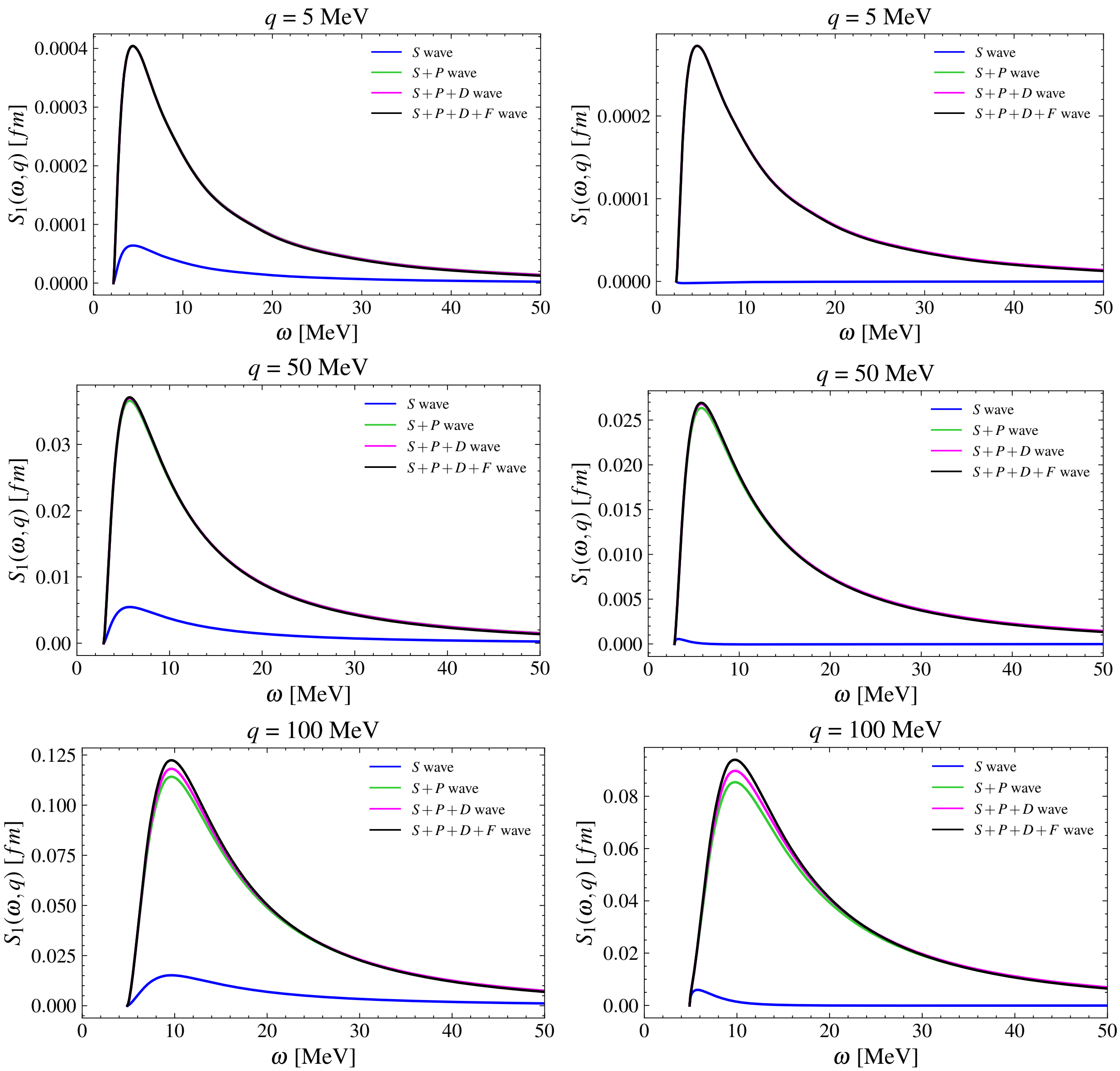

Figure 4.2: Results for the $S^{(1)}(\omega, q)$ response function computed in the absence of final state interactions (left column figures) and with final state interactions (right column figures). These results were evaluated at three fixed momentum q plotted as a function of ω and obtained using Idaho interaction with 1-body vector current operators only and point-like form factors. Line colors represent response function contributions with channel inclusions up to $L = 3$.

Bibliography

[1] B. Acharya, A. Ekström, and L. Platter. Effective-field-theory predictions of the muon-deuteron capture rate. *Phys. Rev. C*, 98:065506, Dec 2018. 34, 36

[2] S. Ando, T. S. Park, K. Kubodera, and F. Myhrer. The mu- d capture rate in effective field theory. *Phys. Lett.*, B533:25–36, 2002. 35, 37, 40

[3] A. Antognini et al. Proton Structure from the Measurement of $2S - 2P$ Transition Frequencies of Muonic Hydrogen. *Science*, 339:417–420, 2013. 45

[4] A. Baroni, L. Girlanda, S. Pastore, R. Schiavilla, and M. Viviani. Nuclear Axial Currents in Chiral Effective Field Theory. *Phys. Rev.*, C93(1):015501, 2016. [Erratum: Phys. Rev.C95, 059901(2017)]. 11

[5] A. Bertin, A. Vitale, A. Placci, and E. Zavattini. Muon capture in gaseous deuterium. *Phys. Rev. D*, 8:3774–3793, 1973. 35, 37, 40

[6] J. Bonilla, B. Acharya, and L. Platter. Muon capture on the deuteron in chiral effective field theory. *Phys. Rev. C*, 107:065502, Jun 2023. 29

[7] M. Cargnelli, W. H. Breunlich, H. Fuhrmann, P. Kammel, J. Marton, P. Pawlek, J. Werner, J. Zmeskal, W. Bertl, and C. Petitjean. Measurement of the muon capture rate in gaseous deuterium. In *23rd Yamada Conference: Nuclear Weak Processes and Nuclear Structure*, pages 115–120, 6 1989. 35, 37, 40

[8] B. D. Carlsson, A. Ekström, C. Forssén, D. F. Strömberg, G. R. Jansen, O. Lilja, M. Lindby, B. A. Mattsson, and K. A. Wendt. Uncertainty analysis and order-by-order

optimization of chiral nuclear interactions. *Phys. Rev.*, X6(1):011019, 2016. 15, 33, 39, 44

[9] L. Ceccarelli, A. Gnech, L. E. Marcucci, M. Piarulli, and M. Viviani. Muon capture on deuteron using local chiral potentials. *Front. Phys.*, 10:1049919, 2023. 37

[10] T. C. Collaboration, K. Schuhmann, L. M. P. Fernandes, F. Nez, M. A. Ahmed, F. D. Amaro, P. Amaro, F. Biraben, T.-L. Chen, D. S. Covita, A. J. Dax, M. Diepold, B. Franke, S. Galtier, A. L. Gouvea, J. Götzfried, T. Graf, T. W. Hänsch, M. Hildebrandt, P. Indelicato, L. Julien, K. Kirch, A. Knecht, F. Kottmann, J. J. Krauth, Y.-W. Liu, J. Machado, C. M. B. Monteiro, F. Mulhauser, B. Naar, T. Nebel, J. M. F. dos Santos, J. P. Santos, C. I. Szabo, D. Taqqu, J. F. C. A. Veloso, A. Voss, B. Weichelt, A. Antognini, and R. Pohl. The helion charge radius from laser spectroscopy of muonic helium-3 ions. 2023. 45

[11] A. Elmeshneb. *Muon capture on the deuteron and 3He*. PhD thesis, Jagiellonian U. (main), 2015. 34, 35, 37, 39, 40, 41

[12] D. R. Entem and R. Machleidt. Accurate charge-dependent nucleon-nucleon potential at fourth order of chiral perturbation theory. *Phys. Rev. C*, 68:041001, Oct 2003. 55

[13] E. Epelbaum, A. Gasparyan, J. Gegelia, and H. Krebs. 11 nuclear forces for precision nuclear physics: Some thoughts on the sta-tus, controversies and challenges. *Nuclear Forces for Precision Nuclear Physics–a collection of perspectives–*, page 47, 2022. 34

[14] E. Epelbaum, H. W. Hammer, and U.-G. Meissner. Modern Theory of Nuclear Forces. *Rev. Mod. Phys.*, 81:1773–1825, 2009. 5, 11

[15] R. J. Furnstahl, N. Klco, D. R. Phillips, and S. Wesolowski. Quantifying truncation errors in effective field theory. *Phys. Rev. C*, 92:024005, Aug 2015. 36

[16] A. Gnech, L. E. Marcucci, and M. Viviani. Bayesian analysis of muon capture on the deuteron in chiral effective field theory. *Phys. Rev. C*, 109:035502, Mar 2024. 38, 40, 41

[17] M. Gorchtein. γW Box Inside Out: Nuclear Polarizabilities Distort the Beta Decay Spectrum. *Phys. Rev. Lett.*, 123(4):042503, 2019. 38

[18] H. Guan, S. Chen, X.-Q. Qi, S. Liang, W. Sun, P. Zhou, Y. Huang, P.-P. Zhang, Z.-X. Zhong, Z.-C. Yan, G. W. F. Drake, T.-Y. Shi, and K. Gao. Probing atomic and nuclear properties with precision spectroscopy of fine and hyperfine structures in the ^{7}li$^+$ ion. *Phys. Rev. A*, 102:030801, Sep 2020. 45

[19] H. Hellwig, R. F. C. Vessot, M. W. Levine, P. W. Zitzewitz, D. W. Allan, and D. J. Glaze. Measurement of the unperturbed hydrogen hyperfine transition frequency. *IEEE Transactions on Instrumentation and Measurement*, 19(4):200–209, 1970. 45

[20] R. J. Hill, P. Kammel, W. J. Marciano, and A. Sirlin. Nucleon Axial Radius and Muonic Hydrogen — A New Analysis and Review. *Rept. Prog. Phys.*, 81(9):096301, 2018. 35, 37

[21] M. Hoferichter, J. Ruiz de Elvira, B. Kubis, and U.-G. Meißner. Roy–Steiner-equation analysis of pion–nucleon scattering. *Phys. Rept.*, 625:1–88, 2016. 34

[22] M. I. Eides, H. Grotch, and V. A. Shelyuto. Theory of light hydrogenlike atoms. *Physics Reports*, 342(2–3):63–261, Feb. 2001. 45

[23] C. Ji, X. Zhang, and L. Platter. Nuclear structure effects on hyperfine splittings in ordinary and muonic deuterium. 2023. 45, 47, 56, 58

[24] S. Kolling, E. Epelbaum, H. Krebs, and U. G. Meissner. Two-nucleon electromagnetic current in chiral effective field theory: One-pion exchange and short-range contributions. *Phys. Rev. C*, 84:054008, 2011. 12, 17, 38

[25] H. Krebs, E. Epelbaum, and U. G. Meißner. Nuclear axial current operators to fourth order in chiral effective field theory. *Annals Phys.*, 378:317–395, 2017. 11, 12, 13, 15, 17, 22, 38, 55

[26] R. Machleidt and D. R. Entem. Chiral effective field theory and nuclear forces. *Phys. Rept.*, 503:1–75, 2011. 34

[27] L. E. Marcucci, A. Kievsky, S. Rosati, R. Schiavilla, and M. Viviani. Chiral effective field theory predictions for muon capture on deuteron and ^3He. *Phys. Rev. Lett.*, 108:052502, 2012. 37, 38, 40

[28] L. E. Marcucci, M. Piarulli, M. Viviani, L. Girlanda, A. Kievsky, S. Rosati, and R. Schiavilla. Muon capture on deuteron and ^3He. *Phys. Rev.*, C83:014002, 2011. 16, 32, 35, 37

[29] J. Martino. A Measurement of the Muon Capture Rate in Liquid Deuterium by the Lifetime Technique. *Nucl. Phys. A*, 453:591–604, 1986. 35, 37, 40

[30] K. Pachucki. Theory of the lamb shift in muonic hydrogen. *Phys. Rev. A*, 53:2092–2100, Apr 1996. 46

[31] T. S. Park et al. Parameter-free effective field theory calculation for the solar proton fusion and hep processes. *Phys. Rev.*, C67:055206, 2003. 12

[32] T.-S. Park, K. Kubodera, D.-P. Min, and M. Rho. The Solar proton burning process revisited in chiral perturbation theory. *Astrophys. J.*, 507:443–453, 1998. 12

[33] T.-S. Park, D.-P. Min, and M. Rho. Chiral Lagrangian approach to exchange vector currents in nuclei. *Nucl. Phys.*, A596:515–552, 1996. 12

[34] R. N. Pérez, J. E. Amaro, and E. R. Arriola. Coarse-grained potential analysis of neutron-proton and proton-proton scattering below the pion production threshold. *Phys. Rev. C*, 88:064002, Dec 2013. 34

[35] R. N. Pérez, J. E. Amaro, and E. R. Arriola. Low-energy chiral two-pion exchange potential with statistical uncertainties. *Phys. Rev. C*, 91:054002, May 2015. 34

[36] R. N. Pérez, J. E. Amaro, and E. Ruiz Arriola. Precise determination of charge-dependent pion-nucleon-nucleon coupling constants. *Phys. Rev. C*, 95:064001, Jun 2017. 34

[37] R. Pohl, A. Antognini, F. Nez, F. D. Amaro, F. Biraben, J. M. R. Cardoso, D. S. Covita, A. Dax, S. Dhawan, L. M. P. Fernandes, A. Giesen, T. Graf, T. W. Hänsch, P. Indelicato, L. Julien, C. Y. Kao, P. Knowles, F. Kottmann, E. O. L. Bigot, Y. W. Liu, J. A. M. Lopes, L. Ludhova, C. M. B. Monteiro, F. Mulhauser, T. Nebel, P. Rabinowitz, J. M. F. dos Santos, K. Schuhmann, C. Schwob, D. Taqqu, J. F. C. A. Veloso, and B. Kloopfer. The size of the proton. *Nature*, 466:213–216, 2010. 46

[38] R. Pohl et al. Laser spectroscopy of muonic deuterium. *Science*, 353(6300):669–673, 2016. 45

[39] S. D. Rosner and F. M. Pipkin. Hyperfine structure of the 2^3s_1 state of he^3. *Phys. Rev. A*, 1:571–586, Mar 1970. 45

[40] G. Shen, L. E. Marcucci, J. Carlson, S. Gandolfi, and R. Schiavilla. Inclusive neutrino scattering off the deuteron from threshold to gev energies. *Phys. Rev. C*, 86:035503, Sep 2012. 16

[41] D. Siemens, J. R. de Elvira, E. Epelbaum, M. Hoferichter, H. Krebs, B. Kubis, and U. G. Meissner. Reconciling threshold and subthreshold expansions for pion–nucleon scattering. *Physics Letters B*, 770:27–34, July 2017. 34

[42] Y.-H. Song, R. Lazauskas, and T.-S. Park. Up-to N3LO heavy-baryon chiral perturbation theory calculation for the M1 properties of three-nucleon systems. *Phys. Rev.*, C79:064002, 2009. 12

[43] I.-T. Wang, E. W. Anderson, E. J. Bleser, L. M. Lederman, S. L. Meyer, J. L. Rosen, and J. E. Rothberg. Muon Capture in (pmud) + Molecules. *Phys. Rev.*, 139:B1528–B1538, 1965. 35, 37, 40

[44] S. Wesolowski, I. Svensson, A. Ekström, C. Forssén, R. J. Furnstahl, J. A. Melendez, and D. R. Phillips. Rigorous constraints on three-nucleon forces in chiral effective field theory from fast and accurate calculations of few-body observables. *Phys. Rev. C*, 104:064001, Dec 2021. 34

[45] D. J. Wineland and N. F. Ramsey. Atomic deuterium maser. *Phys. Rev. A*, 5:821–837, Feb 1972. 45

[46] R. L. Workman and Others. Review of Particle Physics. *PTEP*, 2022:083C01, 2022. 15

Appendices

Appendix A

Matrix Elements

A.1 Current Operator With Final State Interactions

To generate the nuclear matrix element, we have to include the final state interactions of the two outgoing nucleons by introducing the solution of the Lippmann-Schwinger equation which is obtained using a given nucleon-nucleon interaction, so we start by writing the nuclear matrix element as follows:

$$\begin{aligned}\langle p\alpha M_J|\,(1+\hat{t}G_0)\hat{J}^\mu\,|\psi_d, M_d\rangle &= \langle p\alpha M_J|\left[1+\hat{t}(E_{nn})G_0(E_{nn})\right]\hat{J}^\mu\,|\psi_d, M_d\rangle \\ &= \langle p\alpha M_J|\,\hat{J}^\mu\,|\psi_d, M_d\rangle + \langle p\alpha M_J|\,\hat{t}(E_{nn})G_0(E_{nn})\hat{J}^\mu\,|\psi_d, M_d\rangle\ ,\end{aligned} \tag{A.1}$$

where the state $|p\alpha M_J\rangle = |p(ls); J, M_J; T, M_T\rangle$ is a partially-wave-decomposed basis or in other words a plane wave. We can define the expression $\langle p\alpha M_J|\,(1+\hat{t}G_0)$ as $\langle nn^{FSI}|$ for simplicity, where the superscript FSI stands for final state interaction, so now we have:

$$
\begin{aligned}
\langle nn^{FSI}|\,\hat{J}^{\mu}\,|\psi_d, M_d\rangle &= \langle p\alpha M_J|\,\hat{J}^{\mu}\,|\psi_d, M_d\rangle \\
&\quad + \sum_{\alpha', M'_J}\int dp'\; p'^2 G_0 \,\langle p\alpha M_J|\,\hat{t}\,|p'\alpha' M'_J\rangle\,\langle p'\alpha' M'_J|\,\hat{J}^{\mu}\,|\psi_d, M_d\rangle \\
&= \langle p\alpha M_J|\,\hat{J}^{\mu}\,|\psi_d, M_d\rangle \\
&\quad + m\sum_{\alpha', M'_J}\int dp'\; p'^2 \frac{\langle p\alpha M_J|\,\hat{t}\,|p'\alpha' M'_J\rangle\,\langle p'\alpha' M'_J|\,\hat{J}^{\mu}\,|\psi_d, M_d\rangle}{p^2 - p'^2 + i\epsilon}\;.
\end{aligned}
$$

In the above equation $i\epsilon$ is introduced in order to avoid the singularity present in the denominator of the integral term. To eliminate the $i\epsilon$, we can use the identity

$$
\int_x dx \frac{f(x)}{g(x)+i\epsilon} = \mathcal{P}\int_x dx \frac{f(x)}{g(x)} - i\pi \int_x dx f(x)\delta[g(x)]\;, \tag{A.2}
$$

where $\mathcal{P}$ denotes principal value of the integral above, and the delta function can be solved with

$$
\delta[g(x)] = \sum_{\{x_0|g(x_0)=0\}} \frac{\delta(x-x_0)}{g'(x_0)}\;. \tag{A.3}
$$

Now using the above identities the matrix element with final state interaction becomes

$$
\begin{aligned}
\langle nn^{FSI}|\,\hat{J}^{\mu}\,|\psi_d, M_d\rangle &= \langle p\alpha M_J|\,\hat{J}^{\mu}\,|\psi_d, M_d\rangle \\
&\quad + m\sum_{\alpha', M'_J}\int dp'\; p'^2 \frac{\langle p\alpha M_J|\,\hat{t}\,|p'\alpha' M'_J\rangle\,\langle p'\alpha' M'_J|\,\hat{J}^{\mu}\,|\psi_d, M_d\rangle}{p^2 - p'^2 + i\epsilon} \\
&= \langle p\alpha M_J|\,\hat{J}^{\mu}\,|\psi_d, M_d\rangle \\
&\quad + m\sum_{\alpha', M'_J}\Bigg[\mathcal{P}\int dp'\; p'^2 \frac{\langle p\alpha M_J|\,\hat{t}\,|p'\alpha' M'_J\rangle\,\langle p'\alpha' M'_J|\,\hat{J}^{\mu}\,|\psi_d, M_d\rangle}{p^2 - p'^2} \\
&\quad - \; i\pi m\int dp'\; p'^2 \,\langle p\alpha M_J|\,\hat{t}\,|p'\alpha' M'_J\rangle\,\langle p'\alpha' M'_J|\,\hat{J}^{\mu}\,|\psi_d, M_d\rangle\,\delta(p-p')\Bigg]\;.
\end{aligned}
$$

Because of the delta function present on the second integral, which we will call I_2, we can obtain an expression rapidly as follows

$$\begin{aligned} I_2 &= i\pi m \int dp'\ p'^2 \langle p\alpha M_J|\, \hat{t}\, |p'\alpha' M'_J\rangle \langle p'\alpha' M'_J|\, \hat{J}^\mu\, |\psi_d, M_d\rangle\, \delta(p-p') \\ &= i\pi m p^2 \langle p\alpha M_J|\, \hat{t}\, |p\alpha' M'_J\rangle \langle p\alpha' M'_J|\, \hat{J}^\mu\, |\psi_d, M_d\rangle \frac{1}{2p} \\ &= i\pi \frac{mp}{2} \langle p\alpha M_J|\, \hat{t}\, |p\alpha' M'_J\rangle \langle p\alpha' M'_J|\, \hat{J}^\mu\, |\psi_d, M_d\rangle \ . \end{aligned} \tag{A.4}$$

The principal value integral, which we will call I_1, is solved by doing the following

$$I_1 = m\mathcal{P} \int dp'\ p'^2 \frac{\langle p\alpha M_J|\, \hat{t}\, |p'\alpha' M'_J\rangle \langle p'\alpha' M'_J|\, \hat{J}^\mu\, |\psi_d, M_d\rangle}{p^2 - p'^2} \ . \tag{A.5}$$

Integral I_1 is handled by adding and subtracting $p^2 \langle p\alpha M_J|\, \hat{t}\, |p\alpha' M'_J\rangle \langle p\alpha' M'_J|\, \hat{J}^\mu\, |\psi_d, M_d\rangle$ by being evaluated where the singularity occurs

$$\begin{aligned} I_1 =& m \int dp'\ p'^2 \frac{\langle p\alpha M_J|\, \hat{t}\, |p'\alpha' M'_J\rangle \langle p'\alpha' M'_J|\, \hat{J}^\mu\, |\psi_d, M_d\rangle}{p^2 - p'^2} \\ &-\ m \int dp'\ p^2 \frac{\langle p\alpha M_J|\, \hat{t}\, |p\alpha' M'_J\rangle \langle p\alpha' M'_J|\, \hat{J}^\mu\, |\psi_d, M_d\rangle}{p^2 - p'^2} \\ &+\ mp^2 \langle p\alpha M_J|\, \hat{t}\, |p\alpha' M'_J\rangle \langle p\alpha' M'_J|\, \hat{J}^\mu\, |\psi_d, M_d\rangle\, \mathcal{P} \int \frac{dp'}{p-p'} \ . \end{aligned} \tag{A.6}$$

Now solving the remaining principal value integral we get

$$\begin{aligned} I_3 &= \mathcal{P} \int_0^\Lambda \frac{dp'}{p-p'} = \frac{1}{2p} \mathcal{P} \int_0^\Lambda dp' \left(\frac{1}{p-p'} + \frac{1}{p+p'} \right) \\ &= \frac{1}{2p} \left\{ \mathcal{P} \int_0^{2p} \frac{dp'}{p-p'} + \int_{2p}^{\Lambda} \frac{dp'}{p-p'} + \left[log(p+p') \right]_{p'=0}^{p'=\Lambda} \right\} \ . \end{aligned} \tag{A.7}$$

Noting that the principal value integral goes to zero, then we can solve I_3 as follows

$$
\begin{aligned}
I_3 &= \frac{1}{2p}\Bigg\{\big[-log(|p-p'|)\big]_{p'=2p}^{p'=\Lambda} + log(p+\Lambda) - log(p)\Bigg\} \\
&= \frac{1}{2p} log\left(\frac{\Lambda+p}{\Lambda-p}\right) .
\end{aligned} \tag{A.8}
$$

Finally putting everything together we get:

$$
\begin{aligned}
\langle nn^{FSI}|\, \hat{J}^{\mu}\, |\psi_d, M_d\rangle = \langle p\alpha M_J|\, \hat{J}^{\mu}\, |\psi_d, M_d\rangle & \\
+ \sum_{\alpha', M_J'} \Bigg[m \int_0^{\Lambda} dp'\ p'^2 \frac{\langle p\alpha M_J|\, \hat{t}\, |p'\alpha' M_J'\rangle \langle p'\alpha' M_J'|\, \hat{J}^{\mu}\, |\psi_d, M_d\rangle}{p^2 - p'^2} & \\
- \ m \int_0^{\Lambda} dp'\ p^2 \frac{\langle p\alpha M_J|\, \hat{t}\, |p\alpha' M_J'\rangle \langle p\alpha' M_J'|\, \hat{J}^{\mu}\, |\psi_d, M_d\rangle}{p^2 - p'^2} & \\
+ \ \frac{mp}{2} \langle p\alpha M_J|\, \hat{t}\, |p\alpha' M_J'\rangle \langle p\alpha' M_J'|\, \hat{J}^{\mu}\, |\psi_d, M_d\rangle\, log\left(\frac{\Lambda+p}{\Lambda-p}\right) & \\
- \ i\pi \frac{mp}{2} \langle p\alpha M_J|\, \hat{t}\, |p\alpha' M_J'\rangle \langle p\alpha' M_J'|\, \hat{J}^{\mu}\, |\psi_d, M_d\rangle \Bigg] &
\end{aligned} \tag{A.9}
$$

and simplifying we finally obtain

$$
\begin{aligned}
\langle nn^{FSI}|\, \hat{J}^{\mu}\, |\psi_d, M_d\rangle = \langle p\alpha M_J|\, \hat{J}^{\mu}\, |\psi_d, M_d\rangle & \\
+ \sum_{\alpha', M_J'} \Bigg\{ m \int_0^{\Lambda} dp'\ p'^2 \frac{\langle p\alpha M_J|\, \hat{t}\, |p'\alpha' M_J'\rangle \langle p'\alpha' M_J'|\, \hat{J}^{\mu}\, |\psi_d, M_d\rangle}{p^2 - p'^2} & \\
- \ m \int_0^{\Lambda} dp'\ p^2 \frac{\langle p\alpha M_J|\, \hat{t}\, |p\alpha' M_J'\rangle \langle p\alpha' M_J'|\, \hat{J}^{\mu}\, |\psi_d, M_d\rangle}{p^2 - p'^2} & \\
+ \ \frac{mp}{2} \langle p\alpha M_J|\, \hat{t}\, |p\alpha' M_J'\rangle \langle p\alpha' M_J'|\, \hat{J}^{\mu}\, |\psi_d, M_d\rangle \left[log\left(\frac{\Lambda+p}{\Lambda-p}\right) - i\pi \right] \Bigg\} . &
\end{aligned} \tag{A.10}
$$

where the relative energy of the two-nucleon system is defined as $E_{nn} = p^2/m$, and m is the nucleon mass.

A.2 Spin and Isospin Operation

For the case of the muon capture calculation, we encounter the single nucleon lowering operator which is defined as

$$\tau_{i,-} = \frac{1}{2}\big(\tau_{i,x} - i\tau_{i,y}\big) \ , \tag{A.11}$$

where, i refers to whether we operate on particle 1 or particle 2. Its relevant matrix elements can be calculated easily for the case of an incoming spin-singlet state of the two nucleons $|0,0\rangle$ and outgoing spin-triplet state $|1,-1\rangle$. The solutions for this particular case is then

$$\langle 1,-1|\,\tau_{-,1}\,|0,0\rangle = \frac{1}{\sqrt{2}} \ , \qquad \langle 1,-1|\,\tau_{-,2}\,|0,0\rangle = \frac{-1}{\sqrt{2}} \ . \tag{A.12}$$

Now, the lowering component of the cross product of the isospin matrices found in the 2-body current operators can be defined as shown below

$$(\boldsymbol{\tau}_1 \times \boldsymbol{\tau}_2)_- = i\sqrt{2}\big({\tau_{-1}}^{(1)}{\tau_0}^{(2)} - {\tau_0}^{(1)}{\tau_{-1}}^{(2)}\big) \ . \tag{A.13}$$

To operate between an initial and final isospin states using Eq.(A.13) such as

$$\langle T', M_T'|\,(\boldsymbol{\tau}_1 \times \boldsymbol{\tau}_2)_-\,|T, M_T\rangle = i\sqrt{2}\,\langle T', M_T'|\,\big({\tau_{-1}}^{(1)}{\tau_0}^{(2)} - {\tau_0}^{(1)}{\tau_{-1}}^{(2)}\big)\,|T, M_T\rangle \ \ , \tag{A.14}$$

and then inserting a complete set of 2-body isospin states gives

$$\langle T', M_T'|\,{\tau_{-1}}^{(1)}{\tau_0}^{(2)}\,|T, M_T\rangle = \sum_{T'',M_T"} \langle T', M_T'|\,{\tau_{-1}}^{(1)}\,|T", M_T"\rangle\,\langle T", M_T"|\,{\tau_0}^{(2)}\,|T, M_T\rangle \ \ , \tag{A.15}$$

$$\langle T', M_T'|\,{\tau_0}^{(1)}{\tau_{-1}}^{(2)}\,|T, M_T\rangle = \sum_{T'',M_T"} \langle T', M_T'|\,{\tau_0}^{(1)}\,|T", M_T"\rangle\,\langle T", M_T"|\,{\tau_{-1}}^{(2)}\,|T, M_T\rangle \ \ . \tag{A.16}$$

We can solve the coefficients of $\langle T', M_T'|\,\tau_\mu^{(i)}\,|T, M_T\rangle$ by using the Wigner-Eckart theorem as:

$$\langle T', M_T'|\,\tau_\mu^{(i)}\,|T, M_T\rangle = C^{T',M_T'}_{T,M_T;1,\mu}\langle T'||\tau_{(i)}||T\rangle \ . \tag{A.17}$$

Putting everything together we get:

$$\langle T', M_T'| \left(\boldsymbol{\tau}_1 \times \boldsymbol{\tau}_2\right)_- |T, M_T\rangle = i\sqrt{2} \sum_{T", M_T"} \left[C^{T', M_T'}_{T", M_T"; 1, -1} C^{T", M_T"}_{T, M_T; 1, 0} - C^{T', M_T'}_{T", M_T"; 1, 0} C^{T", M_T"}_{T, M_T; 1, -1} \right] \times \langle T' || \tau_1 || T" \rangle \langle T" || \tau_2 || T \rangle \ . \quad \text{(A.18)}$$

For the μd-capture case, we use $|0,0\rangle$ and $|1,-1\rangle$ for our initial and final state respectively. So for the two isospin cross product combination operation we have:

$$\langle 1, -1| \left(\boldsymbol{\tau}_1 \times \boldsymbol{\tau}_2\right)_- |0, 0\rangle = -i2\sqrt{2} \ , \qquad \langle 1, -1| \left(\boldsymbol{\tau}_2 \times \boldsymbol{\tau}_1\right)_- |0, 0\rangle = i2\sqrt{2} \ . \quad \text{(A.19)}$$

The same prescription can be applied to solve the coefficients of $\langle S, M_S| \, \sigma_{i,\mu} \, |S_d, M_{s_d}\rangle$, which involves the Pauli spin matrices and are found in different of the 1- and 2-body current operators; this is done as follows

$$\langle S, M_S| \, \sigma_{i,\mu} \, |S_d, M_{s_d}\rangle = C^{S, M_S}_{S_d, M_{S_d}; 1, \mu} \langle S || \sigma_i || S_d \rangle \ . \quad \text{(A.20)}$$

For the case of double spin matrices operation we have:

$$\langle S, M_S| \, \sigma_{i,\mu} \sigma_{j,\nu} \, |S_d, M_{s_d}\rangle = \sum_{S', M'} C^{S, M_S}_{S', M_S'; 1, \mu} C^{S', M_S'}_{S_d, M_d; 1, \nu} \langle S || \sigma_i || S' \rangle \langle S' || \sigma_j || S_d \rangle \ . \quad \text{(A.21)}$$

The corresponding reduced matrix coefficients for the particular combination case of $S = 0, 1$ and $S_d = 0, 1$ are found to be

for particle (1):

$$\langle 0 || \sigma_1 || 1 \rangle = -\sqrt{3} \ , \quad \langle 1 || \sigma_1 || 1 \rangle = \sqrt{2} \ , \quad \langle 1 || \sigma_1 || 0 \rangle = 1 \ , \quad \text{(A.22)}$$

for particle (2):

$$\langle 0 || \sigma_2 || 1 \rangle = \sqrt{3} \ , \quad \langle 1 || \sigma_2 || 1 \rangle = \sqrt{2} \ , \quad \langle 1 || \sigma_2 || 0 \rangle = -1 \ . \quad \text{(A.23)}$$

A.3 Leptonic matrix element

In this section, we will calculate the leptonic matrix element l^σ explicitly. To do this, we work in the Pauli-Dirac representation. We need to evaluate

$$l^\sigma = \bar{u}(\nu)\gamma^\sigma(1+\gamma^5)u(k, m_\mu) \ . \tag{A.24}$$

The neutrino spinor is

$$u(\nu) = \sqrt{\nu_0}\begin{pmatrix} \chi^\nu \\ \frac{\boldsymbol{\sigma}\cdot\boldsymbol{\nu}}{E+m_\nu}\chi^\nu \end{pmatrix} \ , \tag{A.25}$$

where χ^ν is a 2-component spinor describing the neutrino spin, and ν denotes the 4-momentum of the neutrino. Setting the neutrino mass to 0 leads to

$$u(\nu) = \sqrt{\nu_0}\begin{pmatrix} \chi^\nu \\ \frac{\boldsymbol{\sigma}\cdot\boldsymbol{\nu}}{\nu_0}\chi^\nu \end{pmatrix} \ . \tag{A.26}$$

This expression simplifies further if we align the neutrino momentum with the z-axis. Since the muon is assumed to be at rest, this corresponds to fixing the direction of the mometum exchange. Then, the neutrino helicity is the neutrino spin

$$u(\nu) = \sqrt{\nu_0}\begin{pmatrix} \chi^\nu \\ \sigma^3\chi^\nu \end{pmatrix} \ . \tag{A.27}$$

Note that we also used $\nu_0 = |\boldsymbol{\nu}|$. If we now include include the fact that neutrinos are left-handed and exploit that for the neutrino 2-component spinor thus $\sigma_3\chi^\nu = -\chi^\nu$, we get

$$u(\nu) = \sqrt{\nu_0}\begin{pmatrix} \chi^\downarrow \\ -\chi^\downarrow \end{pmatrix} \ . \tag{A.28}$$

For the muon Dirac spinor, we will set the momentum $\mathbf{k}$ to 0. Below, χ^μ denotes the two-component spinor for the muon.

$$u(k, s_\mu) = \sqrt{k_0 + m_\mu} \begin{pmatrix} \chi^\mu \\ \frac{\boldsymbol{\sigma}\cdot\mathbf{k}}{k_0+m_\mu}\chi^h \end{pmatrix} \to \sqrt{2m_\mu} \begin{pmatrix} \chi^\mu \\ 0 \end{pmatrix} , \tag{A.29}$$

where we used $k_0 = m_\mu$ for $\mathbf{k} = 0$.

We can evaluate l^σ for the case of l^0, this give us

$$l^0 = \sqrt{2m_\mu\nu_0} \begin{pmatrix} \chi^\downarrow \\ -\chi^\downarrow \end{pmatrix}^\dagger \gamma^0\gamma^0(1-\gamma^5) \begin{pmatrix} \chi^\mu \\ 0 \end{pmatrix} = \sqrt{2m_\mu\nu_0} \begin{pmatrix} \chi^\downarrow \\ -\chi^\downarrow \end{pmatrix}^\dagger (1-\gamma^5) \begin{pmatrix} \chi^\mu \\ 0 \end{pmatrix} . \tag{A.30}$$

A.4 The Dirac-Pauli representation

The Dirac-Pauli representation is particularly useful when we combine relativistic expressions (such as the one for the leptonic matrix element) with non-relativistic ones. In this representation, we have for the γ-matrices

$$\gamma^0 = \begin{pmatrix} \mathbb{1} & 0 \\ 0 & -\mathbb{1} \end{pmatrix} , \boldsymbol{\gamma} = \begin{pmatrix} 0 & \boldsymbol{\sigma} \\ -\boldsymbol{\sigma} & 0 \end{pmatrix} , \tag{A.31}$$

The Dirac-Pauli representation lets us define spherical γ-matrices. We define

$$\gamma_+ = -\frac{1}{\sqrt{2}}(\gamma^1 + i\gamma^2) = \begin{pmatrix} 0 & \sigma_+ \\ -\sigma_+ & 0 \end{pmatrix} , \tag{A.32}$$

$$\gamma_- = \frac{1}{\sqrt{2}}(\gamma^1 - i\gamma^2) = \begin{pmatrix} 0 & \sigma_- \\ -\sigma_- & 0 \end{pmatrix} , \tag{A.33}$$

and

$$1 - \gamma^5 = \begin{pmatrix} \mathbb{1} & -\mathbb{1} \\ -\mathbb{1} & \mathbb{1} \end{pmatrix} . \tag{A.34}$$

We can therefore write the contraction of leptonic and hadronic current as

$$l^{\sigma} j_{\sigma} = l^{0} j_{0} - \mathbf{l} \cdot \mathbf{j} \ , \tag{A.35}$$

where in spherical bases can be expanded as:

$$\begin{aligned} l^{\sigma} j_{\sigma} &= l^{0} j_{0} - (l^{+1} j_{+1} + l^{-1} j_{-1} + l^{z} j_{z}) \\ &= l^{0} j_{0} - (-l_{-1} j_{+1} - l_{+1} j_{-1} + l_{z} j_{z}) \\ &= l^{0} j_{0} + l_{-1} j_{+1} + l_{+1} j_{-1} - l_{z} j_{z} \ , \end{aligned} \tag{A.36}$$

where the resulting leptonic matrix element are defined as:

$$l_0 = \sqrt{2}\delta_{m,1/2} \ , \tag{A.37}$$

$$l_{+1} = 2\delta_{m,-1/2} \ , \tag{A.38}$$

$$l_{-1} = 0 \ , \tag{A.39}$$

$$l_z = -\sqrt{2}\delta_{m,1/2} \ . \tag{A.40}$$

A.5 Addtion Rule for Spherical Harmonics

The General equation of the plane wave can be defined as the linear combination of spherical harmonics Y_l^{μ} and spherical Bessel functions j_l. For our particular case, which is encountered when evaluating the nuclear matrix elements, the plane wave can be defined as follows

$$e^{i(\boldsymbol{p}-\boldsymbol{q})\cdot\boldsymbol{r}} = 4\pi \sum_{l\mu} i^l j_l(|\boldsymbol{p}-\boldsymbol{q}|r) Y_l^{\mu}(\boldsymbol{p} \hat{-} \boldsymbol{q}) Y_l^{*\mu}(\hat{\boldsymbol{r}}) = e^{i\boldsymbol{p}\cdot\boldsymbol{r}} e^{-i\boldsymbol{q}\cdot\boldsymbol{r}} \ , \tag{A.41}$$

where $\boldsymbol{r}$ is the position vector, and $\boldsymbol{p}$ and $\boldsymbol{q}$ are momentum vectors. We can further expand the above expression as follows

$$\begin{aligned}
e^{i\boldsymbol{p}\cdot\boldsymbol{r}}e^{-i\boldsymbol{q}\cdot\boldsymbol{r}} &= (4\pi)^2 \sum_{LN}\sum_{LN'} i^{L'-L} j_{L'}(pr) j_L(qr) Y_{L'}^{N'}(\hat{\boldsymbol{p}}) Y_L^N(\hat{\boldsymbol{q}}) Y_{L'}^{*N'}(\hat{\boldsymbol{r}}) Y_L^{*N}(\hat{\boldsymbol{r}}) \\
&= (4\pi)^2 \sum_{LN}\sum_{L'N'}\sum_{l'\mu'} \left[\frac{(2L+1)(2L'+1)}{4\pi(2l'+1)}\right]^{1/2} C^{l',0}_{L',0;L,0} C^{l',\mu'}_{L',N';L,N} \\
&\times i^{L'-L} j_{L'}(pr) j_L(qr) Y_{L'}^{N'}(\hat{\boldsymbol{p}}) Y_L^N(\hat{\boldsymbol{q}}) Y_{l'}^{*\mu'}(\hat{\boldsymbol{r}}) \ .
\end{aligned} \tag{A.42}$$

By setting Eq. (A.41) and Eq. (A.42) equal to each other we obtain

$$\begin{aligned}
i^l \frac{|\boldsymbol{p}-\boldsymbol{q}|^l r^l}{(2l+1)!!} Y_l^\mu(\boldsymbol{p} \hat{-} \boldsymbol{q}) = 4\pi \sum_{LN}\sum_{L'N'} \left[\frac{(2L+1)(2L'+1)}{4\pi(2l+1)}\right]^{1/2} C^{l,0}_{L',0;L,0} C^{l,\mu}_{L',N';L,N} \\
\times i^{L'-L} \frac{p^{L'} q^L r^{L+L'}}{(2L+1)!!(2L'+1)!!} Y_{L'}^{N'}(\hat{\boldsymbol{p}}) Y_L^N(\hat{\boldsymbol{q}}) \ .
\end{aligned} \tag{A.43}$$

Since the triangle relations of the Clebsch-Gordan coefficients require $l \leq L + L'$, then the coefficients of r^l must be the same on both sides of the equation. So taking $L' = l - L$ we get:

$$\begin{aligned}
Y_l^\mu(\widehat{\boldsymbol{p}-\boldsymbol{q}}) = \sqrt{4\pi} \sum_{LN} (-1)^L \left[\frac{(2l+1)!}{(2L+1)!(2l-2L+1)!}\right]^{1/2} \\
\times \frac{p^{l-L}(q)^L}{|\boldsymbol{p}-\boldsymbol{q}|^l} C^{l,\mu}_{(l-L),(\mu-N);L,N} Y_{l-L}^{\mu-N}(\hat{\boldsymbol{p}}) Y_L^N(\hat{\boldsymbol{q}}) \ .
\end{aligned} \tag{A.44}$$

For $Y_l^\mu(\widehat{\boldsymbol{p}+\boldsymbol{q}})$ case, the $i^{L'-L} \to i^l$ cancel out in both sides of the equal sign. Therefore, there is no phase $(-1)^L$ in $Y_l^\mu(\widehat{\boldsymbol{p}+\boldsymbol{q}})$, and the denominator $|\boldsymbol{p}-\boldsymbol{q}|^l$ in the above equation goes like $|\boldsymbol{p}+\boldsymbol{q}|^l$.

So for our case in the μd-capture process, where we take the direction of the 3-momentum transfer $\boldsymbol{q}$ in the z-direction, we have:

$$Y_2^{m_{l_d}}(\widehat{\boldsymbol{p}-\boldsymbol{q}/2}) = \sqrt{4\pi}\sum_{LN}(-1)^L\left[\frac{5!}{(2L+1)!(5-2L)!}\right]^{1/2}\frac{p^{2-L}(q/2)^L}{|\boldsymbol{p}-\boldsymbol{q}/2|^2} \times \langle(2-L),L,2|(m_{l_d}-N),N,m_{l_d}\rangle\, Y_{2-L}^{m_{l_d}-N}(\hat{\boldsymbol{p}})Y_L^N(\hat{\boldsymbol{q}})\ , \quad \text{(A.45)}$$

$$Y_2^{m_{l_d}}(\widehat{\boldsymbol{p}+\boldsymbol{q}/2}) = \sqrt{4\pi}\sum_{LN}\left[\frac{5!}{(2L+1)!(5-2L)!}\right]^{1/2}\frac{p^{2-L}(q/2)^L}{|\boldsymbol{p}+\boldsymbol{q}/2|^2} \times \langle(2-L),L,2|(m_{l_d}-N),N,m_{l_d}\rangle\, Y_{2-L}^{m_{l_d}-N}(\hat{\boldsymbol{p}})Y_L^N(\hat{\boldsymbol{q}})\ , \quad \text{(A.46)}$$

where:

$$Y_L^N(\hat{\boldsymbol{q}}) = \sqrt{\frac{2L+1}{4\pi}}\delta_{0,N}\ . \quad \text{(A.47)}$$

A.6 Integral Reduction for Relative ϕ Angle

In this appendix section, we show how the angular integral calculation encountered in the nuclear matrix elements for the μd-capture case was reduced or simplified by integrating out the angle ϕ dependence. If the spherical harmonics are defined as:

$$Y_l^m(\theta,\phi) = \sqrt{\frac{(2l+1)}{4\pi}\frac{(l-m)!}{(l+m)!}}P_l^m(\theta)e^{im\phi} = F(l,m,\theta)e^{im\phi}\ , \quad \text{(A.48)}$$

and if we defined the Kronecker Delta function as:

$$\delta_{m,n} = \frac{1}{2\pi i}\oint_{|z|=1} z^{m-n-1}dz = \frac{1}{2\pi}\int_0^{2\pi} e^{i\phi(m-n)}d\phi \quad \text{(A.49)}$$

then for the case in which we have the integral of the product of three spherical harmonics, we can reduce it as follows:

$$\int_0^{2\pi} Y_l^{*m_l}(\theta,\phi) Y_{l'}^{m'}(\theta,\phi) Y_{l_d}^{m_{ld}}(\theta,\phi) d\phi$$
$$= \int_0^{2\pi} (-1)^{m_l} F(l,-m_l,\theta) F(l',m',\theta) F(l_d,m_{ld},\theta) e^{-im_l\phi} e^{im'\phi} e^{im_{ld}\phi} d\phi$$
$$= (-1)^{m_l} F(l,-m_l,\theta) F(l',m',\theta) F(l_d,m_{ld},\theta)\ 2\pi\ \delta_{m_l,m'+m_{ld}}\ . \quad (A.50)$$

A.7 Vector current matrix elements derivations

A.7.1 Vector Current Definitions

In the section, we derive the nuclear matrix elements for the vector current operators which contain point-like form factors and they are defined as:

$$\hat{V}_0^{(i)} = G_E = \frac{1}{2}(1+\tau_3)^{(i)} \quad (A.51)$$

$$\hat{\boldsymbol{V}_c}^{(i)} = \frac{\boldsymbol{q}_i}{m} G_E = \frac{\boldsymbol{q}_i}{m}\frac{1}{2}(1+\tau_3)^{(i)} \quad (A.52)$$

$$\hat{\boldsymbol{V}_m}^{(i)} = i\frac{1}{2m}(\boldsymbol{\sigma_i}\times\boldsymbol{q}) G_M = i\frac{1}{2m}(\boldsymbol{\sigma_i}\times\boldsymbol{q})(\kappa_0+\kappa_1\tau_3)^{(i)} \quad (A.53)$$

where $\boldsymbol{q}_i = \frac{\boldsymbol{p}_i'+\boldsymbol{p}_i}{2}$, and the neutron magnetic form factors $\kappa_p = 5.586$ and $\kappa_n = -3.826$ by $\kappa_0 = (\kappa_p+\kappa_n)/2$ and $\kappa_1 = (\kappa_p-\kappa_n)/2$.

A.7.2 Momentum Space Deuteron Wave Function

Using the same definition as in Elmeshneb's thesis:

$$|\psi_d M_d\rangle = \int dp'\ p'^2 \sum_{l_d=0,2} |p'(l_d 1); 1 M_d\rangle \otimes |0,0\rangle\ \psi_{l_d}(p') \quad (A.54)$$

Now projecting it into momentum space we get:

$$\langle \boldsymbol{p}|\psi_d M_d\rangle = \sum_{l_d,m_{ld}} Y_{l_d}^{m_{ld}}(\hat{p}) C^{1,M_d}_{l_d,m_{ld};1,M_d-m_{ld}} \otimes |1, M_d - m_{ld}\rangle \otimes |0,0\rangle\, \psi_{l_d}(p) \tag{A.55}$$

A.7.3 Plane Wave in Momentum Space

If we operate a plane wave on the left with $\langle \boldsymbol{p}|$ then we get:

$$\langle \boldsymbol{p}|p'(ls)J, M_J; T, M_T\rangle = \sum_{m_l} Y_l^{m_l}(\hat{p}) C^{J,M_J}_{l,m_l;S,M_J-m_l} \frac{\delta(|\boldsymbol{p}|-p')}{pp'} \otimes |S, M_J - m_l\rangle \otimes |T, M_T\rangle \tag{A.56}$$

A.7.4 Vector Current Matrix Elements

<u>**Time-like Vector Current Matrix Element**</u>

$$\langle p\alpha M_J; T, M_T|\, V_0\, |\psi_d, M_d\rangle = \int d^3\boldsymbol{p}' \int d^3\boldsymbol{p}''\, \langle p\alpha M_J; T, M_T|\boldsymbol{p}'\rangle\, \langle \boldsymbol{p}'|\, V_0\, |\boldsymbol{p}''\rangle\, \langle \boldsymbol{p}''|\psi_d, M_d\rangle \;\; , \tag{A.57}$$

$$\begin{aligned} \langle p\alpha M_J; T, M_T|\, V_0\, |\psi_d, M_d\rangle &= \int d^3\boldsymbol{p}' \int d^3\boldsymbol{p}'' \\ &\times \sum_{m_l} Y_l^{*m_l}(\hat{p'}) C^{J,M_J}_{l,m_l;S,M_J-m_l} \frac{\delta(|\boldsymbol{p}'|-p)}{p'p} \sum_{l_d,m_{ld}} Y_{l_d}^{m_{ld}}(\hat{p''}) C^{1,M_d}_{l_d,m_{ld};1,M_d-m_{ld}} \psi_{l_d}(p'') \\ &\times \langle T, M_T| \otimes \langle S, M_J - m_l| \otimes \langle \boldsymbol{p}'|\, V_0\, |\boldsymbol{p}''\rangle \otimes |1, M_d - m_{ld}\rangle \otimes |0,0\rangle \;\; , \end{aligned} \tag{A.58}$$

$$
\begin{aligned}
\langle p\alpha M_J;T,M_T|\,V_0\,|\psi_d,M_d\rangle &= \int d\hat{\boldsymbol{p}}\int d^3\boldsymbol{p}'' \\
&\times\sum_{m_l} Y_l^{*m_l}(\hat{p})C^{J,M_J}_{l,m_l;S,M_J-m_l}\sum_{l_d,m_{ld}} Y_{l_d}^{m_{ld}}(\hat{p''})C^{1,M_d}_{l_d,m_{ld};1,M_d-m_{ld}}\psi_{l_d}(p'') \\
&\times\langle T,M_T|\otimes\langle S,M_J-m_l|\otimes\langle\boldsymbol{p}|\,V_0\,|\boldsymbol{p}''\rangle\otimes|1,M_d-m_{ld}\rangle\otimes|0,0\rangle \quad , \qquad \text{(A.59)}
\end{aligned}
$$

$$
\begin{aligned}
\langle p\alpha M_J;T,M_T|\,V_0\,|\psi_d,M_d\rangle &= \int d\hat{\boldsymbol{p}}\int d^3\boldsymbol{p}'' \\
&\times\sum_{m_l} Y_l^{*m_l}(\hat{p})C^{J,M_J}_{l,m_l;S,M_J-m_l}\sum_{l_d,m_{ld}} Y_{l_d}^{m_{ld}}(\hat{p''})C^{1,M_d}_{l_d,m_{ld};1,M_d-m_{ld}}\psi_{l_d}(p'') \\
\times\langle T,M_T|\otimes\langle S,M_J-m_l|&\left[\frac{1}{2}(1+\tau_3)^{(i)}\delta^3(\boldsymbol{p}''-\boldsymbol{p}\pm\boldsymbol{q}/2)\right]|1,M_d-m_{ld}\rangle\otimes|0,0\rangle \quad , \qquad \text{(A.60)}
\end{aligned}
$$

$$
\begin{aligned}
\langle p\alpha M_J;T,M_T|\,V_0\,|\psi_d,M_d\rangle &= \int d\hat{\boldsymbol{p}} \\
\times\sum_{m_l} Y_l^{*m_l}(\hat{p})C^{J,M_J}_{l,m_l;S,M_J-m_l}&\sum_{l_d,m_{ld}} Y_{l_d}^{m_{ld}}(\widehat{\boldsymbol{p}\mp\boldsymbol{q}/}2)C^{1,M_d}_{l_d,m_{ld};1,M_d-m_{ld}}\psi_{l_d}(|\boldsymbol{p}\mp\boldsymbol{q}/2|) \\
&\times\delta_{S,1}\delta_{,M_J-m_l,M_d-m_{ld}}\frac{1}{2}(\delta_{T,0}\delta_{M_T,0}\pm\delta_{T,1}\delta_{M_T,0})^{(i)} \quad , \qquad \text{(A.61)}
\end{aligned}
$$

$$
\begin{aligned}
\langle p\alpha M_J;T,M_T|\,V_0\,|\psi_d,M_d\rangle &= \int d\hat{\boldsymbol{p}}\sum_{m_l} Y_l^{*m_l}(\hat{p})C^{J,M_J}_{l,m_l;S,M_J-m_l} \\
&\times\Bigg\{\delta_{S,1}\delta_{,M_J-m_l,M_d-m_{ld}}\frac{1}{2}(\delta_{T,0}\delta_{M_T,0}\pm\delta_{T,1}\delta_{M_T,0})^{(i)}\frac{1}{\sqrt{4\pi}}\psi_0(|\boldsymbol{p}\mp\boldsymbol{q}/2|)+ \\
\sum_{2,m_{ld}} Y_2^{m_{ld}}(\widehat{\boldsymbol{p}\mp\boldsymbol{q}/}2)&C^{1,M_d}_{2,m_{ld};1,M_d-m_{ld}}\delta_{S,1}\delta_{,M_J-m_l,M_d-m_{ld}}\frac{1}{2}(\delta_{T,0}\delta_{M_T,0}\pm\delta_{T,1}\delta_{M_T,0})^{(i)}\psi_2(|\boldsymbol{p}\mp\boldsymbol{q}/2|)\Bigg\}\,,
\end{aligned}
$$

(A.62)

$$\langle p\alpha M_J;T,M_T|\,V_0\,|\psi_d,M_d\rangle = \int d\hat{\boldsymbol{p}}\sum_{m_l} Y_l^{*m_l}(\hat{p})C^{J,M_J}_{l,m_l;S,M_J-m_l}$$
$$\times\,\delta_{S,1}\delta_{,M_J-m_l,M_d-m_{ld}}\frac{1}{2}(\delta_{T,0}\delta_{M_T,0}\pm\delta_{T,1}\delta_{M_T,0})^{(i)}\Bigg\{\frac{1}{\sqrt{4\pi}}\psi_0(|\boldsymbol{p}\mp\boldsymbol{q}/2|)+$$
$$\sum_{2,m_{ld}} Y_2^{m_{ld}}(\widehat{\boldsymbol{p}\mp\boldsymbol{q}/}2)C^{1,M_d}_{2,m_{ld};1,M_d-m_{ld}}\psi_2(|\boldsymbol{p}\mp\boldsymbol{q}/2|)\Bigg\}\;. \quad \text{(A.63)}$$

<u>**Convection Vector Current Matrix Element**</u>

$$\langle p\alpha M_J;T,M_T|\,\boldsymbol{V}_c\,|\psi_d,M_d\rangle = \int d^3\boldsymbol{p}'\int d^3\boldsymbol{p}''\,\langle p\alpha M_J;T,M_T|\boldsymbol{p}'\rangle\,\langle\boldsymbol{p}'|\,\boldsymbol{V}_c\,|\boldsymbol{p}''\rangle\,\langle\boldsymbol{p}''|\psi_d,M_d\rangle\;\;, \quad \text{(A.64)}$$

$$\langle p\alpha M_J;T,M_T|\,\boldsymbol{V}_c\,|\psi_d,M_d\rangle = \int d\hat{\boldsymbol{p}}\int d^3\boldsymbol{p}''$$
$$\times\sum_{m_l} Y_l^{*m_l}(\hat{p})C^{J,M_J}_{l,m_l;S,M_J-m_l}\sum_{l_d,m_{ld}} Y_{l_d}^{m_{ld}}(\hat{p''})C^{1,M_d}_{l_d,m_{ld};1,M_d-m_{ld}}\psi_{l_d}(p'')$$
$$\times\,\langle T,M_T|\otimes\langle S,M_J-m_l|\otimes\langle\boldsymbol{p}|\,\boldsymbol{V}_c\,|\boldsymbol{p}''\rangle\otimes|1,M_d-m_{ld}\rangle\otimes|0,0\rangle\;\;, \quad \text{(A.65)}$$

$$\langle p\alpha M_J;T,M_T|\,\boldsymbol{V}_c\,|\psi_d,M_d\rangle = \int d\hat{\boldsymbol{p}}\int d^3\boldsymbol{p}''$$
$$\times\sum_{m_l} Y_l^{*m_l}(\hat{p})C^{J,M_J}_{l,m_l;S,M_J-m_l}\sum_{l_d,m_{ld}} Y_{l_d}^{m_{ld}}(\hat{p''})C^{1,M_d}_{l_d,m_{ld};1,M_d-m_{ld}}\psi_{l_d}(p'')$$
$$\times\langle T,M_T|\otimes\langle S,M_J-m_l|\left[\frac{1}{2m}(\boldsymbol{p}_i+\boldsymbol{p}''_i)\frac{1}{2}(1+\tau_3)^{(i)}\delta^3(\boldsymbol{p}''-\boldsymbol{p}\pm\boldsymbol{q}/2)\right]|1,M_d-m_{ld}\rangle\otimes|0,0\rangle\;\;, \quad \text{(A.66)}$$

where $\boldsymbol{p}_i+\boldsymbol{p}_i''=\boldsymbol{q}+\boldsymbol{p}_i''+\boldsymbol{p}_i''=\boldsymbol{q}\pm 2\boldsymbol{p}''$, so when the delta function from the above expression is applied then $\boldsymbol{q}\pm 2\boldsymbol{p}''\to\pm 2\boldsymbol{p}$

$$\begin{aligned}\langle p\alpha M_J;T,M_T|\,\boldsymbol{V}_c\,|\psi_d,M_d\rangle &= \int d\hat{\boldsymbol{p}}\\ &\times\sum_{m_l} Y_l^{*m_l}(\hat{p})C^{J,M_J}_{l,m_l;S,M_J-m_l}\sum_{l_d,m_{ld}} Y_{l_d}^{m_{ld}}(\widehat{\boldsymbol{p}\mp\boldsymbol{q}/2})C^{1,M_d}_{l_d,m_{ld};1,M_d-m_{ld}}\psi_{l_d}(|\boldsymbol{p}\mp\boldsymbol{q}/2|)\\ &\times(\pm)\frac{\boldsymbol{p}}{m}\delta_{S,1}\delta_{M_J-m_l,M_d-m_{ld}}\frac{1}{2}(\delta_{T,0}\delta_{M_T,0}\pm\delta_{T,1}\delta_{M_T,0})^{(i)}\ ,\end{aligned}\tag{A.67}$$

$$\begin{aligned}\langle p\alpha M_J;T,M_T|\,\boldsymbol{V}_c\,|\psi_d,M_d\rangle &= \int d\hat{\boldsymbol{p}}\\ &\times\sum_{m_l} Y_l^{*m_l}(\hat{p})C^{J,M_J}_{l,m_l;S,M_J-m_l}\sum_{l_d,m_{ld}} Y_{l_d}^{m_{ld}}(\widehat{\boldsymbol{p}\mp\boldsymbol{q}/2})C^{1,M_d}_{l_d,m_{ld};1,M_d-m_{ld}}\psi_{l_d}(|\boldsymbol{p}\mp\boldsymbol{q}/2|)\\ &\times(\pm)\frac{1}{m}\sqrt{\frac{4\pi}{3}}p\left[Y_1^{-1}(\hat{p})\hat{\boldsymbol{e}}^{\boldsymbol{-1}}+Y_1^0(\hat{p})\hat{\boldsymbol{e}}^{\boldsymbol{0}}+Y_1^1(\hat{p})\hat{\boldsymbol{e}}^{\boldsymbol{+1}}\right]\\ &\times\delta_{S,1}\delta_{M_J-m_l,M_d-m_{ld}}\frac{1}{2}(\delta_{T,0}\delta_{M_T,0}\pm\delta_{T,1}\delta_{M_T,0})^{(i)}\ ,\end{aligned}\tag{A.68}$$

$$\begin{aligned}\langle p\alpha M_J;T,M_T|\,\boldsymbol{V}_c\,|\psi_d,M_d\rangle &= \int d\hat{\boldsymbol{p}}\sum_{m_l} Y_l^{*m_l}(\hat{p})C^{J,M_J}_{l,m_l;S,M_J-m_l}(\pm)\frac{1}{2}(\delta_{T,0}\delta_{M_T,0}\pm\delta_{T,1}\delta_{M_T,0})^{(i)}\\ \times\frac{1}{m}\sqrt{\frac{4\pi}{3}}p&\left[Y_1^{-1}(\hat{p})\hat{\boldsymbol{e}}^{\boldsymbol{-1}}+Y_1^0(\hat{p})\hat{\boldsymbol{e}}^{\boldsymbol{0}}+Y_1^1(\hat{p})\hat{\boldsymbol{e}}^{\boldsymbol{+1}}\right]\Bigg\{\delta_{S,1}\delta_{M_J-m_l,M_d}\frac{1}{\sqrt{4\pi}}\psi_0(|\boldsymbol{p}\mp\boldsymbol{q}/2|)\\ &+\sum_{m_{ld}}\delta_{S,1}\delta_{M_J-m_l,M_d-m_{ld}}Y_2^{m_{ld}}(\widehat{\boldsymbol{p}\mp\boldsymbol{q}/2})C^{1,M_d}_{2,m_{ld};1,M_d-m_{ld}}\psi_2(|\boldsymbol{p}\mp\boldsymbol{q}/2|)\Bigg\}\ .\end{aligned}\tag{A.69}$$

Magnetic Vector Current Matrix Element

The matrix element need it for the TPE is defined as $\langle p\alpha M_J;T,M_T|\left[\boldsymbol{q}\times\boldsymbol{V}_m\right]_3|\psi_d,M_d\rangle$ which is in other words for this case $\left[\boldsymbol{q}\times\langle p\alpha M_J;T,M_T|\,\boldsymbol{V}_m\,|\psi_d,M_d\rangle\right]_{3\equiv z}$, so solving for

$\langle p\alpha M_J; T, M_T| \boldsymbol{V}_m |\psi_d, M_d\rangle$ itself we get:

$$\langle p\alpha M_J; T, M_T| \boldsymbol{V}_m |\psi_d, M_d\rangle = \int d^3\boldsymbol{p}' \int d^3\boldsymbol{p}'' \langle p\alpha M_J; T, M_T|\boldsymbol{p}'\rangle \langle \boldsymbol{p}'| \boldsymbol{V}_m |\boldsymbol{p}''\rangle \langle \boldsymbol{p}''|\psi_d, M_d\rangle \ , \tag{A.70}$$

$$\begin{aligned}\langle p\alpha M_J; T, M_T| \boldsymbol{V}_m |\psi_d, M_d\rangle = &\int d\hat{\boldsymbol{p}} \int d^3\boldsymbol{p}'' \\ &\times \sum_{m_l} Y_l^{*m_l}(\hat{p}) C^{J,M_J}_{l,m_l;S,M_J-m_l} \sum_{l_d,m_{ld}} Y_{l_d}^{m_{ld}}(\hat{p''}) C^{1,M_d}_{l_d,m_{ld};1,M_d-m_{ld}} \psi_{l_d}(p'') \\ &\times \langle T, M_T| \otimes \langle S, M_J - m_l| \otimes \langle \boldsymbol{p}'| \boldsymbol{V}_m |\boldsymbol{p}''\rangle \otimes |1, M_d - m_{ld}\rangle \otimes |0,0\rangle \ , \end{aligned} \tag{A.71}$$

$$\begin{aligned}\langle p\alpha M_J; T, M_T| \boldsymbol{V}_m |\psi_d, M_d\rangle = &\int d\hat{\boldsymbol{p}} \int d^3\boldsymbol{p}'' \\ &\times \sum_{m_l} Y_l^{*m_l}(\hat{p}) C^{J,M_J}_{l,m_l;S,M_J-m_l} \sum_{l_d,m_{ld}} Y_{l_d}^{m_{ld}}(\hat{p''}) C^{1,M_d}_{l_d,m_{ld};1,M_d-m_{ld}} \psi_{l_d}(p'') \\ \times\langle T, M_T|\otimes\langle S, M_J - m_l| &\left[i\frac{1}{2m}(\boldsymbol{\sigma_i}\times\boldsymbol{q})(\kappa_0+\kappa_1\tau_3)^{(i)}\right]\delta^3(\boldsymbol{p}\text{"}-\boldsymbol{p}\pm\boldsymbol{q}/2)\,|1, M_d - m_{ld}\rangle\otimes|0,0\rangle \ , \end{aligned} \tag{A.72}$$

$$\begin{aligned}\langle p\alpha M_J; T, M_T| \boldsymbol{V}_m |\psi_d, M_d\rangle = &\int d\hat{\boldsymbol{p}} \\ \times \sum_{m_l} Y_l^{*m_l}(\hat{p}) C^{J,M_J}_{l,m_l;S,M_J-m_l} &\sum_{l_d,m_{ld}} Y_{l_d}^{m_{ld}}(\widehat{\boldsymbol{p}\mp\boldsymbol{q}/2}) C^{1,M_d}_{l_d,m_{ld};1,M_d-m_{ld}} \psi_{l_d}(|\boldsymbol{p}\mp\boldsymbol{q}/2|) \\ \times \langle S, M_J - m_l| &\left[i\frac{1}{2m}(\boldsymbol{\sigma_i}\times\boldsymbol{q})(\kappa_0\delta_{T,0}\delta_{M_T,0} \pm \kappa_1\delta_{T,1}\delta_{M_T,0})^{(i)}\right] |1, M_d - m_{ld}\rangle \ , \end{aligned} \tag{A.73}$$

$$
\begin{aligned}
\langle p\alpha M_J; T, M_T| \boldsymbol{V}_m |\psi_d, M_d\rangle &= \int d\hat{\boldsymbol{p}} \\
&\times \sum_{m_l} Y_l^{*m_l}(\hat{p}) C^{J,M_J}_{l,m_l;S,M_J-m_l} \sum_{l_d,m_{ld}} Y_{l_d}^{m_{ld}}(\widehat{\boldsymbol{p}\mp\boldsymbol{q}/2}) C^{1,M_d}_{l_d,m_{ld};1,M_d-m_{ld}} \psi_{l_d}(|\boldsymbol{p}\mp\boldsymbol{q}/2|) \\
\times \langle S, M_J - m_l| &\left\{ \frac{1}{2m} \left[(\sigma_0 q_{+1} - \sigma_{+1} q_0) e^{+1} + (\sigma_{-1} q_{+1} - \sigma_{+1} q_{-1}) e^0 + (\sigma_{-1} q_0 - \sigma_0 q_{-1}) e^{-1} \right] \right. \\
&\left. \times (\kappa_0 \delta_{T,0} \delta_{M_T,0} \pm \kappa_1 \delta_{T,1} \delta_{M_T,0})^{(i)} \right\} |1, M_d - m_{ld}\rangle \ , \quad \text{(A.74)}
\end{aligned}
$$

Now if we use the Wigner–Eckart theorem to operate on the spin σ matrices, we get the following:

$$
\langle S, M_s|\sigma_\mu^{(i)}|S_d, M_d\rangle = C^{S,M_s}_{S_d,M_d;1,\mu} \langle S||\sigma^{(i)}||S_d\rangle \ , \quad \text{(A.75)}
$$

where for our case the reduced matrices for both particles $\langle 1||\sigma^{(1)}||1\rangle = \langle 1||\sigma^{(2)}||1\rangle = \sqrt{2}$

$$
\begin{aligned}
\langle p\alpha M_J; T, M_T| \boldsymbol{V}_m |\psi_d, M_d\rangle &= \int d\hat{\boldsymbol{p}} \sum_{m_l} Y_l^{*m_l}(\hat{p}) C^{J,M_J}_{l,m_l;S,M_J-m_l} \\
\times \sum_{l_d,m_{ld}} & Y_{l_d}^{m_{ld}}(\widehat{\boldsymbol{p}\mp\boldsymbol{q}/2}) C^{1,M_d}_{l_d,m_{ld};1,M_d-m_{ld}} \psi_{l_d}(|\boldsymbol{p}\mp\boldsymbol{q}/2|) \left\{ \frac{1}{2m} \sqrt{\frac{4\pi}{3}} q \langle S||\sigma^{(i)}||1\rangle \right. \\
&\times \Big[(C^{S,M_j-m_l}_{1,M_d-m_{ld};1,0} Y_1^1(\hat{q}) - C^{S,M_j-m_l}_{1,M_d-m_{ld};1,1} Y_1^0(\hat{q})) e^{+1} + \\
&(C^{S,M_j-m_l}_{1,M_d-m_{ld};1,-1} Y_1^1(\hat{q}) - C^{S,M_j-m_l}_{1,M_d-m_{ld};1,1} Y_1^{-1}(\hat{q})) e^0 + \\
&(C^{S,M_j-m_l}_{1,M_d-m_{ld};1,-1} Y_1^0(\hat{q}) - C^{S,M_j-m_l}_{1,M_d-m_{ld};1,0} Y_1^{-1}(\hat{q})) e^{-1} \Big] \\
&\left. (\kappa_0 \delta_{T,0} \delta_{M_T,0} \pm \kappa_1 \delta_{T,1} \delta_{M_T,0})^{(i)} \right\} \ , \quad \text{(A.76)}
\end{aligned}
$$

$$
\begin{aligned}
\langle p\alpha M_J; T, M_T | \boldsymbol{V}_m | \psi_d, M_d \rangle = & \int d\hat{\boldsymbol{p}} \sum_{m_l} Y_l^{*m_l}(\hat{p}) C^{J,M_J}_{l,m_l;S,M_J-m_l} \\
& \times \frac{1}{2m}(\kappa_0 \delta_{T,0}\delta_{M_T,0} \pm \kappa_1 \delta_{T,1}\delta_{M_T,0})^{(i)} \sqrt{\frac{4\pi}{3}} q \langle S || \sigma^{(i)} || 1 \rangle \\
\Bigg\{ \Bigg[& (C^{S,M_j-m_l}_{1,M_d;1,0} Y_1^1(\hat{q}) - C^{S,M_j-m_l}_{1,M_d;1,1} Y_1^0(\hat{q})) e^{+1} + (C^{S,M_j-m_l}_{1,M_d;1,-1} Y_1^1(\hat{q}) - C^{S,M_j-m_l}_{1,M_d;1,1} Y_1^{-1}(\hat{q})) e^0 + \\
& (C^{S,M_j-m_l}_{1,M_d;1,-1} Y_1^0(\hat{q}) - C^{S,M_j-m_l}_{1,M_d;1,0} Y_1^{-1}(\hat{q})) e^{-1} \Bigg] \frac{1}{\sqrt{4\pi}} \psi_0(|\boldsymbol{p} \mp \boldsymbol{q}/2|) + \\
& \sum_{m_{ld}} Y_2^{m_{ld}}(\widehat{\boldsymbol{p} \mp \boldsymbol{q}/2}) C^{1,M_d}_{2,m_{ld};1,M_d-m_{ld}} \Bigg[(C^{S,M_j-m_l}_{1,M_d-m_{ld};1,0} Y_1^1(\hat{q}) - C^{S,M_j-m_l}_{1,M_d-m_{ld};1,1} Y_1^0(\hat{q})) e^{+1} + \\
& (C^{S,M_j-m_l}_{1,M_d-m_{ld};1,-1} Y_1^1(\hat{q}) - C^{S,M_j-m_l}_{1,M_d-m_{ld};1,1} Y_1^{-1}(\hat{q})) e^0 + \\
& (C^{S,M_j-m_l}_{1,M_d-m_{ld};1,-1} Y_1^0(\hat{q}) - C^{S,M_j-m_l}_{1,M_d-m_{ld};1,0} Y_1^{-1}(\hat{q})) e^{-1} \Bigg] \psi_2(|\boldsymbol{p} \mp \boldsymbol{q}/2|) \Bigg\} . \qquad \text{(A.77)}
\end{aligned}
$$

Appendix B

Numerical solutions of the Deuteron Bound and Scattering States

B.1 Schrodinger Equation Solution for the Deuteron System

In this section, we solve the Schrodinger equation in momentum space for the case of the deuteron bound state. We can define the bound state equation as:

$$H\,|\psi_d, M_d\rangle = E_d\,|\psi_d, M_d\rangle \ , \tag{B.1}$$

$$\left(\frac{\hat{p}^2}{2m} + \hat{V}\right)|\psi_d, M_d\rangle = E_d\,|\psi_d, M_d\rangle \ , \tag{B.2}$$

where $\hat{p}$ represents the relative momentum between the two nucleons of the deuteron system, $\hat{V}$ denotes our interaction or potential, and E_d stands for the binding energy of the deuteron. Now, employing a partial-wave-decomposed momentum state $|pl\rangle = |p(ls)J, M_d\rangle \otimes |T, M_T\rangle$, where l signifies the orbital momentum, s indicates the spin, J represents the total angular momentum with projection M_d, and T and M_T denote the isospin of the system and its projection, respectively, we can express our partial-wave-decomposed state for the deuteron case as $|pl\rangle = |p(l1)1, M_d\rangle \otimes |0, 0\rangle$. From here, we project it onto the left side of the

Schrödinger Equation and then insert a complete set of partial-wave-decomposed momentum states, such as

$$\sum_{l'} \int_0^\infty dp' p'^2 \left|p'l'\right\rangle \left\langle p'l'\right| = 1 \ . \tag{B.3}$$

We can define the Schrodinger equation for the deuteron system as follows

$$\left(\frac{p^2}{2m}\delta_{l,l'} + \sum_{l'} \int_0^\infty dp' p'^2 \left\langle pl\right| \hat{V} \left|p'l'\right\rangle \right) \left\langle p'l'|\psi_d, M_d\right\rangle = E_d \left\langle pl|\psi_d, M_d\right\rangle \ . \tag{B.4}$$

From theory, we know that the deuteron bound state is represented by its S-wave at $l = 0$ and its D-wave at $l = 2$, and omitting the total angular momentum projection M_d (deuteron wave functions do not depend on it), we can define our Schrodinger equation for the deuteron as

$$\frac{p^2}{2m} \left\langle pl|\psi_d\right\rangle + \sum_{l',l=0,2} \int_0^\infty dp' p'^2 \left\langle pl\right| \hat{V} \left|p'l'\right\rangle \left\langle p'l'|\psi_d\right\rangle = E_d \left\langle pl|\psi_d\right\rangle \ . \tag{B.5}$$

and taking $\langle pl|\psi_d\rangle = \psi_l(p)$, we can re-write our equation where we have

$$\frac{p^2}{2m}\psi_l(p) + \sum_{l'=0,2} \int_0^\infty dp' p'^2 \left\langle pl\right| \hat{V} \left|p'l'\right\rangle \psi_{l'}(p') = E_d\psi_l(p) \ . \tag{B.6}$$

To solve this equation, we have to discretize the integral, such as

$$\sum_{l'=0,2} \int_0^\infty dp' p'^2 \to \sum_{l'=0,2} \sum_{j=0}^{N-1} w_j p_j'^2 \ , \tag{B.7}$$

where we use a mesh in momentum space of size N up to a large $p = \Lambda_{cutoff} = 2000$ MeV. At this point, we can re-write our bound-state equation using discretize points as

$$\frac{p_i^2}{2m}\psi_l(p_i) + \sum_{l'=0,2} \sum_{j=0}^{N-1} w_j p_j'^2 V_{l,l'}(p_i, p_j')\psi_{l'}(p_j') = E_d\psi_l(p_i) \ . \tag{B.8}$$

The above equation is simple an eigenvalue problem of the form $K\boldsymbol{x} = E_d\boldsymbol{x}$. We can use eigenvalue routines found in GSL-GNU Scientific Library to solve for the deuteron wave functions and then renormalize its wave components as done regularly in quatum mechanics:

$$\int_0^{\Lambda_{cutoff}} p^2 \left[\psi_0^2(p) + \psi_2^2(p)\right] dp = 1 \tag{B.9}$$

B.2 Lippmann-Schwinger Equation Solution

To calculate the nuclear matrix element in either the μd-capture and the two-photon exchange processes with final state interactions, we need to obtain the half shell elements of the t-matrix, which can be obtained by solving the Lippmann-Schwinger Equation, that is defined as

$$t_{L,L'}(p,p_o;E) = V_{L,L'}(p,p_o) + \sum_{L"} \int_0^\infty dk\ k^2 \frac{V_{L,L"}(p,k) t_{L",L'}(k,p_o;E)}{E - \frac{k^2}{m} + i\epsilon}\ , \tag{B.10}$$

where $E = p_o^2/m$ is the incident energy of the nucleon. Since the nucleon-nucleon scattering occurs at a positive energy E, then there is a pole at $E = k^2/m$, therefore we introduce $i\epsilon$ in the denominator in order to handle the pole. We can solve the integral on the right hand side of Eq. (B.10) by using the identity in Eq. (A.2). For numerical integration, we introduce an upper limit by changing the $\infty \to \Lambda$. At this point, we can re-write and expand the integral on the right hand side of Eq. (B.10) as follows

$$\begin{aligned} t_{L,L'}(p,p_o;E) = V_{L,L'}(p,p_o) + \sum_{L"} \Bigg[\mathcal{P} \int_0^\Lambda dk\ k^2 \frac{V_{L,L"}(p,k) t_{L",L'}(k,p_o;E)}{E - \frac{k^2}{m}} \\ - i\pi \int_0^\Lambda dk\ k^2\ V_{L,L"}(p,k) t_{L",L'}(k,p_o;E) \delta(E - k^2/m) \Bigg]\ . \end{aligned} \tag{B.11}$$

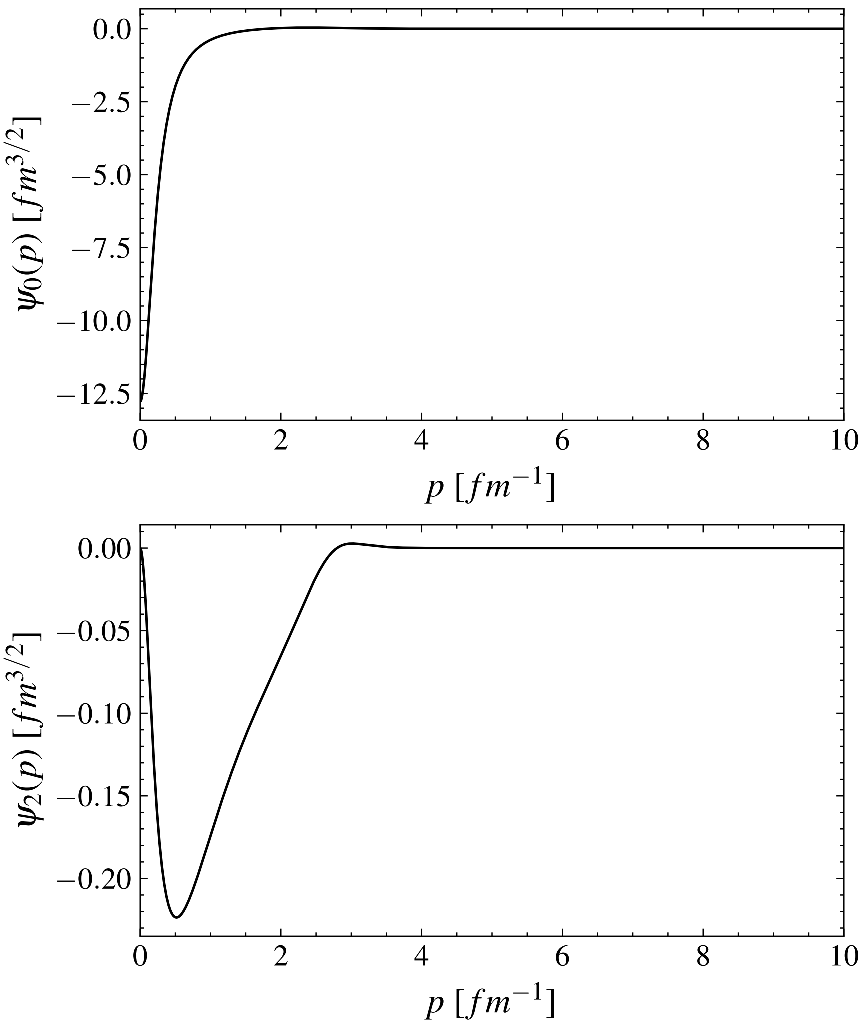

Figure B.1: Results for the deuteron wave functions S-wave (top figure) and D-wave (bottom figure) calculated using the N3LO Idaho interaction. Wave functions are in momentum space.

We can solve the expression inside the brackets as in Eq. (A.10) and write the resulting expression as

$$t_{L,L'}(p,p_o) = V_{L,L'}(p,p_o) + \sum_{L"} \Big\{ m \int_0^{\Lambda} dk\ k^2 \frac{V_{L,L"}(p,k) t_{L",L'}(k,p_o)}{p_o^2 - k^2} \\ - m \int_0^{\Lambda} dk\ p_o^2 \frac{V_{L,L"}(p_o,p_o) t_{L",L'}(p_o,p_o)}{p_o^2 - k^2} \\ - \frac{mp_o}{2}\ V_{L,L"}(p_o,p_o) t_{L",L'}(p_o,p_o) \big[log\Big(\frac{\Lambda + p_o}{\Lambda - p_o}\Big) - i\pi \big] \Big\} \ . \tag{B.12}$$

Now, we have to re-arrange the above equation in order to solve for the t-matrix; this can be done as

$$t_{L,L'}(p,p_o) - \sum_{L"} \Big\{ m \int_0^{\Lambda} dk\ k^2 \frac{V_{L,L"}(p,k) t_{L",L'}(k,p_o)}{p_o^2 - k^2} \\ - m \int_0^{\Lambda} dk\ p_o^2 \frac{V_{L,L"}(p_o,p_o) t_{L",L'}(p_o,p_o)}{p_o^2 - k^2} \\ - \frac{mp_o}{2}\ V_{L,L"}(p_o,p_o) t_{L",L'}(p_o,p_o) \big[log\Big(\frac{\Lambda + p_o}{\Lambda - p_o}\Big) - i\pi \big] \Big\} = V_{L,L'}(p,p_o) \ . \tag{B.13}$$

At this point, we need to discretize the variables and integrals for numerical solutions. Here the variable take the following form

$$\begin{aligned} p &\to p_i \ , \\ p_o &\to p_l \ , \\ k &\to k_j \ , \\ \int dk &\to \sum_{j=0}^{N} w_j \ , \\ t_{L,L'}(p,p_o) &\to t_{L,L'}(i,l) \ , \\ V_{L,L'}(p,p_o) &\to V_{L,L'}(i,l) \ , \end{aligned} \tag{B.14}$$

and re-writing the t-matrix equation as

$$t_{L,L'}(i,l) - \sum_{L"} \Bigg\{ m \sum_{j=0}^{N} w_j k_j^2 \frac{V_{L,L"}(i,j) t_{L",L'}(j,l)}{p_l^2 - k_j^2} - m \sum_{j=0}^{N} w_j p_l^2 \frac{V_{L,L"}(l,l) t_{L",L'}(l,l)}{p_l^2 - k_j^2}$$
$$- \frac{m p_l}{2} \; V_{L,L"}(l,l) t_{L",L'}(l,l) \Big[log \left(\frac{\Lambda + p_l}{\Lambda - p_l} \right) - i\pi \Big] \Bigg\} = V_{L,L'}(i,l) \; . \quad \text{(B.15)}$$

and re-arranging

$$\sum_{L"} \sum_{j=0}^{N} \Bigg\{ \delta_{i,j} \delta_{L,L"} - m w_j k_j^2 \frac{V_{L,L"}(i,j)}{p_l^2 - k_j^2} - m w_j p_l^2 \frac{V_{L,L"}(l,l)}{p_l^2 - k_j^2} \delta_{j,l}$$
$$- \frac{m p_l}{2} \; V_{L,L"}(l,l) \Big[log \left(\frac{\Lambda + p_l}{\Lambda - p_l} \right) - i\pi \Big] \delta_{j,l} \Bigg\} t_{L",L'}(j,l) = V_{L,L'}(i,l) \; . \quad \text{(B.16)}$$

We can solve this system of equations by using LU decomposition routines that can be found in GSL-GNU Scientific Library. Here there are two case to be solved. For uncoupled channels, in which $L = L' = L"$, the system of equations becomes simpler

$$\sum_{j=0}^{N} \Bigg\{ \delta_{i,j} - m w_j k_j^2 \frac{V(i,j)}{p_l^2 - k_j^2} - m w_j p_l^2 \frac{V(l,l)}{p_l^2 - k_j^2} \delta_{j,l}$$
$$- \frac{m p_l}{2} \; V(l,l) \Big[log \left(\frac{\Lambda + p_l}{\Lambda - p_l} \right) - i\pi \Big] \delta_{j,l} \Bigg\} t(j,l) = V(i,l) \; , \quad \text{(B.17)}$$

and for the case of coupled channels, the solution of the t-matrix is coupled to the different L, L', $L"$ projections, this is shown as follows

$$\begin{aligned} t_{dd} &= v_{dd} + v_{dd} G_0 t_{dd} + v_{du} G_0 t_{ud} \; , \\ t_{ud} &= v_{ud} + v_{ud} G_0 t_{dd} + v_{uu} G_0 t_{ud} \; , \end{aligned} \quad \text{(B.18)}$$

where u and d stand for L" indices that are lower or greater than L or L', respectively. As a result, the other coupled t-matrix configuration we have

$$
\begin{aligned}
t_{du} &= v_{du} + v_{dd}G_0 t_{du} + v_{du}G_0 t_{uu} \ , \\
t_{uu} &= v_{uu} + v_{ud}G_0 t_{du} + v_{uu}G_0 t_{uu} \ ,
\end{aligned} \tag{B.19}
$$

and their matrix representation are

$$
\begin{bmatrix} t_{dd} \\ t_{ud} \end{bmatrix} = \begin{bmatrix} v_{dd} & v_{du} \\ v_{ud} & v_{uu} \end{bmatrix} G_0 \begin{bmatrix} t_{dd} \\ t_{ud} \end{bmatrix} \ , \tag{B.20}
$$

and

$$
\begin{bmatrix} t_{du} \\ t_{uu} \end{bmatrix} = \begin{bmatrix} v_{dd} & v_{du} \\ v_{ud} & v_{uu} \end{bmatrix} G_0 \begin{bmatrix} t_{du} \\ t_{uu} \end{bmatrix} \ . \tag{B.21}
$$

For the uncoupled channel he solution is a $N \times N$ matrix, but for the coupled we encounter a $4(N \times N)$ matrix.

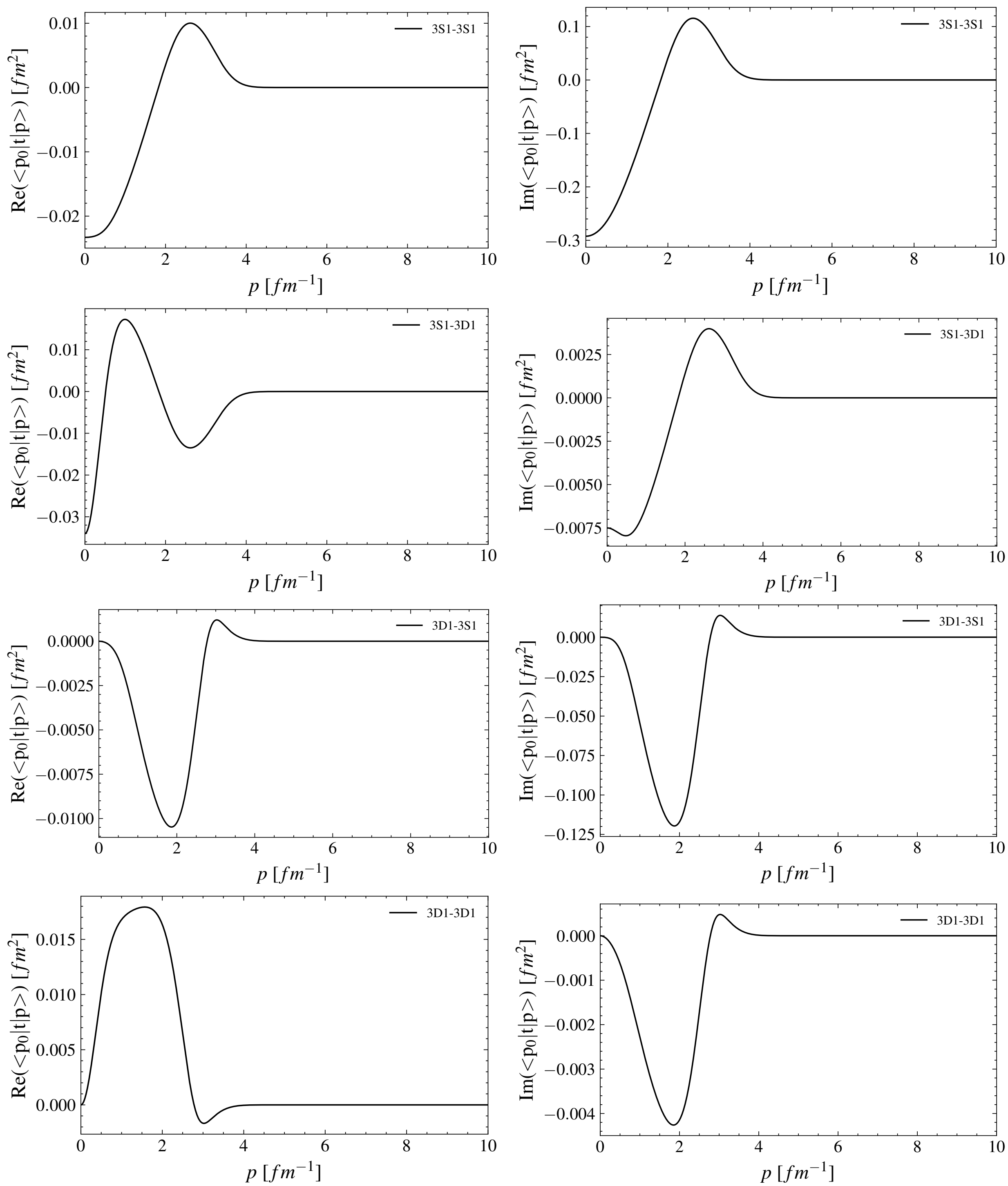

Figure B.2: Results for the half shell t-matrix using the N3LO Idaho interaction for the coupled channel ${}^3S_1$ - ${}^3D_1$. Matrix elements were evaluated to a fixed final momentum $p_0 = 0.5\ fm^{-1}$. Real and imaginary matrix elements of the t-matrix correspond to the left column and right column respectively.

Vita

Jose Bonilla grew up in Cali, Colombia, and immigrated to the United States in 2006. He served honorably in the U.S. Army starting in 2008 for about three years. In 2013, he attended the University of Tennessee in Knoxville, where he completed a Bachelor's degree in Mechanical Engineering, a double major in Physics, and a minor in Aerospace Engineering. During his undergraduate career, he discovered that in order to understand the building blocks of the universe, he needed to engage in knowledge more than usual, so he completed a PhD in Theoretical Nuclear Physics. After graduation, he will begin as a full-time researcher at the U.S. Naval Research Laboratory.